Designer 3D Magnetic Mesostructures

Müller, André

Award date:
2012

Awarding institution:
University of Bath

Designer 3D Magnetic Mesostructures

submitted by

André Müller

for the degree of Doctor of Philosophy

of the

University of Bath

Department of Physics

January 2012

Abstract

Micro Hall probe magnetometry has been used to investigate the magnetisation of various electrodeposited microcrystals. Superconducting tin crystals of almost perfect square cuboid shapes exhibit a strong size dependence of the supercooling of the superconducting state and, for the smallest accessible crystals, the crossover to the mesoscopic regime can be readily explored close to their critical temperatures. Experimental results are in good agreement with Ginzburg-Landau simulations using the exact experimental parameters. Electroplating of the tin cores with another material provides unique core-shell structures of either two superconductors (S-S': tin-lead) or of a superconducting core, covered with a ferromagnetic shell (S-F: tin/lead-nickel). The critical parameters of the tin core in Sn-Pb core-shell crystals are considerably enhanced and superconductivity in the tin core is detected up to $\approx 1.16 \cdot T_c^{\mathrm{Sn}}$. Little-Parks oscillations in the shell can be analysed to reveal the extent of the superconducting sheath and hence can be utilised to measure the range of the proximity effect close to the critical temperature of the shell. In S-F core-shell structures, field cancellation effects govern the overall behaviour. Under certain conditions it was possible to switch the overall magnetic response from para(ferro-)magnetic to diamagnetic and back at finite applied fields. Micromagnetic simulations qualitatively reproduce the experimentally observed effects. Applications for the core-shell structures include magnetic guidance or memory devices.

Acknowledgements

The work for this thesis was carried out between May 2008 and June 2011 in the Department of Physics at the University of Bath.

For the support during the work on this matter I would like to acknowledge the support of a couple of persons.

- First of all I would like to thank my supervisor Prof. S. J. Bending for giving me the opportunity to carry out this work and for his encouragement, support and enthusiasm throughout all its stages.
- The Ginzburg-Landau simulations presented in this work were all carried out by Prof. Milorad V. Milošević, who works now at the Departement Fysica at the Universiteit Antwerpen. He has provided invaluable insight into the workings of mesoscopic superconductors in innumerable discussions.
- The micromagnetic simulations shown in this work, were all carried out by Dr. Andreas Knittel and Prof. Hans Fangohr at the University of Southampton. Our meetings helped to understand the complex interaction between ferromagnetism and superconductivity in core-shell crystals.
- A great deal of help was provided by the technicians from the University of Bath, in particular I would like to thank Dr. Spartaco Landi, Wendy Lambson, Bob Draper and Paul Reddish for their help with the "hardware" aspects of the experiments and their effort, sometimes even beyond normal working hours.
- Many thanks go to the members of the Nanoscience Group, particularly

our former Postdocs Dr. Farzad Nasirpouri and Dr. Sara E. C. Dale who provided invaluably help in all experimental matters. Further I would like to thank all the other members of our group for many fruitful discussions, especially Dr. Miles A. Engbarth, Peter Curran, Mohammed El Bana, Waled Desoky and Dr. Andy Moskalenko.

- Also, I would like to thank all my new friends in Bath for their support and encouragement over the last three years and who made me have a great time in Bath.

- Finally I would like to thank my family for their helping support and encouragement over the years. My special thanks go to Lotte for being nice and even more to Steffi and my parents for taking care of her so often during my writing up work on this thesis.

Contents

List of figures

Chapter 1

Introduction

1.1 Motivation

Today electronic devices are indispensable in basically every aspect of life and whether it is a small battery powered Mp3-player or a huge industrial plant, the one thing all these devices have in common is the need for electricity. Large amounts of electrical energy are transferred over long distances through a lossy cable grid. Recently, due to the "green movement", energy production has moved away from the sites where it is consumed, and large amounts of energy are planned to be produced with off-shore wind farms, underwater turbines or in large arrays of photovoltaic cells in the desert of *e.g.* Spain. The production of energy is easy in all these places, but the main consumers are in different areas which are usually very far away. In addition, these methods do not produce energy in a continuous fashion, so at some times there is an overproduction and sometimes a deficiency of energy. This can be overcome by a large number or power sources which are naturally spread out over a large area. The problem of the transport of energy over large length scales and the storage of it is hence growing. Superconductors, which provide lossless transport of electrical energy would be a solution for the distribution of electric energy over arbitrary large distances. Unfortunately, as far as it is known today, superconductors exhibit this valuable characteristic only at low temperatures. Nevertheless, superconductors are already used in cooled

current networks, where the cost of cooling is offset by the cost of the lost energy and/or the cost of available space for cables. It is also used for short-term energy storage, where energy is simply stored in a superconducting current loop.

A side effect of the zero resistance in superconductors is the possibility to generate high magnetic fields with relatively little effort. For the transport of typical current densities, materials can be used which are cooled with liquid nitrogen. For high magnetic field applications, on the other hand, much lower temperatures are necessary. Applications include all sorts of laboratory equipment, medical magnetic resonance imaging or use as magnetic field generators in levitating trains.

A lot of effort is being put in the search for materials that exhibit superconductivity at higher temperatures, which could reduce the cost of cooling, and which are able to be moulded in the form of cables. Today, most high temperature superconducting materials are of ceramic nature and hence complicated for this use. In particular for high magnetic field applications, the long known, metal like, materials are favoured due to their plasticity. The necessary fabrication of long wires from ceramic-like high temperature materials is not possible with up-to-date fabrication techniques. The main principles of superconductivity are well understood, nonetheless many questions remain open. One field, where the understanding of superconductivity is incomplete, is the area of mesoscopic superconductors, when sample sizes are on the order of or less than micrometres. The behaviour of bulk superconductors is ruled mainly by the thermodynamics of the system, while in the mesoscopic regime the behaviour is governed by the surfaces and hence by the geometry and dimensions of the system. By controlling the size and shape of the sample, superconductivity can be either enhanced, or suppressed. A clear understanding of these effects is hence crucial, to design superconductors with targeted properties.

In this work, electrochemistry is utilised to grow such mesoscopic superconductors. Earlier work performed in the same group on lead gave new insights into vortex formation in small type I superconductors. This understanding is expanded here by using a similar approach with tin, which is even more type I than lead. In addition, the shapes that can be realised with tin are fundamentally different from typical lead crystals, due to a different crystallographic structure.

The suppression of the intermediate state in very small tin crystals yields an ideal system to study the metastable normal and superconducting phases, which form at the transition from superconducting to normal state and *vice versa* due to an externally applied magnetic field.

Ultimately two different materials can be combined in the form of core-shell crystals, where the tin core is a "weak" superconductor which is almost completely surrounded by the "stronger" superconductor lead. It is shown, that even a very thin lead shell is able to change the superconductivity in the tin core drastically.

Another method of controlling the superconductivity in the core of a core-shell crystal is by growing a ferromagnetic shell. The superposition of the external field and the stray field of the ferromagnetic shell results in a lower effective field at the position of the superconductor and enhancement of superconductivity.

Micromagnetic measurements on such crystals allow a very detailed study of the magnetisation in the sample as a function of the applied field. In particular, the advantage of being able to measure single crystals with known dimensions allows the ready simulation of the field dependent magnetisation behaviour of such systems. These simulations are performed by our collaborators. Ginzburg-Landau simulations are used to understand the magnetisation of purely superconducting systems, while micromagnetic simulations are utilised for simulating the magnetisation of the mixed ferromagnetic-superconducting systems.

1.2 Structure of thesis

The thesis is split in two major parts. The first three chapters give an introduction to the physical principles which were utilised in this work. In Chapter 2 an introduction to the principles of superconductivity is given. This chapter spans the history of 100 years since its discovery through the different models of superconductivity to the characteristic phenomena observed in mesoscopic samples and the special cases of the effects originating from two superconductors in close contact and the effect ferromagnetic materials have on superconductivity. The principles of electrochemistry and electrodeposition are introduced in Chapter 3

with focus on the electrodeposition of pure tin crystals and the deposition of core-shell crystals. The Hall probe technique used for the experiments is introduced in Chapter 4, where the fabrication of the Hall probes is explained and the general experimental set-up and the steps in the data analysis are explained.

The following three chapters discuss the experimental results. In Chapter 5 the results of pure tin crystals are described. Chapter 6 deals with the results from the superconductor-superconductor (tin-lead) core-shell crystals while in Chapter 7 core-shell crystals with a superconducting core and a ferromagnetic shell (lead/tin-nickel) are covered. The final Chapter 8 concludes the results of this work and gives some thoughts about future work on model superconducting and hybrid systems.

Chapter 2

Superconductivity

2.1 History of superconductivity

The year 2011 marks the first centenary of the discovery of superconductivity in 1911. In the following paragraph a brief summary is given of the development of this branch of solid state physics.

The precondition to the discovery of superconductivity was met in 1908 when Heike Kammerling Onnes first succeeded in building a machine to liquefy helium.[1] After the liquefaction of air by Linde 1895 and hydrogen by James Dewar 1898, helium, just discovered in 1895 by Sir William Ramsay,[2] was the last gas to be liquefied.[3] Helium, unlike hydrogen, is an inert gas. It has a boiling point of only 4.22 K and hence is an ideal coolant for low temperature physics. At the beginning of the 20^{th} century, the behaviour of ideal metals close to zero temperature was one of the key problems of physics. In his laboratory in Leiden, Onnes planned a systematic series of measurements at liquid helium temperatures. Mercury (Hg) was one of the first metals he used for his measurements, because it was not only readily available in high purity, but also because of the ease of making electrical contacts with the measurements apparatus. On the 8^{th} April 1911, Gilles Holst, a laboratory assistant and PhD student of Onnes saw an almost discontinuous change in the resistivity ρ of pure mercury just below the boiling point of liquid

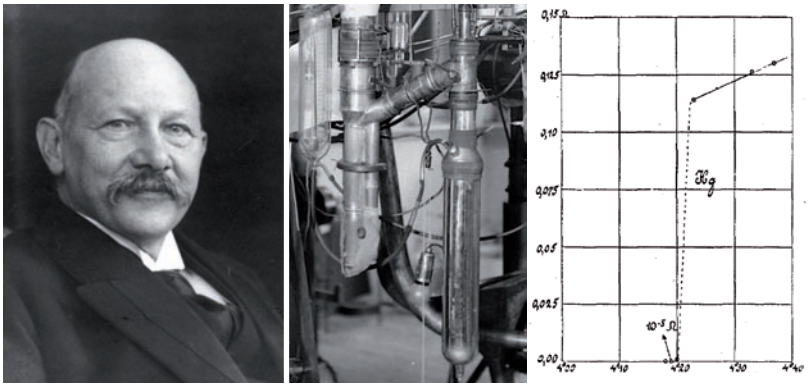

Figure 2-1: Heike Kammerling Onnes (left)[4] and his set-up for the experiment on 08.04. 1911 (middle).[5] On the right the historic plot of the jump in resistivity of mercury.[6]

helium.[7] He found, that the resistivity of helium drops to less that 1/350 of the value just above the jump.[8] Two years later he found that tin and lead show the same behaviour, although he was not able to measure the temperature below which lead became superconducting, as his measurements were all carried out below the boiling point of helium and thus below the critical temperature of lead. In that year, the expression "superconductor" was used to describe the newly discovered phenomenon for the first time. But Onnes also found that the resistivity increased to a larger value above a certain current. Once lead and tin were found to be superconducting,[9] it was possible to make long wires out of these metals, wound up as coils, to measure the conductivity more accurately. It was found, that these coils have a lower critical current compared to unwound wires. It was understood that a high current as well as a high magnetic field led to the breakdown of superconductivity,[10] although there was no explanation for this behaviour by this time. Onnes, who proposed to use superconducting wires to make coils for high magnetic field applications, was very disappointed by that finding.[11]

For the following years, the property of zero resistance, being a perfect conductor, was the main characteristic of a superconductor and the many attempts to explain it were focused on that behaviour. Though some experiments indicated other effects in a superconductor below its critical temperature, T_c, the most important finding was by Walther Meissner and Robert Ochsenfeld in Berlin in

1933.[12] They demonstrated that the magnetic field is expelled from the interior of the superconductor. At the same time Cornelis Jacobus Gorter and Hendrik Casimir were working on a thermodynamic model of superconductivity which was able to describe the effect Meissner found.[13] As the theory was now justified by an experiment, they published their "two fluid model" of superconductivity considering the superconducting state as a phase. However, no theory yet took into account the electrodynamics of the system.

The brothers Fritz and Heinz London were working on the problem in Oxford and published their famous article "The Electromagnetic Equations of the Supraconductor"[14] in 1935. The London equations were phenomenologically justified modifications to the Maxwell equations to correctly describe the Meissner effect. The London penetration depth λ_L describes the extent to which a magnetic field is able to penetrate the sample. However, not all samples showed the full Meissner effect at once but gradually entered the superconducting state. This led Sir Rudolf Ernst Peierls in Oxford to propose an intermediate state with normal and superconducting domains, depending on the demagnetising factor of the sample, coexisting in the sample.[15] The intermediate state was shortly after theoretically explained by Lev Davidovich Landau in Kharkhov.[16] Until after the war only few discoveries were made in the field of superconductivity. Still, progress in explaining the superfluidity of liquid helium (Helium II) with a Bose-Einstein condensate by Fritz London and Laslo Tisza helped eventually understanding what happened to the electrons in a superconductor.[11] After World War II a wide range of technical equipment became available, especially the new radar technology proved to be useful. In the late 1940s Sir Alfred Brian Pippard in Cambridge used radar frequency measurements to determine the penetration depth for superconductors. He found that by adding small impurities to his samples the penetration depth changed significantly. He came to the conclusion, that superconductivity is controlled by some long range interaction, which he called "coherence range" ξ.[17] At about the same time, two American groups, independently, found that different isotopes of the same material have slightly different critical temperatures and fields, the isotope effect.[18–20] The isotope effect suggested that the crystal lattice, especially the phonons might play an important role in the mechanism of superconductivity.

In the meantime in the Soviet Union Vitaly Lazarevich Ginzburg and Lev Davidovich Landau published their famous paper "Phenomenological theory of superconductivity",[21] which extended the London theory of superconductivity in that they proposed an effective wave function and the possibility that the superfluid varies in space. Unfortunately their theory was almost unrecognised in the western world for many years, as in 1950 all Soviet publications reaching the port of New York City were dumped overboard in the name of defending the free world.[11] The Ginzburg-Landau parameter κ defined in this paper divides superconductors in two types (Type I with $\kappa < 1/\sqrt{2}$ and Type II with $\kappa > 1/\sqrt{2}$). While Ginzburg and Landau ignored the case that their parameter can become larger than unity, Alexei Alexeevich Abrikosov simulated a material with a large κ and found that a superconductor under these circumstances would not expel all magnetic flux but be rather interspersed with flux lines containing exactly one flux quantum Φ_0.[22] Although he found this just two years after the initial Ginzburg Landau paper, he was only allowed to publish it in 1957, after Landau gave his permission to do so.

On the other side of the iron curtain again, John Bardeen, Leon Neil Cooper and John Robert Schrieffer worked on another approach to explain the basics of superconductivity in Illinois. Their approach involved the coupling of the electrons and the phonons in the crystal lattice, as indicated by the isotope effect. Cooper proposed an attractive interaction between two electrons which would then form a Cooper-Pair.[23] One Year later, Bardeen, Cooper and Schrieffer published their paper "Theory of Superconductivity" in which they formulated the BCS theory of superconductivity.[24] While the approach of the London Brothers and the one from Ginzburg and Landau are phenomenological theories, the BCS theory was the first rigorous microscopic approach to explain superconductivity.

In the following years the theory of superconductivity was applied to numerous problems of superconductivity and led to a large number of publications in that area. In 1960, Ivar Giaever studied Superconductor/Insulator/Superconductor (S/I/S) tunnel junctions and found that the I/V characteristic can be used to determine not only the energy gap of the superconductor, but can also verify the strength of the electron-phonon coupling.[25] A thorough analysis of these effects due to Brian David Josephson revealed the effect named after himself, the

Josephson effect.[26] He predicted that a direct current of Cooper pairs can flow between two superconductors, even if no voltage is applied (DC Josephson effect). If, however, a voltage is applied, there will be an alternating current between the electrodes (AC Josephson effect). The frequency of the alternating current is proportional to the applied voltage. Just two years later, Robert Jaklevic, John Lambe, James Mercereau, and Arnold Silver invented a DC Superconducting Quantum Interferference Device (SQUID) which uses the Josephson effect in two parallel legs to enable magnetisation measurements with extremely high accuracy.[27]

While in the following years innumerable mainstream applications for superconductors were proposed, most of them turned out to be not very useful due to the low temperatures required to keep the material superconducting. The game changed, however, in 1986 when Johannes G. Bednorz and Karl A. Müller at the IBM research laboratory in Zürich found the first high-T_c superconductor with a critical temperature of $T_c \approx 30$ K. Until today, the T_c has risen to $T_c \approx 135$ K under ambient pressure and up to $T_c \approx 164$ K at high pressures.[28] It is claimed, that the ultimate goal of room temperature superconductivity will never be achieved, but the recent discovery of a new branch of high-T_c superconductors, the Iron pnictides, in 2008[29] or the discovery of MgB_2 to be a conventional superconductor with $T_c = 39$ K in 2001[30] show that even 100 years after the first observation of superconductivity there is still much to discover.

2.2 Introduction to superconductivity

The following section concentrates on the general theory of superconductivity, explaining phenomena emerging in bulk superconductors and in semi infinite superconductors. The special case of 3D samples with small dimensions is discussed in the next section 2.3. Two different approaches to explain the phenomena of superconductivity are distinguished in this chapter. The phenomenological approach uses experimental findings which lead to a theory, such as the London equations (Sec. 2.2.2) and the Ginzburg-Landau formalism (Sec. 2.2.4), while the microscopic approach tries to explain superconductivity by extending known mi-

croscopic theories of the solid state, it is hence a "bottom up" approach. The BCS theory (Sec. 2.2.3), named after its inventors Bardeen, Cooper and Schriefer, is based on common solid state theories, which are amended to account for superconductivity.

2.2.1 Meissner effect

Alongside zero resistivity, from which the name superconductor originates, the perfect diamagnetism (Meissner effect) inside a superconductor, independent of its magnetic and thermal history, is a main characteristic of a superconductor. It shows that a superconductor is not only a perfect conductor. The Meissner effect is a result of surface supercurrents, which are formed spontaneously at the surface of a superconducting sample exposed to an external magnetic field. These currents exactly cancel the external magnetic field in the interior of the superconductor. The susceptibility in the inside of a superconductor is $\chi \equiv -1$. The effect is illustrated in the sketch in Fig. 2-2. The difference in behaviour for a superconductor and a perfect conductor can be explained for the case that the sample is placed in an external magnetic field B_a and cooled below the critical temperature T_c. In an ideal conductor with $R = 0$, a field B_a which is applied at $T < T_c$ is expelled due to supercurrents in the sample and if the field is switched off, the sample returns to a non-magnetised state. If, however, the field is applied at $T > T_c$ before the sample is cooled below T_c, the field penetrates the sample and supercurrents are induced when the field is switched off, maintaining the magnetic field and keeping the sample magnetised (Fig. 2-2 left). A superconductor on the other hand will expel the applied field B_a irrespective of the temperature at which the field is applied at and for $B_a = 0$ the sample is always non-magnetised (Fig. 2-2 right). This difference between a perfect conductor, with only $R = 0$ for $T < T_c$, and a superconductor emphasises the different nature of the superconducting state.

The free energy change ΔF corresponding to a magnetisation of a material is

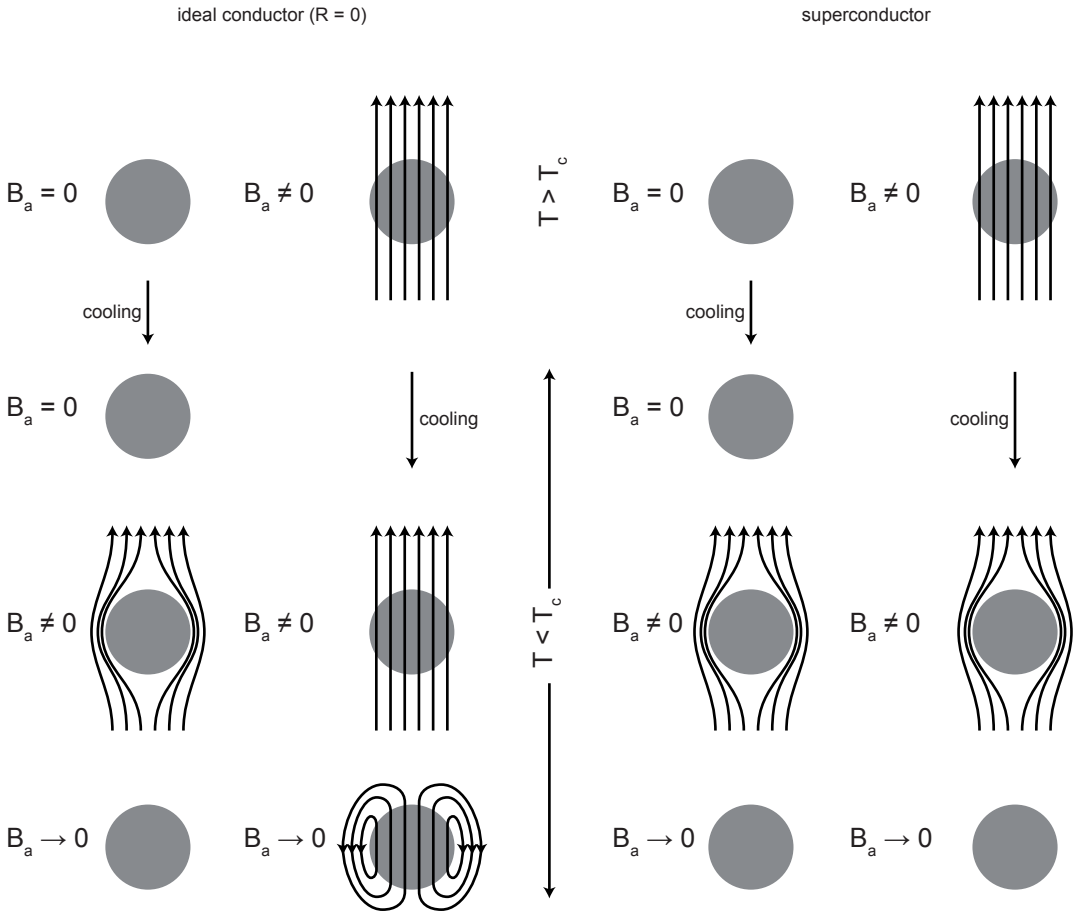

Figure 2-2: The magnetic behaviour of an ideal conductor and a superconductor. The final state of an ideal conductor (left) depends on whether the magnetic field B_a is applied below T_c (left column) or above T_c (right column). In the former case, the field is expelled below T_c and after switching the field off, the sample remains non-magnetised. In the latter case, the field is frozen in below T_c and the supercurrents perpetuate the field so that the sample remains magnetised when the field is switched off. For a superconductor (right) the applied field is expelled below T_c in both cases and the sample is always non-magnetised when the field is switched off.[31]

specified by

$$\Delta F(H_a) = -\mu_0 \int_0^{H_a} M \mathrm{d}H. \tag{2.1}$$

For a superconductor, which is a perfect diamagnet, $\chi = -1$ and hence $M = -H$

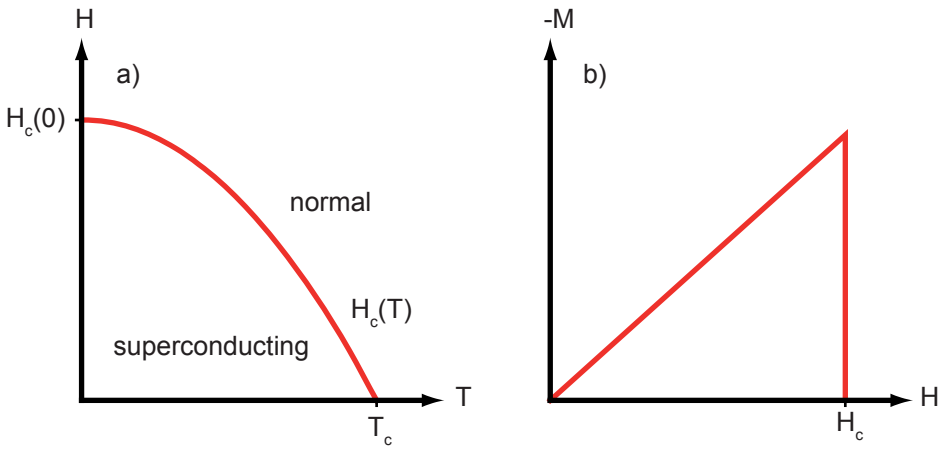

Figure 2-3: The magnetic phase diagram of a superconductor. The temperature dependence of the critical field $H_c(T)$ is shown in (a) and a magnetisation curve $M(H)$ is shown in (b).

this yields the free energy difference for a superconductor:

$$\Delta F(H_a) = \frac{\mu_0 H_a^2}{2}. \tag{2.2}$$

If this energy change is larger than the difference in free energy between the normal and superconducting state, superconductivity breaks down. The corresponding field H_a is called the critical field H_c of the superconductor. $H_c(T)$ is characteristic for a material and a function of temperature T. It was found empirically, that the critical field follows quite well a parabolic law

$$H_c\,(T) \approx H_c\,(0) \cdot \left(1 - \left(\frac{T}{T_c}\right)^2\right). \tag{2.3}$$

The magnetic phase diagram for a superconductor is shown in Fig. 2-3a as well as a magnetisation curve (Fig. 2-3b) illustrating the discontinuous change in magnetisation at $H = H_c$.

2.2.2 London equations

The equations suggested by the London brothers are able to describe the behaviour of a superconductor.[14] The theory is based on phenomenological principles, hence it only describes the phenomena and is not a logical consequence of fundamental principles. The classical equation for moving electrons in a conductor is

$$m\dot{\vec{v}} = -e\vec{E} + \frac{m\vec{v}}{\tau} \tag{2.4}$$

containing the electron charge (e) and mass (m), electron velocity v and electric field $\vec{E}$. τ is the damping time, the typical time in which the velocity of an electron decreases to the thermal motion due to scattering of the electron in the material. This last part, the damping term, is abandoned for a superconductor, as the electron velocity is not damped in a superconductor. Hence:

$$m\dot{\vec{v}} = -e\vec{E} \tag{2.5}$$

and for the superconducting current density $\vec{j_s} = en_s\vec{v}$, where n_s denotes the density of superconducting electrons, one gets

$$\dot{\vec{j_s}} = \frac{n_s e^2}{m}\vec{E}.^1 \tag{2.6}$$

This equation (2.6) is usually referred to as the first London equation. This and the Maxwell equation $\nabla \times \vec{E} = -\dot{\vec{B}}$ leads to the relation

$$\frac{\partial}{\partial t}\left(\frac{m}{n_s e^2}\nabla \times \vec{j_s} + \vec{B}\right) = 0. \tag{2.7}$$

This equation alone shows only the behaviour of an ideal conductor, but not the Meissner effect. To account for the complete vanishing of the field inside the superconductor, the integration constant of the integral of Eq. (2.7) has to be exactly zero. This leads to the second London equation:

$$\nabla \times \vec{j_s} = -\frac{n_s e^2}{m}\vec{B}. \tag{2.8}$$

[1] Note the change in sign due to the definition of the current, as the flow of positive charges.

The common factor in these equations can be merged to

$$\Lambda_L = \frac{m}{n_s e^2}. \tag{2.9}$$

The following equations replace Ohm's law for a superconductor:

$$\vec{E} = \Lambda_L \dot{\vec{j}_s} \tag{2.10}$$

$$\vec{B} = -\Lambda_L \nabla \times \vec{j_s} \tag{2.11}$$

$$\nabla \times \vec{B} = \mu_0 \vec{j_s}. \tag{2.12}$$

These are the two London equations and the Maxwell equation (2.12). The combination of Eq. (2.11) and Eq. (2.12) yields another important property of a superconductor as

$$\nabla \times \nabla \times \vec{B} = \mu_0 \nabla \times \vec{j_s} = -\frac{\mu_0}{\Lambda_L}\vec{B} \tag{2.13}$$

and as $\nabla \cdot \vec{B} = 0$ this equation transforms to

$$\Delta \vec{B} - \frac{\mu_0}{\Lambda_L}\vec{B} = 0. \tag{2.14}$$

Regarding the half infinite interface between a superconductor ($z > 0$) and the surrounding vacuum ($z < 0$) in a homogeneous magnetic field parallel to the interface ($\vec{B} = B_x \cdot \vec{\hat{x}}$), the solution of the equation above (Eq. (2.14)) is an exponential decaying function of the distance z from the interface into the superconductor

$$B_x = B_x^0 e^{-\sqrt{\mu_0/\Lambda_L}z}. \tag{2.15}$$

The distance to which a magnetic field penetrates the superconductor is called the London penetration depth

$$\lambda_L = \sqrt{\frac{m}{\mu_0 n_s e^2}}. \tag{2.16}$$

In the sketch in Fig. 2-4 the exponential decaying magnetic field in the inside of a superconducting material is shown.

The London equations are able to explain both main properties of a superconduc-

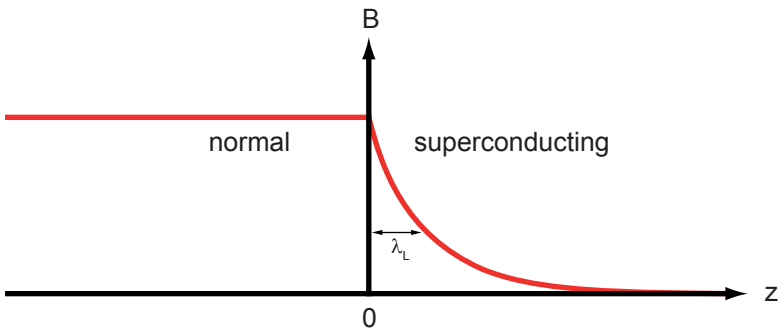

Figure 2-4: The magnetic flux density B is constant in vacuum ($z < 0$) and decays exponentially inside a superconductor ($z > 0$) with penetration depth λ_L.

tor (zero resistance and the Meissner effect) but the theory does not explain the formation of the superconducting phase. However, the London equations take into account the difference between a normal current and a supercurrent in the material as was proposed by Gorter and Casimir in their two fluid model.[13]

2.2.3 Cooper's model of superconductivity

In distinction to the phenomenological theories described in the former and the following section, Cooper's model, the introduction of the two electron bound state in form of a Cooper pair, and the BCS many body theory explain superconductivity from a microscopic point of view.[24] This perspective is especially useful for the understanding of some of the most important parameters of a superconductor.

Electrons are fermions which are controlled by Fermi statistics.[32] In a conductor, electrons occupy all energetic states up to the Fermi energy E_F. This is sometimes referred to as the Fermi-sea. Cooper showed that a weak attractive interaction between electrons in this ground state leads to bound states of at least two electrons.[23] This attractive interaction between two electrons is mediated by virtual phonons, as was already indicated by the isotope effect.[18,19] As the electron moves through the material, it attracts the nuclei of the atoms in the lattice, forcing them to bend towards the path of the electron. A simple sketch of this mechanism is shown in Fig. 2-5. In a similar consideration to that of the

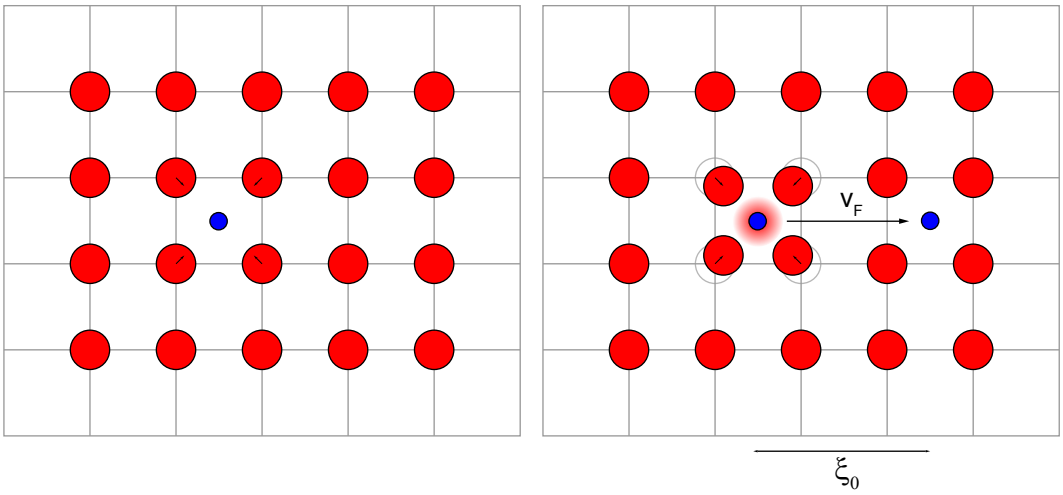

Figure 2-5: Sketch of the formation of a Cooper pair. In the left panel, an electron (blue) is shown amidst the lattice atoms (red). The negatively charged electron attracts the positively charged nuclei. The inert nuclei reach their maximum displacement only after the electron moved on (right panel). The slightly closer nuclei, compared to the neutral crystal, cause a positive excess charge at the former position of the electron which follows the electron. This positive charge region attracts a negatively charged electron. The size of this pair is the coherence length ξ_0 of the Cooper pair. In a real superconductor, the bound state is not between two electrons, but due to the opposing momenta $\vec{k}$ of the electrons, the partner continuously change.

Born-Oppenheimer approximation the heavy nuclei are much more inertial compared to the moving electron. This results in a retarded response to the charge of the electron, so that the highest accumulation of positive charge is reached far behind the electron. This trace of accumulated positive charge is a simple model of the attractive interaction mentioned above. The so coupled electrons are called a Cooper pair (CP). The size of a CP can be estimated by the distance of the electron and the maximum positive charge due to the nuclei to be $s = v_F \cdot 2\pi/\omega_D$. With a typical Fermi velocity $v_F \approx 10^8$ cm/s and the Debye frequency $\omega_D/2\pi \approx 10^{13}$ s^{-1} the result yields a size of a CP on the order of 1000 Å. This size ξ_0 can be identified with the previously introduced Pippard coherence length for a pure sample at $T = 0$ and a mean free path $l \to \infty$.[17] Obviously the size of a Cooper pair and hence the range of the attractive interaction is orders of magnitude larger than the Coulomb interaction between the two electrons. The latter reaches just as far as a couple of Å inside of a crystal. In terms of quantum mechanics the interaction can be described as the exchange of virtual phonons

due to the interaction of the electron with the lattice.

To calculate the energy of the interaction, two electrons above the Fermi energy are taken into account. The two electrons have a opposite wave vectors $\vec{k_1} = -\vec{k_2} = \vec{k}$ and with their positions $\vec{r}_{1,2}$ one gets the wavefunction:

$$\psi_0\left(\vec{r}_1, \vec{r}_2\right) = \sum_{\vec{k}} g_{\vec{k}} e^{i\vec{k}\vec{r}_1} e^{-i\vec{k}\vec{r}_2} \tag{2.17}$$

with the normalisation coefficient $g_{\vec{k}}$. This equation can then be inserted into the Schrödinger equation

$$-\frac{\hbar^2}{2m}\left(\nabla_1^2 + \nabla_2^2\right)\psi + V_0\psi = \left(\epsilon + 2E_F\right)\psi \tag{2.18}$$

where V_0 denotes the coupling energy for $\epsilon < E_F$ and ∇_1 and ∇_2 the nabla operators for the corresponding electron. The solution of this equation in a shell of $\hbar\omega_D$ around the Fermi surface results in the binding energy

$$\epsilon \approx -2\hbar\omega_D e^{-2/N(0)V_0} \tag{2.19}$$

with $N(0)$ the density of states at the Fermi level.[31] Although this is just a rough approximation, it shows that there is a two-electron bound state with a total energy $E = 2E_F - |\epsilon|$ below the Fermi energy for electrons with momenta above the Fermi wavevector. This attractive force leads to an instability of the Fermi-sea and to the creation of a high density of CPs, which occupy a new ground state with a lower energy than E_F. This new state is identical to the superconducting phase.

The two electrons of a CP in an ordinary superconductor, such as *e.g.* tin and lead, have identical, but opposite momentum and opposite spins with the consequence, that a CP behaves like a boson. As bosons are controlled by the Bose-Einstein statistics, all CPs are allowed to have the same ground state.

2.2.4 Ginzburg-Landau formalism

The Ginzburg-Landau theory (GL) is another phenomenological theory of superconductivity.[21] It is basically a modification of the London equations, (Sec. 2.2.2), which are based on classical mechanics. Ginzburg and Landau expanded these equations to a formalism which is based on quantum mechanics. The theory is derived from universally valid thermodynamic assumptions and concentrates on the macroscopic effects in a superconductor.

In the GL-theory the superconducting charge carrier density n_s^* is expressed as the square modulus of a complex order parameter ψ which has the form of a pseudo-wavefunction

$$\psi\left(\vec{r}\right) = \left|\psi\left(\vec{r}\right)\right| e^{i\phi(\vec{r})} \tag{2.20}$$

and hence

$$\left|\psi\left(\vec{r}\right)\right|^2 = n_s^*. \tag{2.21}$$

Based on Landau's theory of second order phase transitions,[33] the complex order parameter ψ, which is introduced in Eq. (2.20), can be used to calculate the free energy of the system close to the phase transition. Assuming only slow spatial variations of the order parameter ψ, the free energy of the system f can be expanded in a series of powers of the real variable $|\psi|^2$ about the point $T = T_c$. For the temperature $T = T_c$ the value of n_s^* vanishes and $\psi_0 = \psi\left(T_c\right) = 0$. The expansion of the free energy

$$f\left(|\psi|^2\right) = f\left(|\psi_0|^2\right) + \frac{\mathrm{d}f\left(|\psi_0|^2\right)}{\mathrm{d}\,|\psi|^2}\left(|\psi|^2 - |\psi_0|^2\right) + \frac{1}{2}\frac{\mathrm{d}^2 f\left(|\psi_0|^2\right)}{\mathrm{d}\,|\psi|^4}\left(|\psi|^2 - |\psi_0|^2\right)^2 + \ldots \tag{2.22}$$

is usually cut off after the second order terms. The differential factors of the first two terms of the expansion are defined as coefficients $\alpha\left(T\right)$ and $\beta\left(T\right)$, which simplifies Eq. (2.22) to

$$f_s = f_n + \alpha\left(T\right)|\psi|^2 + \frac{\beta\left(T\right)}{2}|\psi|^4 \tag{2.23}$$

with the superconducting free energy density f_s and the normal free energy density f_n. With $\beta\left(T\right) > 0$, the sign of $\alpha\left(T\right)$ decides whether the system is in the

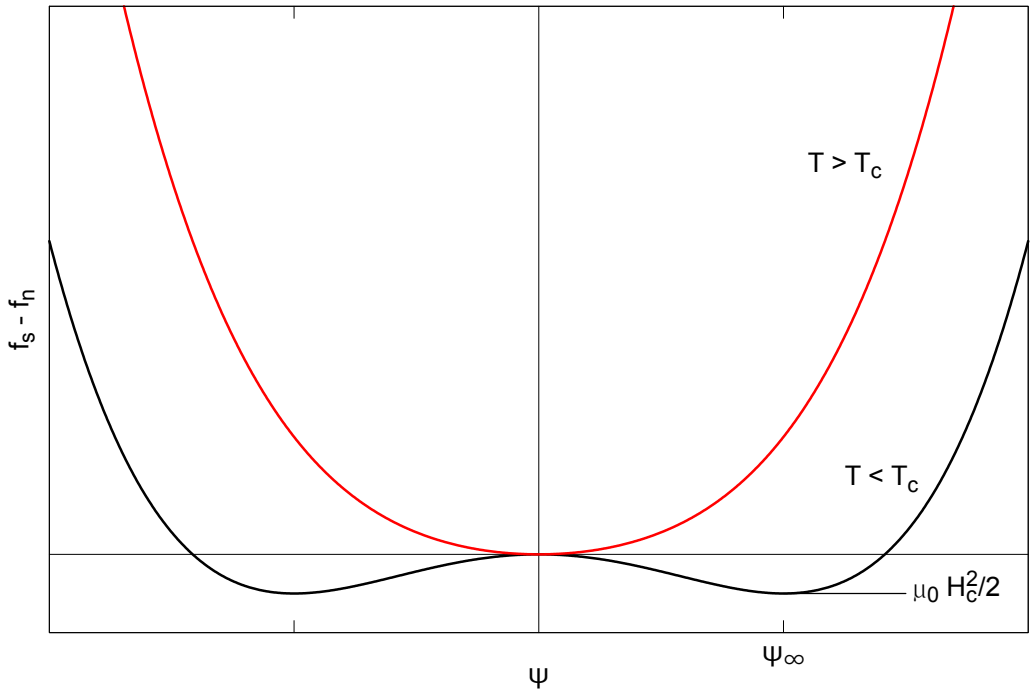

Figure 2-6: The GL free energy functions for $T < T_c$ ($\alpha < 0$) and $T > T_c$ ($\alpha > 0$).

normal or superconducting state. The minima in ψ are determined by differentiating equation (2.23). The solutions for

$$\alpha\psi + \beta |\psi|^2 \psi = 0 \tag{2.24}$$

are the trivial solution $|\psi|^2 = 0$ which is the only solution for $\alpha > 0$. This solution corresponds to the normal state for $T > T_c$ (red curve in Fig. 2-6). For $\alpha < 0$ and $T < T_c$ the solution is

$$|\psi|^2 = |\psi_\infty|^2 = n_s^* = -\frac{\alpha}{\beta}. \tag{2.25}$$

The earlier choice of $\beta(T) > 0$ becomes obvious by close inspection of this definition. From Eq. (2.23) and (2.25) the energy difference becomes $f_s - f_n = -\alpha^2/2\beta$ which is only positive for positive β. This is shown in the black curve in Fig. 2-6. ψ_∞ is the bulk value of ψ which is reached infinitely deep into the material, where the surface does not disturb the order parameter. The temperature dependence of $\alpha(T)$, which shows a sign change at $T = T_c$ is approximated by expanding it

in linear form. This yields a T-dependence

$$\alpha(T) = \alpha'(T - T_c) \tag{2.26}$$

with a constant α' for $T \to T_c$ and $T < T_c$. As α vanishes at T_c, so does ψ and

$$|\psi|^2 = -\frac{\alpha'(T - T_c)}{\beta}, \tag{2.27}$$

which is a typical behaviour for a second order phase transition.

The above discussed model is so far only valid for a homogeneous system, *i.e.* $\psi = \psi_\infty$ everywhere in the superconductor and no applied magnetic field. To account for the energy an external applied field would add and the additional energy originating from a gradient in the order parameter ψ, Eq. (2.23) has to be amended. The energy from the magnetic field was introduced in Eq. (2.2). To account for the additional energy of a gradient in ψ, this energy contribution is written in a form in analogy to the Schrödinger equation as

$$\frac{1}{2m^*} \left| \left(-i\hbar\nabla - e^* \vec{A} \right) \psi \right|^2 . \tag{2.28}$$

Here, m^* and e^* are the mass and charge of superconducting charge carriers. As was shown in Sec. 2.2.3, this is the mass and charge of a Cooper pair and hence $m^* = 2m_e$ and $e^* = 2e$. The combination of these terms with the free energy in Eq. (2.23) leads to the full expression for an inhomogeneous superconductor in a magnetic field

$$f_s = f_n + \alpha(T) \left|\psi(\vec{r})\right|^2 + \frac{\beta(T)}{2} \left|\psi(\vec{r})\right|^4 + \frac{1}{2m^*} \left| \left(-i\hbar\nabla - e^* \vec{A} \right) \psi(\vec{r}) \right|^2 + \frac{\mu_0 H^2}{2}. \tag{2.29}$$

The stable state is found by minimising the volume integral $\int f_s \mathrm{d}V$.[34] The result is the famous Ginzburg Landau equations:

$$\alpha\psi + \beta \left|\psi\right|^2 \psi + \frac{1}{2m^*} \left(-i\hbar\nabla - e^* \vec{A} \right)^2 \psi = 0 \tag{2.30}$$

$$\vec{J_s} = -\frac{ie^*\hbar}{2m^*} \left(\psi^* \nabla\psi - \psi \nabla\psi^* \right) - \frac{e^{*2}}{m^*} \psi^* \psi \vec{A} \tag{2.31}$$

where $\vec{J}_s$ is the supercurrent density.

Assuming the absence of a magnetic field ($\vec{A} = 0$) Eq. (2.30) leads to the definition of a characteristic lengthscale

$$\xi(T) = \sqrt{\frac{\hbar^2}{2m^*|\alpha|}}, \tag{2.32}$$

which is known as the GL coherence length. While the earlier defined coherence length ξ_0 (*cf.* Sec. 2.2.3) from the BCS theory is basically constant near the critical temperature, the GL coherence length $\xi(T)$ diverges for $T \to T_c$. The connection between these two lengths with basically identical names is not obvious, but for historical reasons, both are called coherence length. However, for very low temperatures and pure metals, these two parameters become comparable, $\xi(T) \approx \xi_0$.[35]

In Sec. 2.2.2 the London penetration depth λ_L (Eq. (2.16)) was introduced. With the definition of n_s^* as in Eq. (2.25) the London penetration depth becomes the temperature dependent penetration depth

$$\lambda(T) = \sqrt{\frac{m\beta}{2\mu_0|\alpha|e^2}}. \tag{2.33}$$

The parameters $\xi(T)$ and $\lambda(T)$ from Eq. (2.32) and (2.33) respectively, have a similar T dependence in the form shown here ($\propto |\alpha(T)|^{-1/2} \propto (T - T_c)^{-1/2}$) and are usually combined to generate the dimensionless Ginzburg-Landau parameter

$$\kappa = \frac{\lambda(T)}{\xi(T)}. \tag{2.34}$$

However, the series expansions used to derive the GL equation are valid only very close to T_c, while at T_c both parameters, $\xi(T)$ and $\lambda(T)$, diverge. The critical field H_c which results from the combination of equations (2.2) and (2.23) and the identity (2.25) together with the definitions of $\xi(T)$ and $\lambda(T)$ above, is given by

$$H_c(T) = \frac{\Phi_0}{2\sqrt{2}\pi\lambda(T)\xi(T)} \tag{2.35}$$

with the flux quantum Φ_0 which will be introduced in the next section. The theoretical T dependence deviates slightly from empirical data for $H_c(T)$ and $\lambda(T)$, so that in fact, $\kappa = \kappa(T)$.[35,36] The temperature dependence is usually expressed as

$$\kappa(T) = \frac{\kappa(0)}{1 + (T/T_c)^2}. \tag{2.36}$$

It was later shown, that the GL formalism can be derived from the BCS theory for a superconductor very close to T_c.[37] It is obvious from the way the formalism was derived, that the GL theory has its limitations. The approximations and the series expansions can only be used very close to T_c. But as the theory was developed from a phenomenological approach, the GL theory is ideal to simulate the behaviour of superconductors which is ruled by their size and geometry, as the GL formalism allows easy 3D modelling of a specific boundary value problem.

2.2.5 The critical fields of a superconductor

The fluxoid

Magnetic field lines that penetrate a superconducting sample, turn small areas from a superconducting to a normal state (*cf.* Fig. 2-7). The magnetic flux through these normal domains is quantised, as was shown experimentally almost simultaneously by Deaver & Fairbank and Doll & Näbauer and later by Little & Parks.[38–41] The smallest unit of flux in a superconductor is the magnetic flux quantum:

$$\Phi_0 = \frac{h}{2e} = 2.0679 \times 10^{-7}\text{G cm}^2. \tag{2.37}$$

The quantisation of the magnetic flux was already proposed by F. London,[42] but the nature of a Cooper pair was not understood when he proposed his fluxoid. Because he did not take into account the doubled charge of a Cooper pair, his original fluxoid was twice the value which was measured experimentally for a superconductor.

Utilising the GL formalism, flux quantisation can easily be shown by inserting the

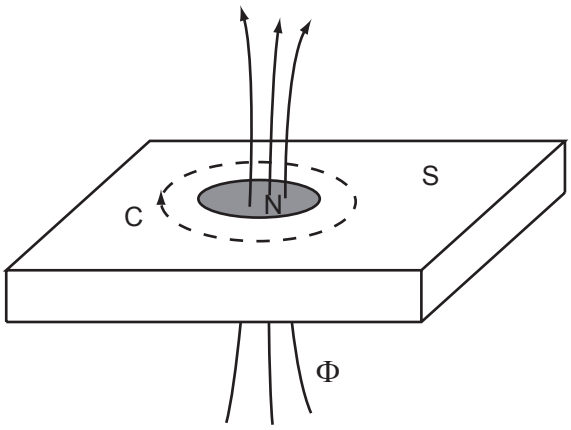

Figure 2-7: The magnetic flux Φ through a normal region (N) within a superconducting region (S). A contour C is chosen around the normal region.

wave function (2.20) into the second GL equation (Eq. (2.31)). The supercurrent can then be written as:

$$\vec{J}_s = -\frac{e\hbar}{2m}\left|\psi\right|^2 \nabla\phi - \frac{e^2}{m}\left|\psi\right|^2 \vec{A}. \tag{2.38}$$

The contour integral of the vector potential $\vec{A}$ around a closed path C gives, by using Stokes' theorem, the flux through the surface S enclosed by the path C.

$$\oint_C \vec{A}\cdot \mathrm{d}\vec{l} = \int_S \nabla\times\vec{A}\cdot \mathrm{d}\vec{S} = \int_S \vec{B}\cdot \mathrm{d}\vec{S} = \Phi \tag{2.39}$$

Rearranging Eq. (2.38) and inserting it in the equation above, one gets the quantisation of the magnetic flux:

$$\begin{aligned}\Phi = \oint_C \vec{A}\cdot \mathrm{d}\vec{l} &= -\frac{m}{e^2}\oint_C \frac{\vec{J}_s}{\left|\psi\right|^2}\cdot \mathrm{d}\vec{l} + \frac{\hbar}{2e}\underbrace{\oint_C \nabla\phi\cdot \mathrm{d}\vec{l}}_{=2\pi n} \\ &= n\frac{h}{2e} - \frac{m}{e^2}\underbrace{\int_C \frac{\vec{J}_s}{\left|\psi\right|^2}\cdot \mathrm{d}\vec{l}}_{=0}\,.\end{aligned} \tag{2.40}$$

The only condition for the order parameter function is, that the modulus of ψ has a single defined value. This means, that the phase ϕ is a multiple of 2π, with

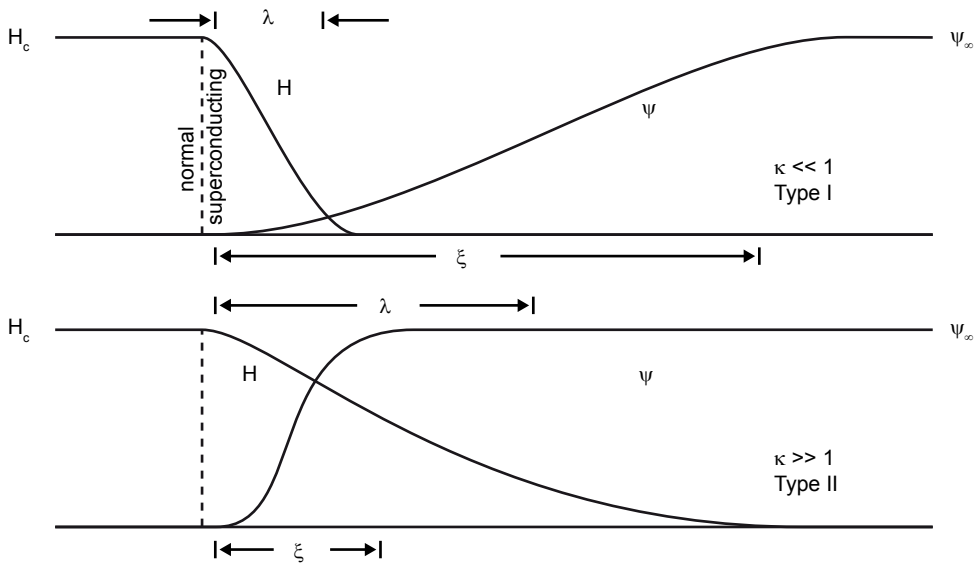

Figure 2-8: A sketch showing the importance of ξ and λ at a normal/superconducting interface. H decreases from H_c in the normal phase to zero inside of the superconducting phase within the penetration depth λ, while the order parameter ψ increases from zero at the interface to the bulk value ψ_∞ in the superconducting phase. The ratio $\kappa = \lambda/\xi$ defines whether a superconductor is of type I or type II.

$n \in \mathbb{N}$ any integer, when the integral is over a full turn around C. The path C can be chosen so that $\vec{J}_s = 0$ or $\vec{J}_s \perp \mathrm{d}\vec{l}$ for the contour C. The second term of the equation vanishes and with $h = 2\pi\hbar$ the relation becomes $\Phi = n\Phi_0$ with the magnetic flux quantum Φ_0 as defined in Eq. (2.37).[43]

Type I and type II superconductors

The two length scales, coherence length ξ and penetration depth λ, which are derived from the GL formalism describe the behaviour of the order parameter and the magnetic field at a normal/superconducting (N/S) interface. Each length scale is responsible for an opposing energy contribution to the system. The GL parameter κ, which is the ratio between these two parameters, provides a measure for the interfacial energy, whose sign divides a superconductor in type I and type II superconductors. Abrikosov was the first who studied theoretically the boundary between normal and superconducting regions.[22] A sketch of these considerations is shown in Fig. 2-8.

A rough estimate of the energy linked to the interface is possible by looking at the free energy difference originating from the magnetic field penetrating the superconducting region and from the absence of superconducting charge carriers in the proximity of the interface.[44] The free energy saved by letting the magnetic field penetrate the distance λ into the superconducting phase with the area A can be approximated as

$$E_1 = \lambda A \frac{1}{2} \mu_0 H_c^2. \tag{2.41}$$

A similar argument leads to the energy it costs to break the Cooper pairs up to a distance ξ deep in the superconducting phase.

$$E_2 = \xi A \frac{1}{2} \mu_0 H_c^2. \tag{2.42}$$

The difference of these two contributions

$$\Delta E = \xi A \frac{1}{2} \mu_0 H_c^2 - \lambda A \frac{1}{2} \mu_0 H_c^2 = \frac{1}{2} \mu_0 A H_c^2 (\xi - \lambda) \tag{2.43}$$

gives a measure of whether it is favourable to form such an interface and if free energy is gained ($\Delta E > 0$) or if it costs energy to form an interface ($\Delta E < 0$) and the formation of an interface is unfavourable.

In this estimation, the sign of ΔE changes when either ξ or λ gets larger than the other and hence $\kappa = 1$ divides type I and type II superconductors. This value is wrong by a factor of $1/\sqrt{2}$ as the actual value is $\kappa = 1/\sqrt{2}$. This was shown in a much more detailed calculation by Abrikosov.[22]

In the case of positive surface energy ($\xi > \lambda$), the superconductor is of type I. $\Delta E > 0$ means that it costs energy to generate the N/S interface and hence the building of such an interface is avoided. If, above a certain field, flux starts to penetrate the superconducting region, a domain structure of normal and superconducting areas forms. If, however, $\Delta E < 0$, energy is won by maximising the interface between normal and superconducting regions and the superconductor is of type II. As was shown above, a normal domain cannot have an arbitrarily small magnetic flux connected with it, as the smallest amount of flux is the magnetic flux quantum Φ_0. Fig. 2-9a shows a cross section of such an Abrikosov vortex. The order parameter ψ and hence the Cooper pair density $n_s = |\psi_\infty|^2$ is

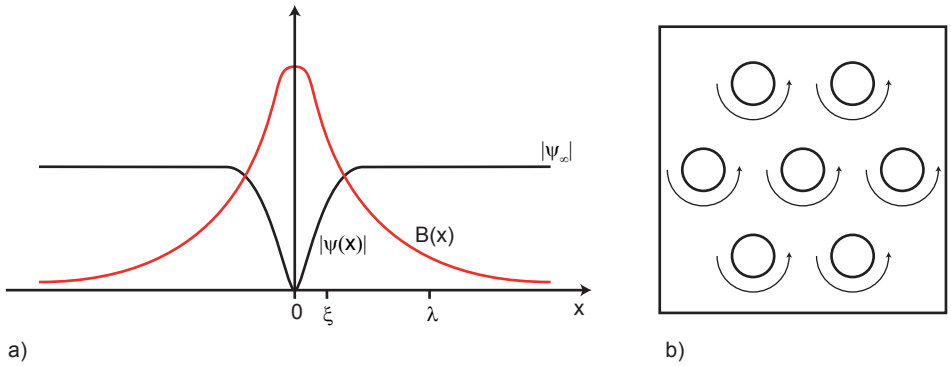

Figure 2-9: Cross-section of an isolated Abrikosov vortex showing the distribution of the Cooper pair density $|\psi(x)|$ and the magnetic field $B(x)$ (a). Vortices arrange in a triangular lattice. Supercurrents around the core keep the rest of the sample superconducting (b).

zero at the centre of the vortex in a region somewhat larger than the coherence length ξ in diameter.[35,45] At the same time, supercurrents form around each vortex (Fig. 2-9b) with a maximum current at a distance of λ from the core of the vortex line.

The current flows in opposite directions for two neighbouring vortices, which causes a repulsive force between two vortices. Abrikosov showed, that the vortices form a periodic lattice as this maximises the individual spacings. His calculations suggested a square lattice for the flux lines. It was later shown by Kleiner *et al.* that the lowest energy state is actually a triangular lattice as shown in Fig. 2-9b.[46]

2.2.6 Flux entry at H_{c1} and the nucleation field H_{c2}

It is apparent from the discussion in Sec. 2.2.5, that there are two different critical fields for a type II superconductor where something significantly changes in the superconducting state. The first field H_{c1} is defined as the field below which the sample is in the Meissner state, where the bulk of the sample is field free. For fields between H_{c1} and H_{c2} flux lines fill the sample as the magnetic field is increased until at a field of H_{c2} superconductivity is destroyed and the sample turns normal. This occurrence is shown in Fig. 2-10. With the GL formalism, the energy of a single flux line can be calculated. Above the field H_{c1} energy is

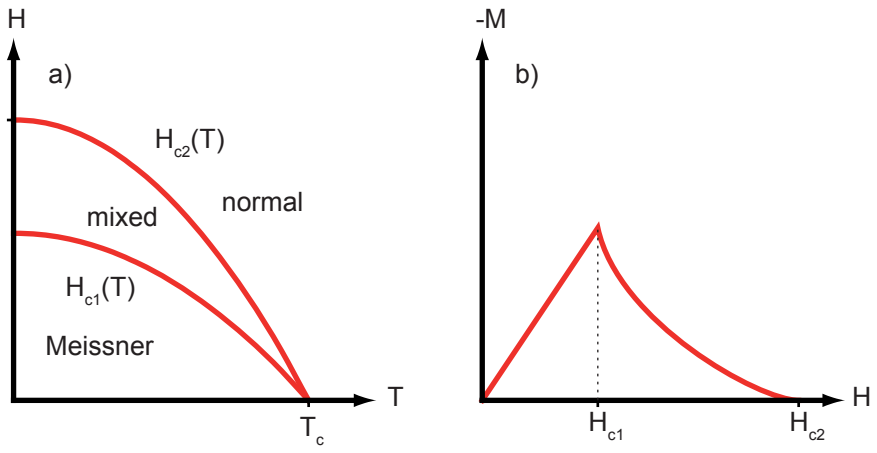

Figure 2-10: The magnetic phase diagram of a type II superconductor. As opposed to type I superconductors, two critical fields are defined (a). The first penetration critical field H_{c1} and the nucleation field H_{c2}. The magnetisation curve $M(H)$ which is shown in (b) shows that the sample is fully superconducting for $H < H_{c1}$, while for $H_{c1} < H < H_{c2}$ flux lines penetrate the sample. Only at H_{c2} does the whole sample turn normal.

gained by letting a flux line penetrate. The resulting field is

$$H_{c1} = \frac{\Phi_0}{4\pi\lambda^2} \ln \kappa = \frac{H_c}{\sqrt{2}\kappa} \ln \kappa. \tag{2.44}$$

With increasing field, more flux lines enter the sample. In the Meissner state $|\psi|^2 = |\psi_\infty|^2$ is the bulk value. This value decreases continuously to zero as the field is increased. The flux lines come closer together and finally start to overlap. For the case of an applied field very close to H_{c2}, where $|\psi|^2 \ll |\psi_\infty|^2$ equation (2.30) can be simplified by dropping the $\beta |\psi|^2 \psi$ term, which leads to the linearised GL equation

$$\frac{1}{2m^*} \left(-i\hbar\nabla - e^* \vec{A} \right)^2 \psi = -\alpha\psi. \tag{2.45}$$

This equation is similar to the Schrödinger equation for a particle in a harmonic oscillator potential, which can easily be solved. For this problem, the sample dimensions are assumed to be infinite in all directions and the magnetic field is parallel to the z-axis. The eigenvalues for this problem

$$E_{n,v_z} = \left(n + \frac{1}{2} \right) \hbar\omega_c + \frac{1}{2m^*} m^* v_z^2 = -\alpha \tag{2.46}$$

with the velocity v_z parallel to the field and the cyclotron energy $\hbar\omega_c = \frac{\hbar e^* H}{m^*}$ Eq. (2.46) can be rearranged and solved for

$$H = \left(-\alpha - \frac{v_z^2}{2}\right) \frac{m^*}{\left(n + \frac{1}{2}\right) \hbar e^*}. \tag{2.47}$$

For $T < T_c$, $\alpha < 0$ and hence the maximum field is reached for $n = 0$ and $v_z = 0$ which is for

$$H = -\alpha \frac{2m^*}{\hbar e^*}. \tag{2.48}$$

H can than be expressed in terms of the thermodynamic critical field H_c which was defined in Eq. (2.35). The result is the nucleation field

$$H_{c2} = \frac{\Phi_0}{2\pi\xi^2} = \frac{4\pi\lambda^2 H_c^2}{\Phi_0} = \sqrt{2}\kappa H_c \tag{2.49}$$

at which superconductivity starts to nucleate in a decreasing magnetic field.

This value of the nucleation field defines the actual value of κ for the crossover from type I to type II superconductors. If $H_{c2} < H_c$, the superconductor is of type I and if $H_{c2} > H_c$, the material is called type II. The two fields are identical $H_{c2} = H_c$ for $\kappa = 1/\sqrt{2}$.

2.2.7 Surface superconductivity at H_{c3}

The nucleation field H_{c2} was calculated for the bulk of the material inside an infinite sample in all dimensions. In a real sample, the surface plays an important role and needs to be considered when calculating the field for which nucleation takes place. Saint-James and de Gennes were the first to investigate the nucleation field of a semi-infinite sample.[47] The sample fills the half space $x > 0$ and the magnetic field is applied parallel to the surface. The boundary condition of a vanishing derivate of the order parameter at the surface $x = 0$ and $x \to \infty$

$$\left.\frac{\partial\psi}{\partial x}\right|_{\text{surface}} = 0 \tag{2.50}$$

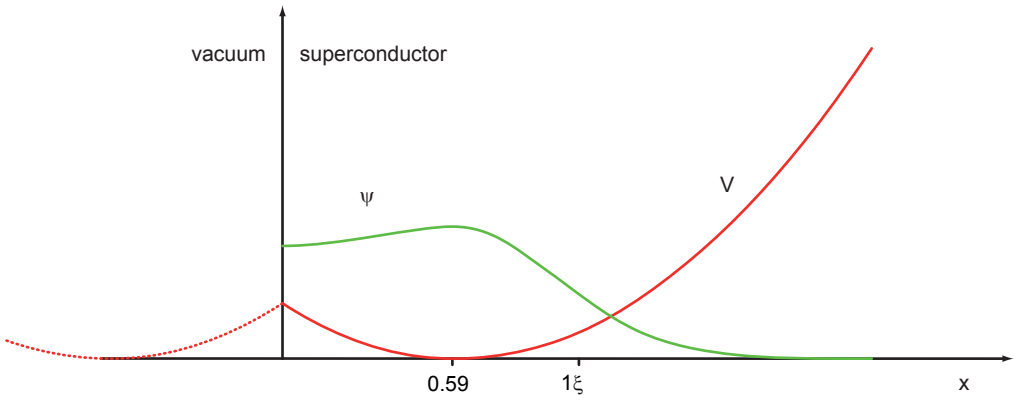

Figure 2-11: Nucleation of superconductivity in a field parallel to the surface. Sketched are the effective potential V with a minimum at $\approx 0.59\xi(T)$ inside the superconductor and the corresponding order parameter ψ.

is fulfilled by a similar ansatz as was used in Sec. 2.2.6 to calculate the nucleation field H_{c2} with the minimum of the potential at $x_0 = 0$ or ∞. In fact, the solution yields the same eigenvalues for the nucleation field as H_{c2}. A potential with lower eigenvalues than the one used above was constructed by Saint-James and de Gennes by shifting the potential by the order of ξ into the sample and mirroring the potential into the vacuum, forming a potential

$$V(x) = \begin{cases} V_0 \cdot (x - x_0)^2, & x > 0 \\ V(-x), & x < 0 \end{cases} \tag{2.51}$$

which also complies with the boundary condition of Eq. (2.50). The potential is sketched in Fig. 2-11. It is clear, that the eigenvalues of this potential are lower than of the original potential around x_0 as the potential is lower and broader than the original potential for a harmonic oscillator. A lower eigenvalue shows that nucleation is easier and hence occurs at a higher field $H_{c3} > H_{c2}$. The lowest eigenvalue is reached for $x_0 = 0.59\xi$. Saint-James and de Gennes were using tabulated Weber functions to obtain the value for the third critical field H_{c3}.[47] For an infinite surface parallel to the applied magnetic field, it is

$$H_{c3} = 1.695 \cdot H_{c2} = 1.695\sqrt{2}\kappa H_c. \tag{2.52}$$

If, however, the semi-infinite sample is turned with respect to the field direction, the value of the nucleation field changes gradually until it reached H_{c2} for the

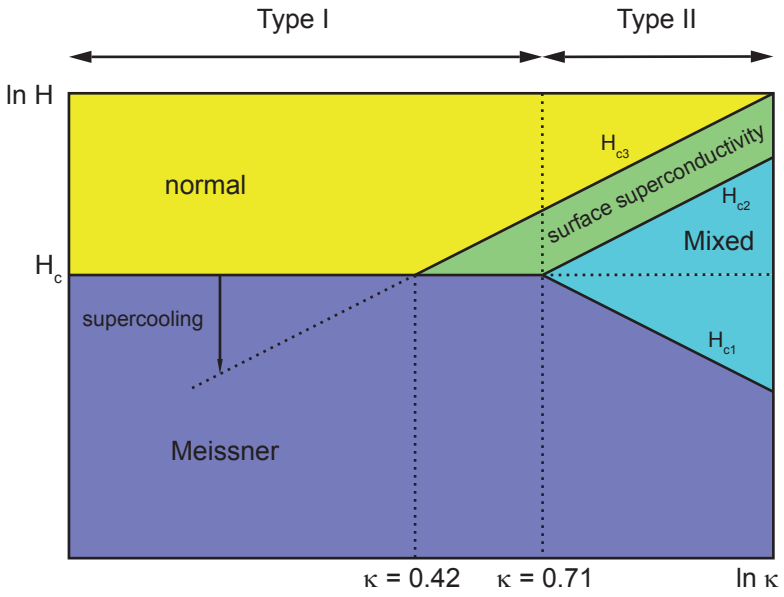

Figure 2-12: Phase diagram of the critical fields in relation to the thermodynamic critical field H_c for different values of κ.

surface orthogonal to the magnetic field. It is obvious, that this nucleation field will play an important role in real samples, especially in small samples, where the surface to volume ratio increases. These effects are discussed in Sec. 2.3.3.

2.2.8 Supercooling and superheating

Supercooling and superheating describes the metastability of the phase transition from normal to superconducting state and *vice versa*. Especially in type I superconductors, supercooling and superheating can become very pronounced. A phase diagram of the above discussed critical fields is sketched in Fig. 2-12. For a high κ type II superconductor, the Meissner state is destroyed by the first flux line which enters the sample at H_{c1}. For applied fields $H_{c1} < H_a < H_{c2}$ the sample is in the mixed state, where flux lines penetrate the sample, turning it locally normal. The bulk of the sample turns normal at H_{c2} and only a surface sheath stays superconducting for $H_{c2} < H_a < H_{c3}$. The phase transition between normal and superconducting is a second order phase transition and is hence continuous and shows no hysteresis (*cf.* Fig. 2-13b).

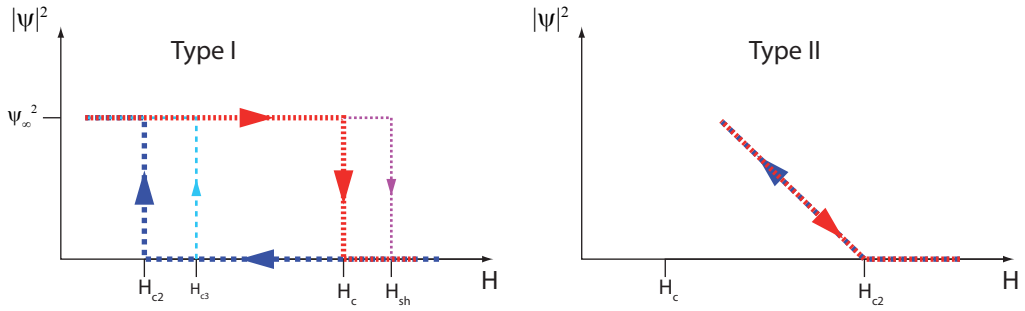

Figure 2-13: The different behaviour of the order parameter for type I and type II superconductors. In a type I superconductor it is $H_{c2} < H_c$. In a decreasing field, the normal state theoretically supercools until H_{c2} is reached, where the whole sample turns to the Meissner state ($|\psi|^2 = \psi_\infty^2$). In a real sample and if $H_{c3} > H_{c2}$ however, supercooling only applies until H_{c3} is reached. Changing the sweep direction to an increasing field, a real sample stays superconducting until the superheating field $H_{sh} > H_c$ is reached. In a type II superconductor on the other hand, with $H_c < H_{c2}$, a second order phase transition occurs at H_{c2} and $|\psi|^2$ increases gradually.

Supercooling

The phase transition in a type I superconductor with an applied magnetic field is a first order phase transition and is hence supercooled. An infinite sample with $\kappa < 0.71$ in a decreasing magnetic field supercools until the nucleation field H_{c2} is reached. When nucleation starts in a type I superconductor, superconductivity spreads through the whole sample and the order parameter jumps discontinuously and non reversibly from $|\psi|^2 = 0$ to $|\psi|^2 = \psi_\infty^2$. If the field is increased, the superconducting state is stable up to H_c, where the order parameter jumps from the bulk value to zero. For samples with $\kappa < 0.42$ and hence $H_{c3} < H_c$ supercooling occurs only until H_{c3} is reached. This is explained by the fact, that once superconductivity nucleates at the surface of these samples, superconductivity spreads into the rest of the sample and establishes superconductivity everywhere in the sample. Supercooling down to H_{c2} in a real sample with $\kappa < 0.42$ is only possible if the surface of the sample is treated in a way to suppress surface superconductivity. This can be done *e.g.* by plating the surface with a normal conducting material.[34,48] In this case the order parameter at the surface of the sample is supressed and superconductivity tends to nucleate in the bulk rather than at the surfaces.

Superheating

Another effect of the first order phase transition of a type I superconductor is superheating of the superconducting state. Superheating means, that the field is increased to a value $H_a > H_c$, so that the energy of the superconductor is greater than the energy of the normal state and the transition is delayed. This is caused by an effective surface barrier which opposes the entry of flux into the superconductor. The effect of superheating on the behaviour of the order parameter in a type I superconductor is also shown in Fig. 2-13. In a type I superconductor, superheating affects H_c, while in a type II superconductor, the field H_{c1}, where flux first penetrates is affected.

Although superheating is an effect mainly observed in type I superconductors, the first discussion of the surface barrier, which is mainly responsible for superheating, was on a high κ type II superconductor.[49] Bean and Livingston considered the forces that act on the first flux line that enters a superconductor with $\kappa \gg 1$, in an increasing magnetic field, in the Meissner state. The forces that lead to the so called Bean-Livingston barrier are sketched in Fig. 2-14. Two competing forces act on the vortex in the superconductor, close to the surface. The Meissner currents (J_s) along the surface of the superconductor exert a repulsive Lorentz force on the flux. The force

$$F_C = J_s(x)\Phi_0, \tag{2.53}$$

attempts to move the vortex further into the material.[44] The current $J_s(x)$ decays exponentially into the sample and is a function of the applied field H_a and the distance x from the vacuum/superconductor interface

$$\begin{aligned} J_s(x) &= J_{s0}e^{-x/\lambda} \text{ with} \\ J_{s0} &= \tfrac{H_a}{\lambda}. \end{aligned} \tag{2.54}$$

The force between the interface and the vortex is constructed by using its mirror image, symmetrically positioned outside the sample.[50] The resulting force between the vortex and the interface, respectively its mirror image, is

$$F_M = -\frac{\Phi_0^2}{2\pi\mu_0\lambda^3} K_1\left(\frac{2x}{\lambda}\right), \tag{2.55}$$

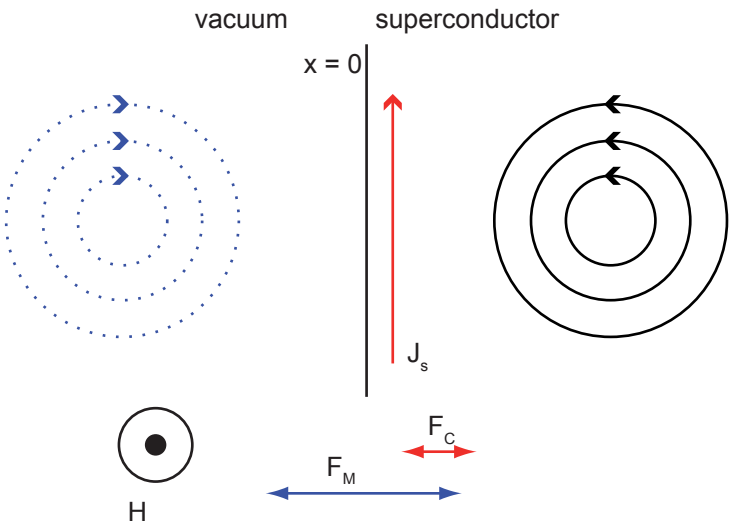

Figure 2-14: A single flux line close to the vacuum-superconductor interface. The force $\vec{F_C}$ between the supercurrents along the surface and the vortex is repulsive, while the force $\vec{F_M}$ between the vortex and its mirror image is attractive.

where $K_1\left(\frac{2x}{\lambda}\right)$ is the Bessel function.[44] The closest distance between vortex and interface is $x = \xi$. By further approximating the Bessel function for small x to

$$\lim_{x\to 0} K_1(x) = \frac{1}{x} \tag{2.56}$$

Eq. (2.55) simplifies to

$$F_M = -\frac{\Phi_0^2}{2\pi\mu_0\lambda^3\xi} \tag{2.57}$$

and one gets the field $H_s^{\lim}$ in the limit for $\xi \ll \lambda$. This is met for a type II superconductor with $\kappa \gg 1$, where the two forces are equal to

$$H_s^{\lim} = \frac{\Phi_0}{4\pi\mu_0\xi\lambda} = \frac{H_c}{\sqrt{2}} \tag{2.58}$$

which is referred to as the London approximation. Although this approach is useful to explain the basic principles of superheating, it is not able to fully explain the superheating field. The above approach assumes the London equations to apply everywhere in the sample, except from a region around the the vortex core with a radius ξ. In addition, close to the field H_s where flux starts to penetrate, the Cooper pair density n_s close to the surface deviates from the value in the

bulk and $|\psi|$ is greatly reduced.

De Gennes considered this reduction of the order parameter at the surface for the limit $\kappa \gg 1$,[51] and he found that the maximum field for which a solution exists is

$$H_s = H_c \tag{2.59}$$

where the reduced order parameter $f = \psi/\psi_\infty$ vanishes at the surface.

The Orsay group later used this approach to calculate the superheating field for a type I superconductor with $\kappa \ll 1$.[52] The boundary conditions can be simplified, as if $\lambda \ll \xi$ for $x < \lambda$ the order parameter is nearly constant and for $x > \lambda$ the magnetic field can be omitted. The field found by this approach is the κ dependent superheating field

$$H_{sh} = \kappa^{-\frac{1}{2}} 2^{-\frac{1}{4}} H_c. \tag{2.60}$$

In this approximation, the superheating field diverges to ∞ as $\kappa \to 0$.

This high barrier for small κ is apparent if one considers that for $\kappa \ll 1$ we have $\lambda \ll \xi$. The size of a Cooper pair, the size ξ where $|\psi|$ changes is here much larger than the distance to which the magnetic field penetrates the sample. The interaction between the applied field and the Cooper pair density hence is suppressed.

This approximation was qualitatively confirmed by numerical calculations of Matricon *et al.*.[53] Their numerical solution, to the same problem considered by the Orsay group, leads to a higher field, especially for larger values of κ (*cf.* Fig. 1 in Ref[53]). Comparing this calculation with the with the simplified form of equation (2.60), one finds that the behaviour towards the limits ($\kappa \to 0$ and $\kappa \to \infty$) are equal for the two calculation methods. More recently in 1996, Parr *et al.* and Dolgert *et al.* confirmed the calculation by Matricon with state of the art simulations.[54–56]

Experimentally, supercooling and superheating on type I materials was extensively studied amongst others by Doll *et al.* and Feder *et al.*.[57–60] They studied tin and indium spheres with different surface treatments. Especially for super-

heating, the surface treatment is of great importance. Local fluctuations, caused by surface imperfections, in the Cooper pair density can change the barrier energy and hence facilitate flux entry. It was found, that the influence of these surface imperfections vanishes, if they become small compared to ξ and/or λ. Also, changing the order parameter, by changing the boundary conditions at the interface, *i.e.* changing the S/I interface to a S/N interface by plating the superconductor with *e.g.* copper or gold, influences the barrier and destroys superheating of the superconducting state.

2.3 Superconductivity in mesoscopic samples

In the last section (Sec. 2.2) the general theory of bulk superconductivity was introduced. The BCS theory or the London and Ginzburg-Landau equations are important and valuable tools for the investigation of the properties and effects apparent in superconducting samples. However, some of the most interesting and striking effects of superconductivity are found in mesoscopic samples. A sample is said to be in the mesoscopic regime if its size is of a similar order as the superconducting length scales, namely ξ and λ. As both of these properties are temperature dependent, and increase as T_c is approached, the sizes where mesoscopic effects are observed also vary with temperature and very close to T_c even comparatively large samples show mesoscopic behaviour. For tin, which is extensively studied in this work, samples of the order of 1 µm show pronounced mesoscopic behaviour close to T_c.

In this section, the focus is on discussing effects which occur due to the geometry of the sample and which are important in order to understand the experimental results.

2.3.1 The demagnetising factor and the intermediate state

The demagnetising factor

Strictly speaking the demagnetising factor is not limited to mesoscopic samples, but as a geometry controlled effect fits best in this section.

In Sec. 2.2.5 it was shown that for a type I superconductor the interface energy is positive and that usually N/S interfaces are avoided. However, under certain circumstances the energy that has to be brought up to form the interface is lower than the energy which is needed to keep the sample in the Meissner state. In that case, normal domains form inside the sample to minimise the overall energy. The energy which is needed to keep the sample field free depends on the geometry of the sample. The demagnetising factor takes the geometric effects into account.

Fig. 2-15a shows how the field lines are bent around the ellipsoid sample when the sample is in the Meissner state. At the points furthest away from the centreline of the field, "the equator", the magnetic field has a local maximum, while at the points facing to and away from the field,"the poles", the magnetic field has a minimum. As soon as the surface field H_s (*cf.* Fig. 2-15b), which is tangential to any point of the sample, exceeds the critical field, the superconducting state is destroyed. For an ellipsoidal sample such as the one in Fig. 2-15a, this is in a band around the equator of the sample. For rectangular shapes (Fig. 2-15c) this happens at the acute corners of the sample.

If a magnetic field $\vec{H}_a$ is applied to a material, the sample is magnetised and hence generates a magnetisation $\vec{M}$. The magnetisation in turn causes surface currents which generate the, shape dependent, demagnetising field $\vec{H_D}$ which opposes $\vec{H}_a$ and $\vec{M}$. The surface field on the inner surface $\vec{H}_i$ in the sample is the superposition of these fields:

$$\vec{H}_i = \vec{H}_a + \vec{H_D} = \vec{H}_a - \eta\vec{M}, \tag{2.61}$$

with the demagnetising factor η, where $0 < \eta < 1$ depends on the shape and size of the sample.

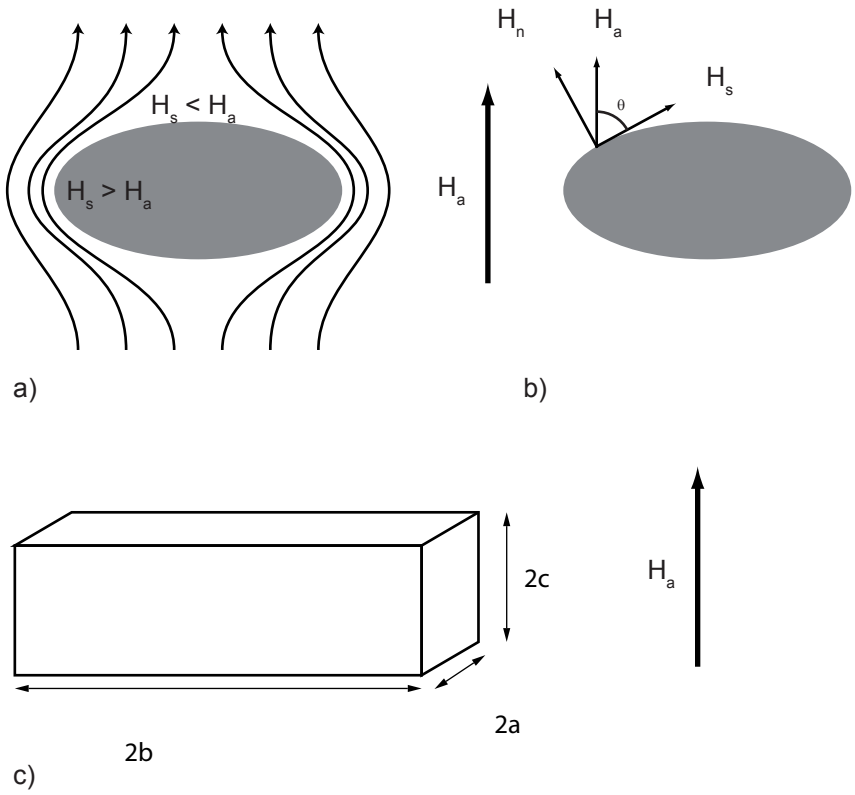

Figure 2-15: A superconducting ellipsoid in an applied field $\vec{H}_a$. The surface field of the sample $\vec{H}_s$ has the highest value at the edges of the sample and is lowest at the centre of the sample, facing the direction of the applied field. The components normal to the surface, $\vec{H}_n$, and parallel to the surface, $\vec{H}_s$, are indicated in (b). The solution by Chen *et al.* uses the geometry shown in (c).[61,62]

The flux density $\vec{B}$ is defined by the internal field and the magnetisation as

$$\vec{B} = \mu_0 \left(\vec{H}_i + \vec{M} \right) \tag{2.62}$$

which, rearranged, leads to

$$\frac{\eta \vec{B}}{\mu_0} + (1 - \eta)\, \vec{H}_i = \vec{H}_a. \tag{2.63}$$

In the Meissner state, it is $\vec{B} = 0$ for a superconductor and hence Eq. (2.63) yields the internal field

$$\vec{H}_i = \frac{\vec{H}_a}{(1 - \eta)}. \tag{2.64}$$

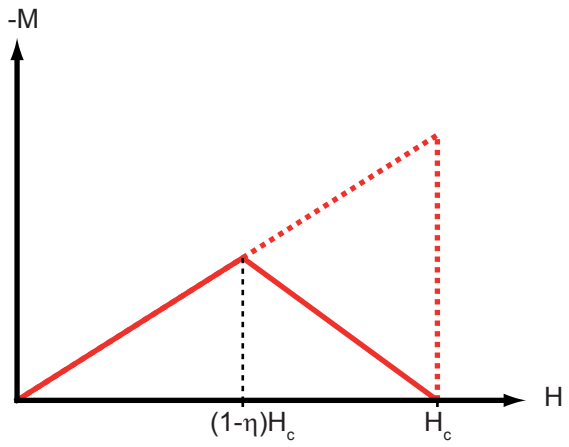

Figure 2-16: The magnetic phase diagram for a type I superconductor including an intermediate state. For an applied field $(1-\eta)H_c < H_a < H_c$ the superconductor is in the intermediate state.

The decisive field for the retention of superconductivity is the internal field $\vec{H}_i$ and if $H_i = \left|\vec{H}_i\right| > H_c$, that is ignoring any supercooling and superheating at this moment, the Meissner state is, at least partially, destroyed. The resulting magnetisation curve is shown in Fig. 2-16, where the Meissner state breaks down at $H_a = (1-\eta)H_c$ and the sample enters the intermediate state, which, obviously, has a lower magnetisation than the Meissner state.

Two extreme cases can be considered.

(i) An infinite cylinder or a thin plate with a field parallel to the long axis/plane of the plate. Here the surface field is basically the applied field, with a vanishing perpendicular component, which is not strongly bent around the sample and hence $\eta = 0$.

(ii) For the same sample with the applied field perpendicular to the long axis/-plane of the plate, the field cannot surround the sample and hence any arbitrarily small field penetrates it and the sample has a demagnetising factor of $\eta = 1$. The sample is always in the intermediate state. A pure Meissner state cannot exist for this geometry.

For other shapes, the demagnetising factor can be calculated analytically or numerically.[63,64] For example the demagnetising factor for a sphere is $\eta_{\text{sphere}} = \frac{1}{3}$.

The usual approach is to calculate the demagnetising factor for an ellipsoidal shape, which is analytically possible. For more complex shapes, the demagnetising factor can still be calculated, either by using an inscribed ellipsoid, or by trying to find an exact solution for a certain shape.[65] Joseph *et al.* used a series expansion to calculate the demagnetising factor for a range of shapes,[66–68] while Chen *et al.* found a method to analytically calculate the demagnetising factor for long rectangular rods and rectangular prisms.[61,62,69] The demagnetising factor after Chen *et al.* for a rectangular prism with the side length $2a \times 2b \times 2c$ (*cf.* Fig. 2-15c) has the form

$$N_f = \frac{2}{\pi} \arctan \frac{4ab}{c\sqrt{4a^2 + 4b^2 + c^2}} + \frac{c}{2\pi ab} \left[F_1 + F_f\left(a, b\right) + F_f\left(b, a\right) \right], \tag{2.65}$$

with

$$F_1 = \sqrt{4a^2 + c^2} + \sqrt{4b^2 + c^2} - \sqrt{4a^2 + 4b^2 + c^2} - c \quad \text{and} \tag{2.66a}$$

$$F_f(u, v) = u \ln \frac{c^2 \left(8u^2 + 4v^2 + c^2 + 4u\sqrt{4u^2 + 4v^2 + c^2}\right)}{\left(4v^2 + c^2\right)\left(8u^2 + c^2 + 4u\sqrt{4u^2 + c^2}\right)}. \tag{2.66b}$$

These equations were used to calculate the exact demagnetising factor for the tin rod samples in this work.

The intermediate state

It was shown above, that any real sample has a demagnetising factor $\eta > 0$ and as a consequence enters the intermediate state at an applied field $H_a = (1 - \eta)H_c$. In Fig. 2-17 an infinitely long superconducting slap is shown with bundles of flux penetrating the slab and forming normal regions in a laminar pattern. In the normal regions the field has a strength H_n which is somewhat less than the critical field H_c. In contrast to the domains in a type II superconductor the domains usually contain a large number of flux quanta Φ_0, although the N/S interface of these domains is accompanied by an energy penalty due to the positive surface energy of the interface. As was shown earlier in Eq. (2.43) the

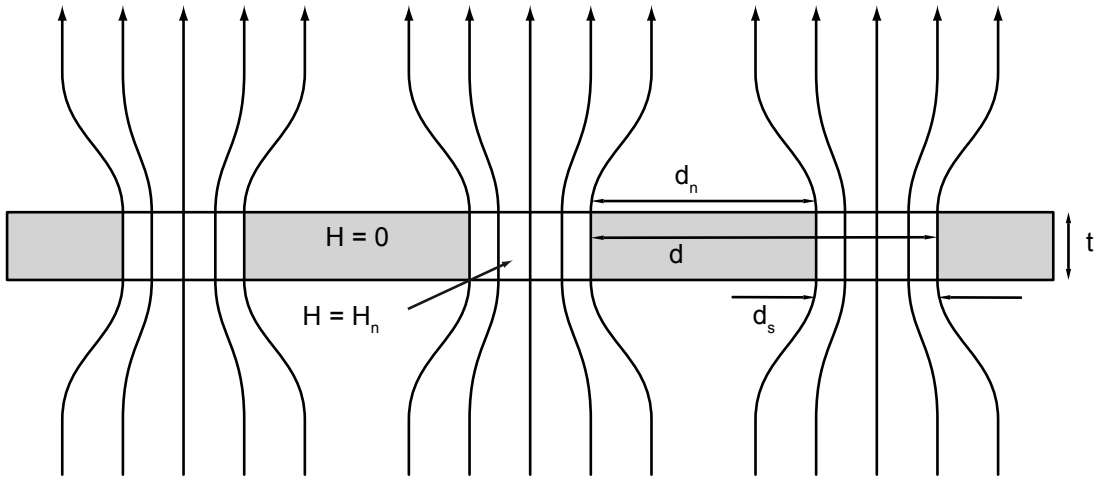

Figure 2-17: The intermediate state in a type I superconductor. The superconductor of thickness t is penetrated by normal domains. Outside of these normal domains with $H = H_n$, the superconductor is in the Meissner state ($H = 0$). d_n (d_s) is the size of the normal (superconducting) domain and d is the overall period of the domains.

energy connected with the interface is

$$F_1 = \frac{1}{2}\mu_0 H_c^2 \delta \frac{2t}{d}, \tag{2.67}$$

where $\delta = \xi - \lambda$ is the wall energy parameter and $\frac{2t}{d}$ the area of the interface per period d in the sample. As type I superconductors are considered, this term is always positive. On the other hand, it costs energy to form a non uniform magnetic field, *i.e.* bending the field lines, which surrounds the superconductor. The relaxation of the field to uniformity by letting flux penetrate through the normal domains of the sample, decreases the free energy and is hence opposing the interface energy F_1. This energy governed by the field H_n in the normal regions and the periodicity d of the S/N pattern, is expressed as

$$F_2 = \frac{1}{2}\mu_0 H_n^2 2d \cdot f\left(\tilde{h}\right) \tag{2.68}$$

with $f\left(\tilde{h}\right)$ being a function of the reduced field $\tilde{h} = \frac{H_a}{H_c}$ which has to be solved numerically.[70]

However, it is possible to approximate this energy by looking at the field just above the surface for the case that the field is uniform and the case where it is

not. Defining the fraction of normal regions in the superconductor as $\rho_n = d_n/d$ and noting that there is no field above the superconducting parts, the energy density becomes

$$F_2^{\text{non-uni}} = \frac{1}{2}\mu_0 \rho_n H_n^2. \tag{2.69}$$

The flux applied through one period d is equal, whether the field is uniform or non uniform. Assuming the length l of the domain,

$$\Phi_0 = H_a l d = H_n l d_n, \tag{2.70}$$

and so $H_a = \rho_n H_n$ which leads to the second contribution to the energy, the energy density of the uniform field

$$F_2^{\text{uni}} = \frac{1}{2}\mu_0 H_a^2 = \frac{1}{2}\mu_0 \rho_n^2 H_n^2. \tag{2.71}$$

The difference of the two energy contributions at the surface $\Delta F_2^{\text{surface}}$ is now

$$F_2^{\text{non-uni}} - F_2^{\text{uni}} = \frac{1}{2}\mu_0 \left(\rho_n - \rho_n^2\right) H_n^2 = \frac{1}{2}\mu_0 \rho_n \rho_s H_n^2, \tag{2.72}$$

where $\rho_s = d_s/d = 1 - \rho_n$ is the superconducting fraction of the domains. To get the energy density one has to multiply the surface contributions by the length it takes the field lines to relax. This "healing length" L as introduced by Tinkham is of the order of the lesser of d_n and d_s and is approximated as $L = d\rho_s\rho_n$ and hence

$$F_2 = \mu_0 \rho_n^2 \rho_s^2 H_n^2 d. \tag{2.73}$$

The minimum of the sum $F_1 + F_2$ with respect to d gives the optimum length of the laminar domains

$$d = \frac{\sqrt{t\delta} H_c}{\rho_n \rho_s H_n} \approx \frac{\sqrt{t\delta}}{\frac{H_a}{H_n} - \left(\frac{H_a}{H_n}\right)^2}. \tag{2.74}$$

The function $d\left(\frac{H_a}{H_c}\right)$ is shown in Fig. 2-18. The function is plotted for three different thicknesses $t = 0.5$ µm, $t = 1$ µm and $t = 2$ µm and for a $\delta = 0.2$ µm, using ξ and λ from Tai *et al.*.[71] For $H_a/H_n \approx 0.5$, the domain pattern has the smallest lateral period, which is of the order of the thickness t. For the values used for the graphs in Fig. 2-18, there is enough space in a sample of typically

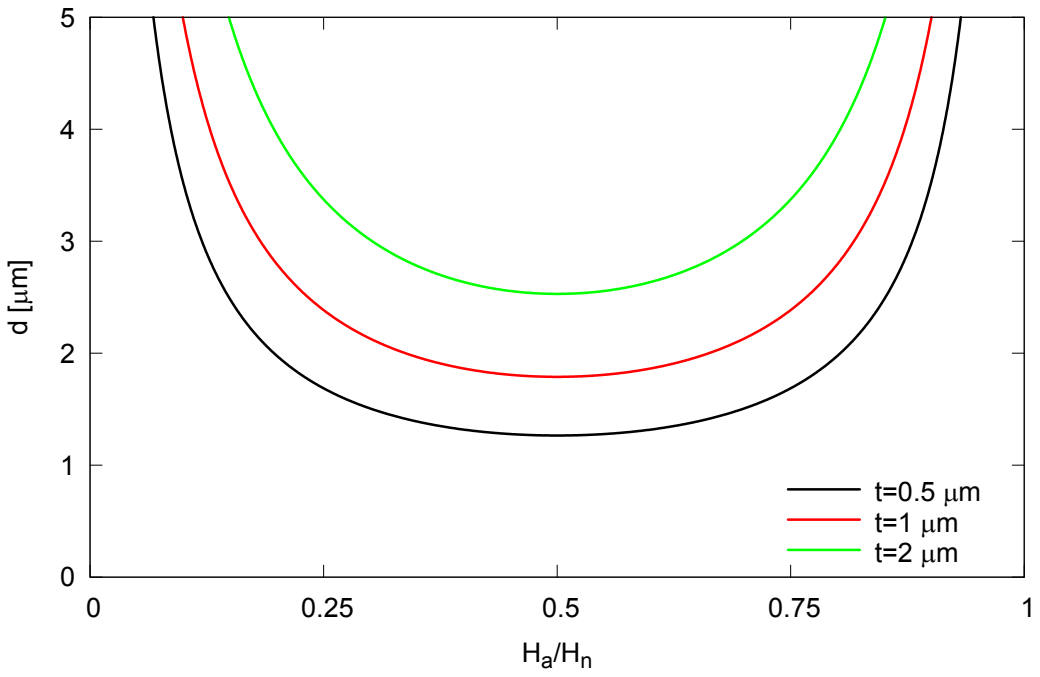

Figure 2-18: Plot of the domain size from Eq. (2.74) for $\delta = 0.2$ µm and three different thicknesses t. For $H_a \approx \frac{1}{2}H_n$, the domain period d is of a similar order to the thickness of the sample.

1 µm in size to form the intermediate state. Only as T_c is approached, ξ and λ increase and so does δ. Above a certain temperature, even large samples will change from type I behaviour, inhibiting an intermediate state, to mesoscopic behaviour, where the sample size is smaller than the laminar domain period.

The critical field H_{cI}, where superconductivity is destroyed in the whole sample ($\rho_n \to 1$ and $\rho_s \to 0$) is also controlled by the surface energy and is somewhat lower than H_c, the critical field for the case of zero demagnetising factor. The free energy of the system for the optimal value of d is assembled from the volume free energies, scaled by their fraction of occurrence in the sample, plus the additional surface energy due to the formation of the N/S interface

$$f_I = \rho_s f_{s0} + \rho_n \left(f_{s0} + \frac{1}{2}\mu_0 H_c^2 + \frac{1}{2}\mu_0 H_n^2 \right) + \frac{F_1 + F_2}{t}. \tag{2.75}$$

Minimising this equation with respect to ρ_n one gets (due *e.g.* Ref.[35]) the field

inside the normal domains

$$H_n = H_c\sqrt{1 - 4\sqrt{\frac{\delta}{t}}\frac{H_a}{H_c}}, \tag{2.76}$$

which is just $H_n = H_c$ for $H_a = 0$ and decreases for increasing H_a to a value of

$$H_{cI} = H_c\left(\sqrt{1 + \frac{4\delta}{t}} - 2\sqrt{\frac{\delta}{t}}\right). \tag{2.77}$$

The field $H_{cI} < H_c$ was proven experimentally for comparatively large cylinders.[72] For films much thicker than the superconducting lengthscales, *i.e.* $t \gg \delta$, the expression for H_{cI} can be simplified to

$$H_{cI} \approx H_c\left(1 - 2\sqrt{\frac{\delta}{t}}\right), \tag{2.78}$$

which is in good agreement with experiments on films with thicknesses on the order of µm or even mm.[73–75]

The limiting case of equation. (2.78) is, that H_{cI} vanishes for very thin films. This, however, is not observed in real samples, as very thin films change in behaviour from type I to type II. Pearl showed that for thin films with $t \approx \lambda$ the approximately infinitessimally thin and hence two dimensional current sheath results in a long range repulsive force between single vortices. This is further discussed in Sec. 2.3.3.

2.3.2 The geometrical barrier

The demagnetising factor introduced in Sec. 2.3.1 accounts only for the general shape of the sample and fails to account for the effects due to corners of the sample, or for very flat samples.

A first close investigation of the effect of different geometries on the penetration field H_p was performed by Provost *et al.*.[76] The group studied the penetration field for small, thin Pd discs, which show an irreversible behaviour when entering

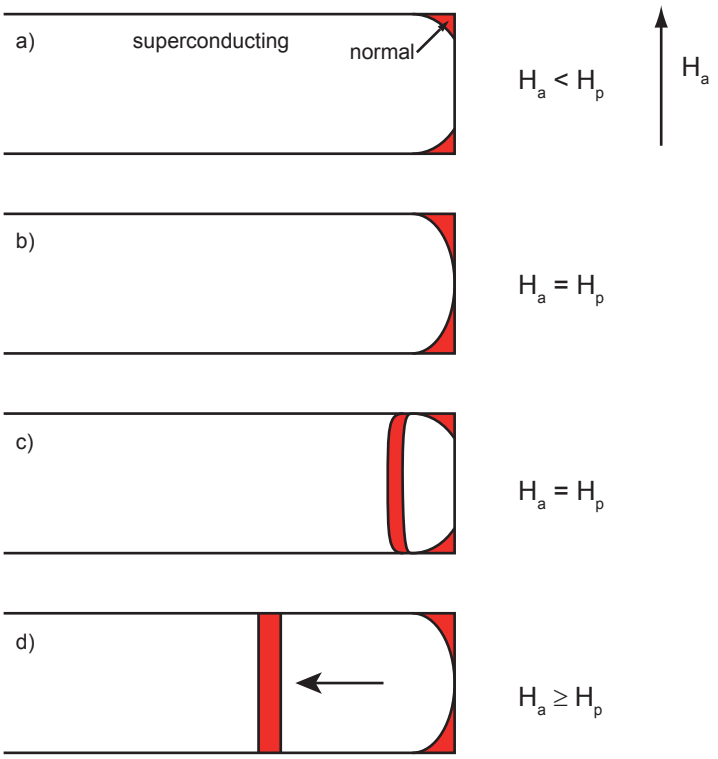

Figure 2-19: Flux penetration into a sample with rectangular cross-section in a perpendicular field. Superconductivity penetrates first at the corners (a and b), but above a field $H_a > H_p$ flux penetrates these corners and migrates into the sample.

the intermediate state. The demagnetising factor for a thin disk of diameter d and thickness t with $t/d \ll 1$ is approximated as $\eta = 1 - t/d$. For the penetration fields, this gives $H_p \propto \frac{t}{d} H_c$. The experimental results, however, showed a dependence $H_p \propto \sqrt{\frac{t}{d}} H_c$ instead. This result is explained by Fortini *et al.*, who consider an arbitrarily shaped sample in an external field.[77,78]

Fig. 2-19 shows how a normal domain enters the sample. For fields lower than the penetration field H_p, only the corners of the sample are normal. If the applied field H_a is increased, the Meissner state becomes energetically unfavourable and a normal domain in the centre of the sample would be energetically more favourable. However, a domain cannot simply jump into the centre of the sample, but has to migrate into the centre from one of the corners. Once a threshold field H_p is reached (Fig. 2-19b), the normal corners are joined and flux can enter the sample, forming a normal domain. By letting the flux enter, the field at the cor-

ners is relaxed and the corners separate again, giving rise to a new barrier for the next flux to enter (Fig. 2-19c). The fresh normal domain then migrates towards the centre of the sample, minimising the excess energy in the field around the sample (Fig. 2-19d). Sharp corners facilitate this barrier, as the field has to penetrate these and turn the corners normal before flux can enter the sample. This extra amount of energy is saved in a sample with rounded edges. The energy a flux line costs, is proportional to its lengths. Hence in a cuboid, flat sample, the position of the domain is only controlled by the force due to the supercurrents, which drive it towards the centre of the sample. In an elliptical cross sectioned sample, however, the domain has to grow in length as it moves inwards. This energy just compensates the effect caused by the supercurrents.[79] This gives rise to an important difference in the behaviour. Once a normal domain is trapped in the Meissner state in a sample with a rectangular cross section, the supercurrents surrounding it move the domain to the centre of the sample and force it to keep its position. As this is the most stable state, additional energy is necessary to move the domain to the corner where it is able to leave the sample again. These two barriers cause a hysteresis in the magnetisation behaviour. For a sample with elliptical cross section however, there is no metastable state for the domain at a given field and the domain leaves at the same field where it enters the sample. This is exactly the effect Provost *et al.* measured for increasingly flat elliptical disks. This effect in type I superconductors was originally called "edge-pinning", which changed after a similar effect was observed and described for type II superconductors and it is now mainly referred to as the "geometrical barrier".[80,81] The effect occurs for samples of any size and for many different geometries.[82,83] This is a major difference to the superheating discussed in Sec. 2.2.8. Superheating occurs for almost perfect, defect free, interfaces and prevents any flux to enter the sample, while the above discussed geometrical barrier controls the behaviour of macroscopic normal domains.

2.3.3 The nucleation field in a thin film

The thermodynamic critical field H_c, as well as supercooling $H_{sc} = H_{c3}$ and superheating fields H_{sh} for bulk or semi infinite samples were discussed in Sec. 2.2.8.

While for these geometries, the surface plays a secondary role, in thin samples the boundary conditions change dramatically and the contribution of the surface becomes dominant. Especially for the case of very thin samples, $d \ll \xi$, the order parameter $|\psi|$, whose variations have a length scale of the coherence length, becomes basically constant everywhere in the sample. The same argument is valid for the penetration depth λ, when $d \ll \lambda$ the magnetic field is able to penetrate throughout the whole sample, preventing a Meissner state anywhere in the sample. In Sec. 2.2.4 it was shown that both parameters diverge as T_c is approached. Hence with increasing temperature, any sample becomes "thinner" with respect to the superconducting length scales.

For a flat sample, two extreme geometries are considered. H_a parallel to the long dimensions and H_a perpendicular to the long dimensions. The solution of the GL problem of these two cases was found by Tinkham *et al.*[84–86] For a field perpendicular to the plane of the sample, the critical field is identical to the nucleation field H_{c2} introduced in Sec. 2.2.6

$$H_{c\perp} = \sqrt{2}\kappa H_c. \tag{2.79}$$

However, this changes drastically for a thin film in a parallel field, where the resulting critical field is a function of the ratio between penetration depth and thickness of the sample $\frac{\lambda}{d}$ and is, especially for very thin films with $d \ll \xi$, strongly enhanced with respect to the thermodynamic critical field. It is

$$H_{c\parallel} = \sqrt{24}\frac{\lambda}{d}H_c, \tag{2.80}$$

while the phase transition is still of first order. Close to this value, the irreversible, due to supercooling and superheating effects, phase transition, becomes first reversible before, for even thinner samples with $d < \sqrt{5}\lambda$, the transition between superconducting and normal state becomes a second order phase transition (*cf.* also Sec. 5). If H_a is increased towards $H_{c\parallel}$, the order parameter ψ approaches zero continuously, while the effective penetration depth λ_{eff} diverges towards infinity. Experimentally, these fields were confirmed, amongst other materials, on thin tin films,[87,88] and on thin lead films.[89,90]

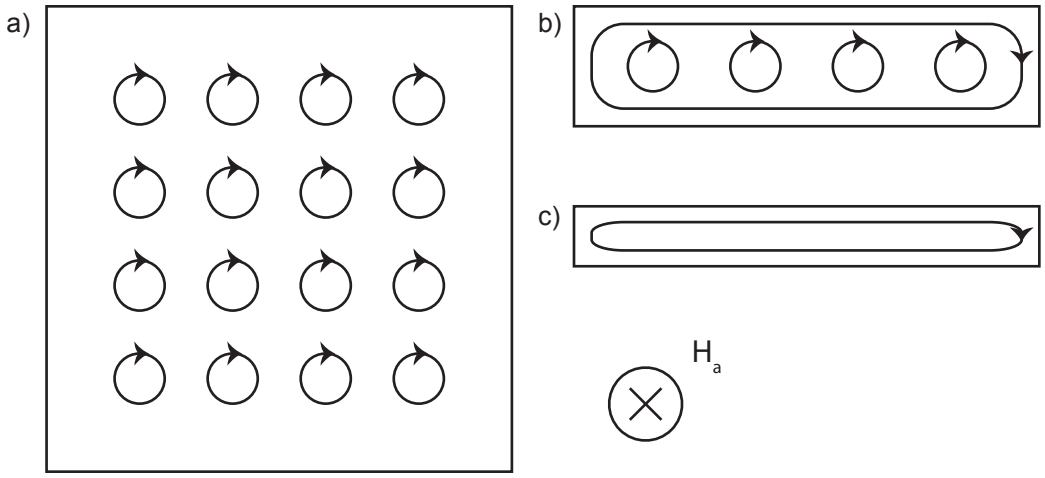

Figure 2-20: The sketch shows a thin film in perpendicular field (a) with a large number of vortices filling the sample. The samples in (b) and (c) show a sample in parallel field. In the sample of intermediate thickness (b) vortices are able to enter, additionally to the surface supercurrents, while this is not possible in the thin sample in (c). The field direction is perpendicular to the plane of the page.

If the thickness of the film $d \approx \xi$ is of the same order as the coherence length, the solution for $H_{c\|}$ under the assumption $\psi = \text{const}$ is no longer valid. The sketch in Fig. 2-20 shows the main difference in behaviour. Fig. 2-20a shows a sample in perpendicular field, where a large number of vortices enters the sample. Fig. 2-20b and c show a sample in parallel field, where for Fig. 2-20b it is $d \approx \xi$ and for Fig. 2-20c $d \ll \xi$. The main difference between the two latter cases is, that in a very narrow film, vortices are unable to enter and hence only surface currents maintain the superconducting state, while in slightly thicker samples, with a thickness of the order of the coherence length, vortices are able to enter.

In a sample with $d \gg \xi$ the nucleation field is defined by the surface superconducting field H_{c3} (Sec. 2.2.7). If, however, two surfaces are brought close together, the solution of the GL equations has to take both interfaces into account. If the size of the sample goes below the critical thickness $d_c \approx 2\xi$, the minima of the potential responsible for surface superconductivity fall together. Numerical calculations show that for $d < d_c$ with $d_c = 1.84\xi$ the minimum of the potential is in the middle of the sample, while for $d > d_c$, the minima are shifted towards the surfaces.[91–93]

2.3.4 The critical field of a slab

In a thin slab, one more dimension is omitted and the two geometries discussed above are basically combined in one single sample. With a magnetic field perpendicular to the long axis of the slab, the superconducting state is confined in both directions, perpendicular and parallel to the applied field. Additionally, in a real sample, the sharp, typically 90°, corners of the slab change the way the field can enter the sample.

Supercooling in a slab

The supercooling field marks the onset of superconductivity in a decreasing external field in a type I superconducting slab which is limited by surface superconductivity. The value for H_{c3}, derived in Sec. 2.2.7, is only valid for a semi infinite sample. This limitation is obviously not suitable for a thin slab with sharp corners. The problem is addressed, by using the boundary conditions of a wedge shaped sample.[94–96] Schweigert *et al.* found a numerical approximation for a wedge with a corner, having an angle α and a radius $r \gg \xi, \lambda$, to be

$$\frac{H_{c3}}{H_{c2}} = \frac{\sqrt{3}}{\alpha}\left(1 + 0.14804\alpha^2 + \frac{0.746\alpha^2}{\alpha^2 + 1.8794}\right). \tag{2.81}$$

The function is shown in Fig. 2-21. The value for a 180° wedge angle, which is basically a semi infinite sample, is identical to the value obtained in Eq. (2.52). It is

$$H_{c3}^{180^\circ} = 1.695 H_{c2}. \tag{2.82}$$

For a wedge with 90° angles, corresponding to a rectangular slab, the field is enhanced to a value

$$H_{c3}^{90^\circ} = 1.96 H_{c2}, \tag{2.83}$$

which is even further increased for an equilateral triangular sample with 60° corners

$$H_{c3}^{60^\circ} = 2.52 H_{c2}. \tag{2.84}$$

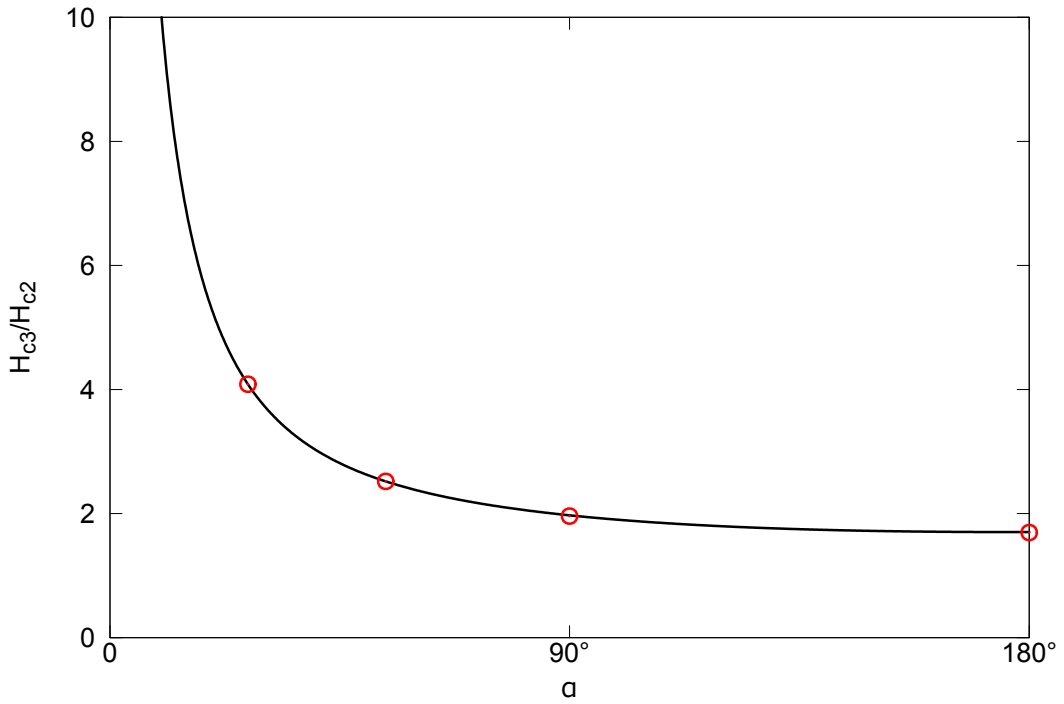

Figure 2-21: The graph shows the angular dependence $H_{c3}(\alpha)$ of the surface field as approximated by Schweigert *et al.*.[96] The red circles mark the values for a semi infinite sample with $\alpha = 180°$, a rectangular sample with $\alpha = 90°$, an equilateral triangle with $\alpha = 60°$ and a sharp $\alpha = 30°$ corner.

An additional effect arises from the cross sectional area of the sample, which is also addressed in the same publication. For a circle with an area $S < (2.33\xi)^2$ the maximum of the order parameter is in the centre of the sample, comparable to the solution of a thin film mentioned earlier. For an area $S > (2.33\xi)^2$ a vortex forms in the centre which changes the nucleation field. They showed that the behaviour is qualitatively similar for a square and triangular samples with different angles (*cf.* Fig. 1 in ref[96]).

These results indicate that the onset of superconductivity in a decreasing field takes place at larger fields if the samples have sharp corners.

Superheating in a slab

The superheating of the superconducting state, which is an effect of a microscopic surface barrier as seen in Sec. 2.2.8, is more pronounced in a mesoscopic slab, where the surface is more flawless than in large bulk samples. It is also clear that the simple model of the vortex trying to enter can only work if the sample is wide enough to contain a vortex. Numerical calculations of the superheating field for different slab widths have been performed by Landau and Rinder.[97] Especially close to the crossover from a first to a second order phase transition, which occurs at the critical thickness $d_c \approx \sqrt{5}\lambda$, the superheating field changes with the width of the sample. For the calculations, Landau and Rinder used a symmetric form of ψ in a slab of infinite length. For very thick slabs, the resulting field is identical to the field from equation (2.60) and decreases with decreasing thickness. For very thin slabs ($d \approx 10\lambda$) the dependence of H_{sh} on the GL parameter κ seems to vanish, and the calculations for two different values of κ join a common minimum of H_{sh} at $d \approx 4\lambda$. Further decreasing the size results in an increasing superheating field which becomes identical to H_c for $d < \lambda$ (*cf.* Fig. 3 in ref[97]).[98–100]

2.4 Superconductors in close contact

So far, all considered interfaces have been between superconductor and vacuum. The boundary condition for the order parameter ψ at these interfaces is simply the vanishing derivative of ψ. If, however, another material is in contact with the superconductor, the boundary conditions for ψ changes, so that ψ either is suppressed, or enhanced close to the interface. To account for the different cases, the surface extrapolation length b is defined and the new boundary condition is

$$\left.\frac{\partial\psi}{\partial x}\right|_{x=0} = \left.\frac{1}{b}\psi\right|_{x=0}. \tag{2.85}$$

In Fig. 2-22 the behaviour of ψ at an interface is shown for a vacuum/superconductor interface ($b = \infty$), an interface where ψ is suppressed ($b > 0$) as in a ferromagnet/superconductor interface and a superconductor/superconductor

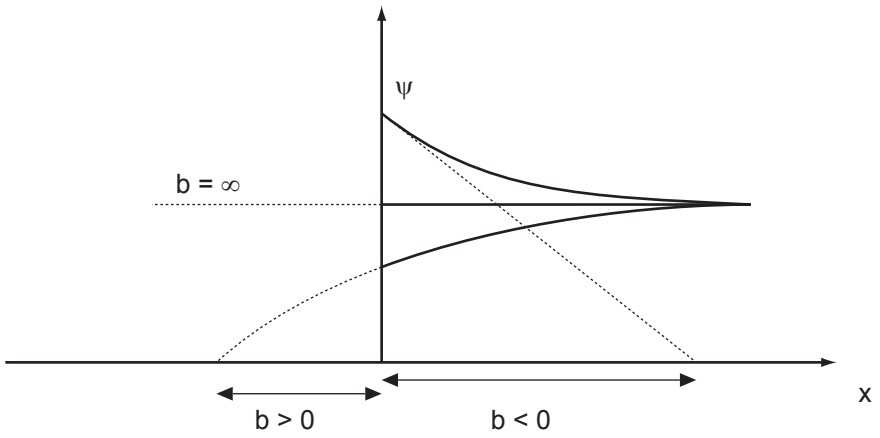

Figure 2-22: The surface extrapolation length b depends on the behaviour of the order parameter ψ at the surface of the sample ($x > 0$). $b > 0$ is a supression of ψ as in a superconductor/ferromagnet interface, $b < 0$ is an enhancement due to a superconductor/superconductor interface, where the superconductor in the $x < 0$ half space has a higher T_c and/or H_c and is hence "deeper" in the superconducting state. $b = \infty$ is a superconductor/vacuum interface.

interface where ψ is enhanced ($b < 0$). In conjunction with the framework of the GL equations these boundary conditions allow the simulation of any interface.

Considering the case where ψ is enhanced at the interface ($b < 0$), it is of major interest to investigate if superconductivity on one side of the interface can act as seed for superconductivity in the other material. Usually the image of "wetting" within a first order phase transition is used to describe this process.[101,102] If one considers a drop of liquid on a solid surface, depending on the surface energies between liquid and solid, the liquid can either wet the material, or remain as a drop on the surface. This is analogous to the situation of a superconducting phase in contact with a normal phase. In type I materials with low κ the superconducting phase spreads easily into the sample, which can be seen from the supercooling of a sample, which only occurs down to the surface field H_{c3}. In a decreasing field, as soon as the surface field H_{c3} is reached, the whole sample turns superconducting.

Examples of a negative surface extrapolation length b are *e.g.* the enhancement of the order parameter by changing the surface, which leads to the so called twinning plane superconductivity which were theoretically and experimentally

investigated.[103,104]

However, the interface between two different superconductors is theoretically explored in the framework of the GL equations by a number of groups, but experiments on these systems are very rare.[105–112] The results of the simulations for different values of b and ξ have in common that an increase in the critical field H_c, as well as in the critical temperature T_c is possible and is predicted to different extents. When two superconductors with different critical temperatures are in close contact, *e.g.* tin with $T_c = 3.72$ K and lead with $T_c = 7.2$ K, Cooper pairs are able to pass from the superconducting lead into tin, even if $H_a > H_c^{\mathrm{Sn}}$ and/or $T > T_c^{\mathrm{Sn}}$.

2.5 Superconductivity and ferromagnetism

2.5.1 Ferromagnetism

The last sections illustrate that superconductivity is usually incompatible with magnetic fields, as these tend to destroy superconductivity, by breaking the Cooper pairs. However, the addition or cancellation of magnetic fields can be used to suppress or enhance the effective magnetic field inside a superconducting material and hence affect the superconducting state.

Materials are called ferromagnetic if the material can be magnetised by an external field and keeps the magnetic field in the form of a permanent magnetisation $\vec{M}_{\mathrm{FM}}$, even when no external field is applied. The name derives from the Latin word for the element iron, and this effect is known since ancient times.

Ferromagnetism, is a special case of paramagnetism. The magnetisation of a sample is defined as

$$\mu_0 M = \mu_0 \chi H_0 = \chi B_0 \tag{2.86}$$

where χ is the magnetic susceptibility. With a susceptibility $-1 < \chi < 0$ the magnetisation opposes the external magnetic field. This is defined as diamagnetism, and a superconductor in the Meissner state is a perfect diamagnet (*cf.*

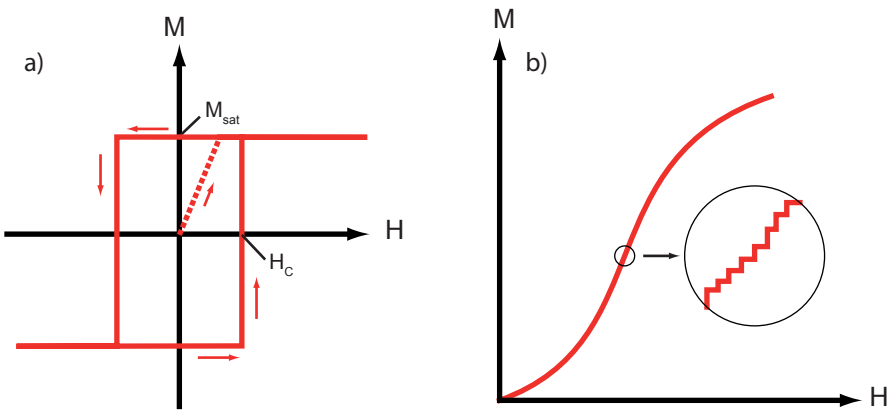

Figure 2-23: (a): A very simplified magnetisation curve for a soft ferromagnetic material. The magnetisation shows a clear hysteresis with the magnetisation changing from the saturation magnetisation $+|M_{sat}|$ to $-|M_{sat}|$ at the coercive field $-|H_C|$ and back at $+|H_C|$. (b) In a large, real sample, the switching process does not occur in one large step, but in many small steps. This is called the Barkhausen effect.[115]

Sec. 2.2.1) as it fully expels the external field. A positive susceptibility ($\chi > 0$) defines paramagnetism, where the magnetisation points in the same direction as the externally applied field. If, however, the magnetisation does not vanish after switching off the external field, the effect is called ferromagnetism.

Ferromagnetism occurs mainly in elements with an incomplete electronic shell such as the transition metals and rare earth elements. The spins of the unpaired electrons of adjacent atoms interact and align. This is caused by the so called exchange interaction which was firstly described by Heisenberg in the late 1920s.[113] The exchange interaction is a purely quantum mechanical phenomenon, which is a result of the Pauli exclusion principle.[114] It forbids identical quantum states for neighbouring atoms. In a ferromagnetic material, the parallel alignment of the spins, and hence the magnetic moments, leads to an energetically more favourable configuration than for antiparallel spin alignment.

A simplified magnetisation curve for a soft ferromagnet is shown in Fig. 2-23a. Coming from the pristine state ($H = M = 0$), the magnetisation increases with increasing field up to the saturation value M_{sat}. A further increase of the field has no effect on the magnetisation. Decreasing the field in our simple model has no effect on the sample magnetisation which stays constant at M_{sat}. Only as the

coercive field H_C[2] is reached, the sample jumps from $+M_{sat}$ to $-M_{sat}$ and hence swaps the direction of its magnetisation. This leads to the hysteretic behaviour seen in Fig. 2-23a. This simple model ignores a couple of effects which occur in a real sample. For the work at hand, the Barkhausen effect is of particular interest.[115] In a real sample, the process of switching magnetisation is less abrupt than shown in the sketch in Fig. 2-23a, however, and on a microscopic scale, the switching of single domains is visible as small steps in the magnetisation curve (Fig. 2-23b). These features were first seen by Barkhausen in 1919 after whom the effect is named.

[2]Not to be confused with the critical field H_c of a superconductor.

2.5.2 Shape anisotropy

Although a ferromagnetic sample can be magnetised in any direction by applying an external field, the energy needed usually differs for different axes. One can usually distinguish between the easy and hard axes of a magnet, where a small or large field is needed to magnetise the sample, respectively. The axes are controlled by the crystalline anisotropy and the shape of the sample. The exchange interaction due to the spin orbit coupling is not necessarily equal for different crystallographic axes, which results in a crystal lattice anisotropy of the magnetisation. For single crystal ferromagnets, this has to be taken into account. The ferromagnetic samples used in this work are all polycrystalline and hence the former effect is largely averaged out and not relevant here. The shape anisotropy, on the other hand, plays an important role in this work, where thin ferromagnetic films are used. In Fig. 2-24 two different geometries are shown. The argument is similar to the discussion of the demagnetising factor of a superconducting sample above in Sec. 2.3.1. The magnetisation of the sample causes magnetic polarisation charges on the sample surface which build up an additional field, opposing the external field. This stray field incorporates a certain amount of magnetostatic energy and the larger the surface is where these poles form, the higher this energetic cost. It is clear, that a magnetisation along the long axis (Fig. 2-24a) has the lowest and a magnetisation parallel to the short axis (Fig. 2-24b) has the highest amount of polarised surface. This leads to the formation of an easy axis along the long axis of the ellipsoid and a hard axis perpendicular to this.[116] This effect is strongest in thin films, where for most common materials the easy axis lies in the plane, while the hard axis points out of the plane of the material. For nickel, which is used in the experiments in this work, this conclusion is correct for sufficiently thick films. Perpendicular anisotropy is observed in thin nickel films with a thickness of 8 - 10 monolayers.[117] This is about two orders of magnitude thinner than the shell thickness of the crystals investigated in Sec. 7.

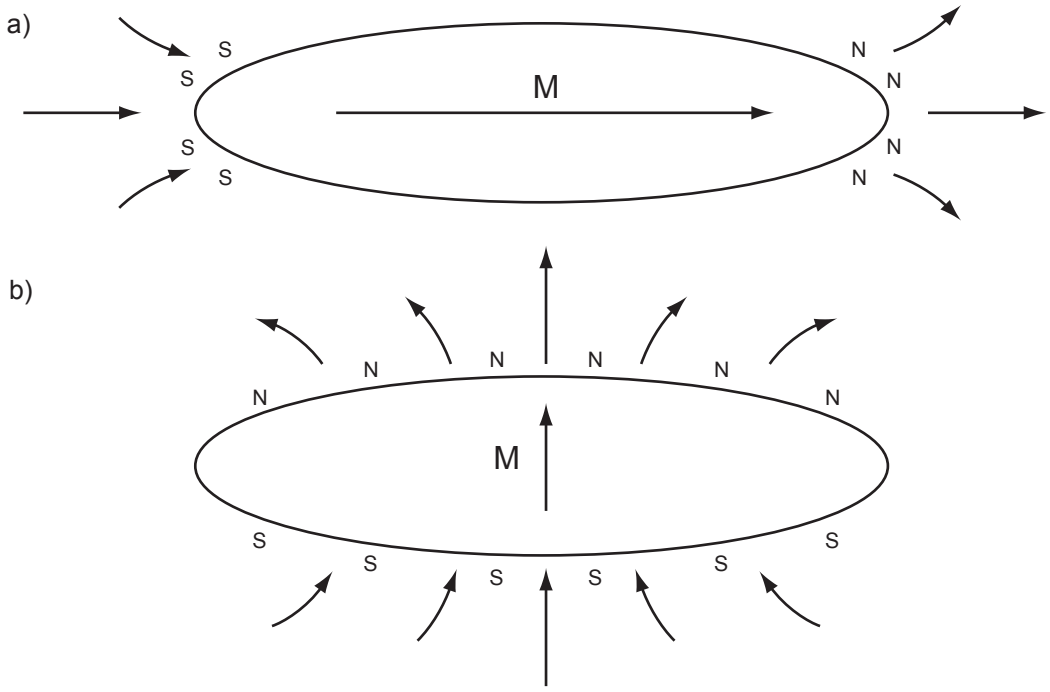

Figure 2-24: The shape anisotropy of magnetisation due to the different build-up of surface poles in an ellipsoid magnetised parallel (a) and perpendicular (b) to the long axis. Due to the smaller surface in the former case, this is energetically favoured.

2.5.3 Ferromagnet - superconductor interaction

The interaction between superconductors and ferromagnetic materials has been widely studied. Composite samples of superconducting and ferromagnetic materials are usually referred to as ferromagnetic superconducting hybrids (FSH).[118–122] The ferromagnetic material may be used *e.g.* as vortex pinning sites in thin samples,[121,122] or as magnetic dots on rod shaped samples.[123,124] Experimental studies, however, have been restricted to one-dimensional nanowires/nanorods,[125] two-dimensional layered structures[126–131] or arrays of ferromagnetic nanodots patterned on top of thin superconducting films.[132–135] Truly 3D systems with superconducting cores and ferromagnetic shells only recently became possible and are discussed later in this work.[136]

The main interaction between the superconducting and ferromagnetic materials is here due to the magnetic stray fields. This effect was correctly described by Jaccarino and Peter in 1962 after experiments by Clogston and Chandrasekhar.[137–139]

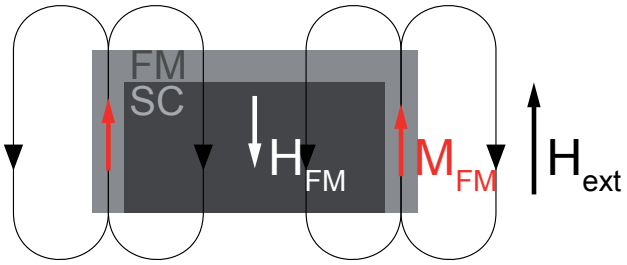

Figure 2-25: Interaction of a ferromagnetic shell with a superconducting core. The stray field H_{FM} caused by the magnetisation M_{FM} of the shell partially cancels the effect of the external field H_{ext}. The lowered effective field acting on the superconducting state, allows to maintain the Meissner state at fields much higher than H_c.[136]

In the first description of the Jaccarino-Peter effect, the authors describe the interaction between the spin of rare earth atoms in the materials and the external field which is hence compensated and the effective magnetic field is lowered. This gives rise to materials which are non-superconducting at fields $H = 0$ due to the internal field caused by the rare earth elements and only enter the superconducting state at field $|H| \gg 0$ when the field due to the ferromagnet is compensated and the effective internal field is lowered below H_{c2} for the material. Although the Jaccarino-Peter effect describes the interaction on a microscopic scale, the effect can easily be scaled up and instead of single spins, macroscopic domains can cause a field which opposes the externally applied field. In Fig. 2-25 a sketch shows the participating fields in a superconducting/ferromagnetic core/shell structure. In this simple sketch, the magnetisation of the top face is ignored as the predominant magnetisation of this part will be parallel to the film due to the shape anisotropy discussed above. The shell magnetisation, M_{FM}, causes a stray field H_{FM} which points in the opposite direction to the magnetisation. Here, the external field is parallel to the shell magnetisation and hence the fields H_{FM} and H_{ext} point in opposite directions. The effective field at the position of the core can now be lower than the critical field, even if the external field is larger than H_c. Applications of this macroscopic Jaccarino-Peter-like effect could be high field particle detectors, where superheated tin particles are currently used. Their working fields could be shifted to much higher values due to the field compensations,[140] other applications include superconducting memory devices.[141–143] In the Memory devices, proposed by Nemes *et al.*, the shell magnetisation is "written" with a high magnetic field and, depending on the magnetisation direction,

a low field would "read" either a normal or a superconducting core acting as a digital "0" or "1". The core-shell samples discussed in Chapter 7 exhibit exactly the necessary properties and could probably be adapted to be used in such applications.

Chapter 3

Electrochemistry

3.1 Introduction

Mesoscopic superconducting samples can be fabricated using a range of different methods.[144–149] A common technique is lithographic patterning, which can be used to get two dimensional samples.[150,151] A lithographic pattern, which is exposed in some form of resist, is used to either etch or deposit material in the mask. The samples are usually polycrystalline thin films, forming a mesa of a given shape. The acuteness and smoothness of the sample is hereby limited by the wavelength of lights and grain size of the materials used in the process (*cf.* Section 4.2). Additionally, polycrystalline thin films are always type-II superconductors.

The use of focused ion beams (FIB) to deposit material in defined shapes is another technique which is used to grow mesoscopic samples.[152] To deposit a metal with a FIB, a precursor is used which decomposes under the influence of the ion beam. It is almost impossible to remove all remains of the precursor, hence there is always some contamination of the precursor in the final sample. Although the FIB method can be used to grow three dimensional (3D) samples, the material is amorphous and contaminated with carbon.

Electrochemistry is a technique, where the growth of a crystal, from a solution of

dissolved metal ions, can be controlled. It is hence ideal to controllably fabricate 3D, single crystal samples with a wide range of sizes and shapes. Electrochemistry has been successfully used to fabricate superconducting and ferromagnetic samples.[153–156] The shapes that can be obtained from electrodeposition are however limited by the material and the set-up used. However, electrodeposition can be used to deposit a metal onto a template, *e.g.* in the fabricated holes of another material to form nanotubes,[157–159] or to plate another sample with a shell of controllable thickness.[136,160–162]

The history of electrochemistry began in the late 18^{th} century when Luigi Galvani experimented with frog legs and found the connection between certain chemical processes and an electrical current in 1780.[163] Scarcely 20 years later, Alessandro Volta developed the first battery which provided electrical energy from chemical processes. Luigi Brugnatelli was the first who used one of the batteries invented by Volta to electroplate gold in 1805.[164] In 1832, Faraday found the laws, now known as Faraday laws, which describe the proportionality between charge, mass and specific weight in electrolysis. This finding led to applications in modern electrochemistry.

The use of electrochemistry can be divided into two main areas. The active use, where current is used to control chemical reactions, and the passive use, where chemical reactions are used to provide available electrical energy. The latter is used in batteries and fuel cells and is of minor importance for the work described in this report. The former is mainly used to plate different metals for large scale industrial applications. Scaled down, these plating processes are able to fabricate structures in the range of single nanometres to several micrometers.

A metal which is immersed in pure water will form metal ions, which will enter into solution. The excess electrons are left in the metal and cause a charge in the bulk metal

$$\mathrm{M}_{(\mathrm{s})} \rightleftharpoons \mathrm{M}^{\mathrm{x}+} + \mathrm{x} \cdot e^{-}_{(m)}. \tag{3.1}$$

This charge prevents further ions from forming and going into solution. For most materials, this process comes to a halt after only a small amount of material is dissolved. The process can be controlled by controlling the amount of excess electrons in the metal. If electrons are drained, more metal ions can form and

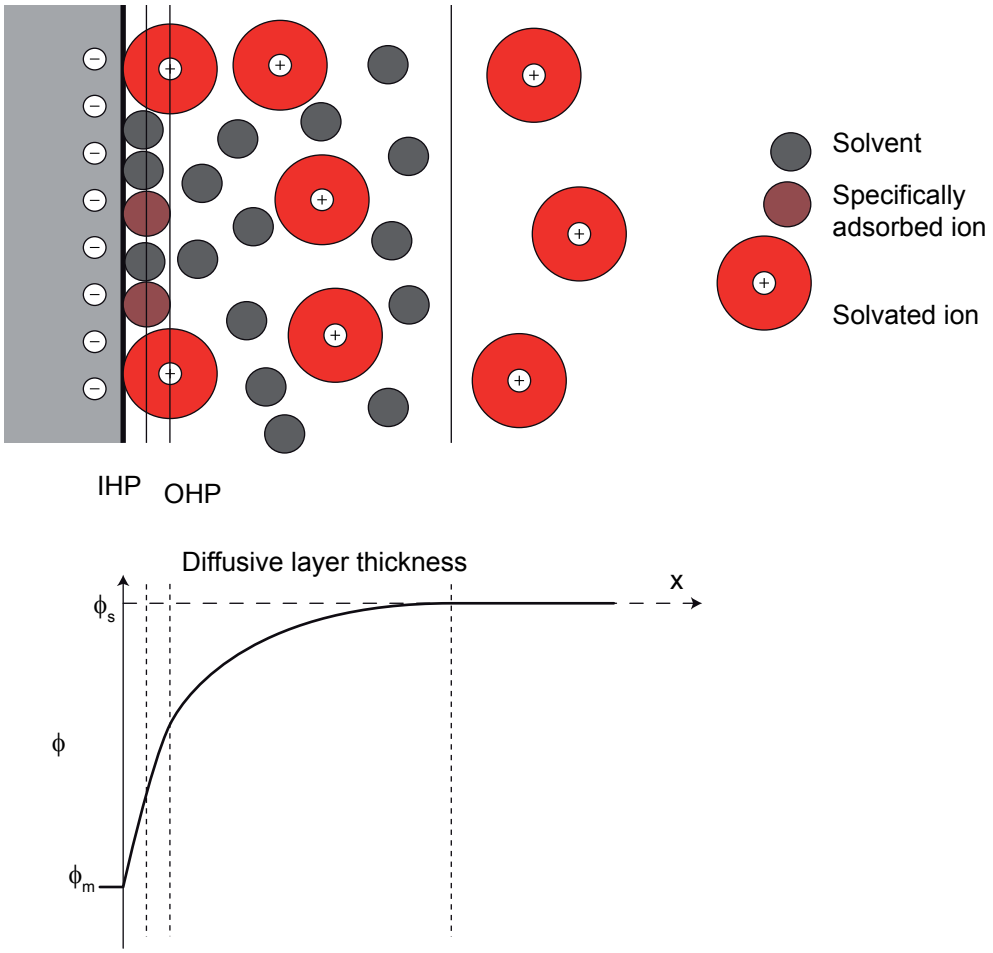

Figure 3-1: The electrode/solution interface as described by Grahame.[165] The main charge is between the electrode and the outer Helmhotz plane (OHP). The influence of the electrode is significant within the diffusive layer thickness. Specifically absorbed ions reach as close as the inner Helmhotz plane (IHP). The potential ϕ is sketched at the bottom, where the potential at the metal surface ϕ_m approaches a constant value ϕ_s in the bulk solution.

enter into solution. If, on the other hand, electrons are added to the metal, less ions are able to dissolve and ultimately the process can be reversed, reducing the metal ions in solution which will then precipitate as neutral atoms. Fig. 3-1 shows a sketch of the interface between the metal (electrode) and the solution (electrolyte). The free electrons in the metal and the free ions in the solution are spatially separated, the interface hence behaves similar to a capacitor. The surface of the electrode is covered with solvent molecules and specifically adsorbed metal ions. Specifically adsorbed ions are adsorbed directly on the surface with-

out a complete solvation sphere. The so called solvated ions have a complete solvation shell around them. If these are adsorbed, they are called nonspecifically adsorbed ions. Specifically adsorbed ions define the thickness of the Inner Helholtz Plane (IHP), while nonspecifically adsorbed ions define the Outer Helmholtz Plane (OHP).[165] The diffusive layer is defined as the region, where the influence of the electrode dominates the behaviour. The potential ϕ is sketched in the bottom of Fig. 3-1. The potential at the metal surface ϕ_m approaches the bulk solution value ϕ_s with increasing distance x.

In the diffusive layer, the electrostatic forces govern the movement of the ions, while at larger distances from the electrode electro neutrality exists. The thickness of the diffusive layer depends on the ion concentration, where a higher concentration means a thinner layer. A typical dimension of the diffusive layer is of the order of 10 nm.

3.1.1 Crystal nucleation and growth

Nucleation

Two bulk phases in an equilibrium will always try to stay in this equilibrium. If a force is applied, one phase will transform into another to keep the system in an equilibrium. In a system with only one phase, like the electrolyte, a driving force has to be applied to form a new phase. The system is in a supersaturated, or metastable state if the applied force is not strong enough to overcome the energy barrier to form a new phase. Well known supersaturated systems are superheated or supercooled liquids. Once the phase change starts to take place, the new phase will nucleate in small clusters.

The nucleation of one phase from another can be discussed using the Gibbs free energy G of the system.[166] Although originally used to describe the condensation of liquid from the vapour phase,[167–169] it also works for the nucleation of solids from liquids or solutions.[170,171] The total change of the Gibbs free energy ΔG consists of the surface excess energy ΔG_S and the volume excess energy ΔG_V. ΔG_S is a positive contribution to ΔG due to the interfacial tension between the

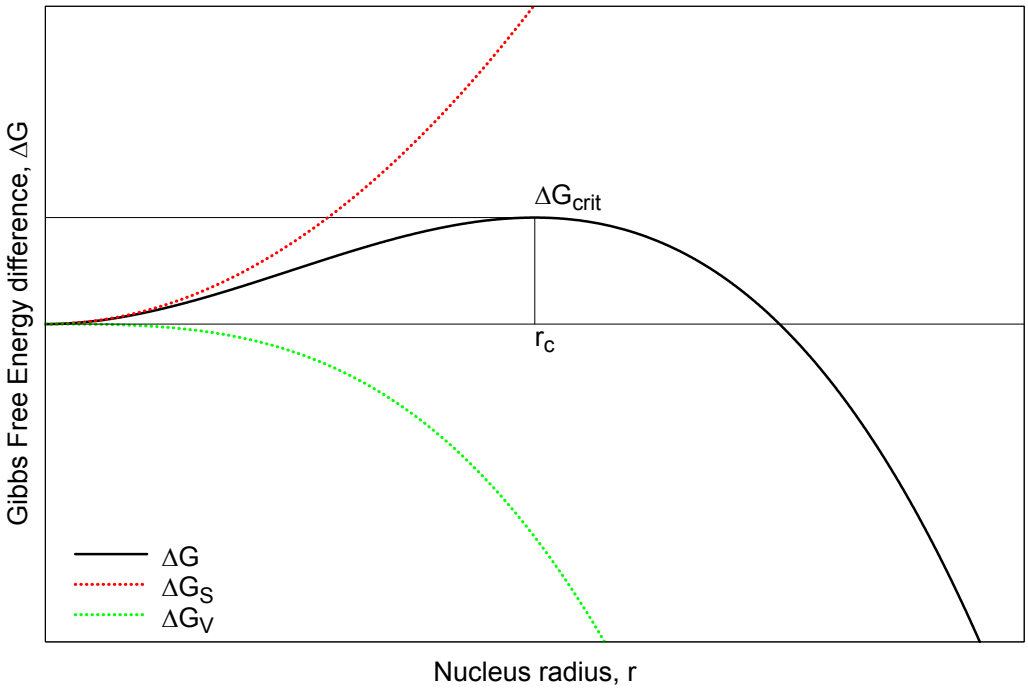

Figure 3-2: Free Energy diagram for nucleation. The Gibbs free energy as function of nucleus size. The positive surface contribution ΔG_S and the negative volume contribution ΔG_V result in a maximum critical Energy ΔG_{crit} for a critical nucleus radius r_c.[171]

nucleus and the supersaturated solution, while ΔG_V is the negative contribution of the bulk formation of the solid material. For a small, spherical particle the surface growth $\propto r^2$ while the volume growth $\propto r^3$. The difference in Gibbs free energy ΔG is

$$\begin{aligned} \Delta G &= \Delta G_S + \Delta G_V \\ &= 4\pi r^2 \gamma + \frac{4\pi}{3} r^3 \Delta G_v \end{aligned} \tag{3.2}$$

with the interfacial tension or surface energy γ and the free energy of formation of the bulk phase per unit volume ΔG_v. This function is shown in Fig. 3-2. For small r the quadratic surface term dominates, hence $\Delta G > 0$ and for large r, the cubic term of the volume dominates and hence $\Delta G < 0$. Differentiating Eq. (3.2) yields a critical radius $r = r_c$ where the maximum positive $\Delta G = \Delta G_{crit}$ is reached. A particle that tries to minimise its energy will shrink if it is smaller

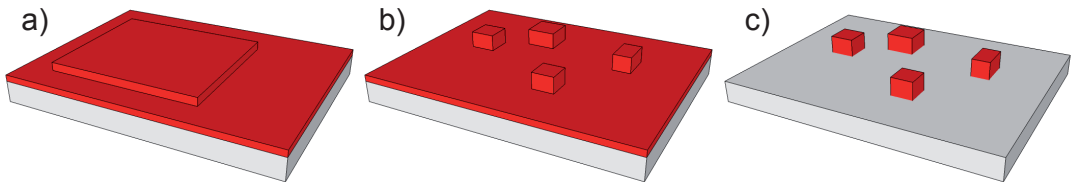

Figure 3-3: Illustration of the three different growth modi, Frank-van der Merwe (a), Stranski-Krastanov (b) and Volmer-Weber (c).

than $r = r_c$ until it disappears. Larger particles with $r > r_c$ will continue to grow to minimise their free energy.

The nucleation straight from bulk, without involvement of foreign particles acting as seeds for the nucleation, as shown above, is called homogeneous nucleation.[171] If, however, foreign particles (*i.e.* in the form of the electrode surface) are present, the nucleation is called heterogeneous nucleation. The latter usually yields a much higher nucleation rate and has a lower $\Delta G'_{crit} < \Delta G_{crit}$.[171,172] This is caused by the smaller surface contribution of a semi spherical nucleus that starts to grow at the surface of the electrode. Additionally, the surface of a real electrode/solution interface is not atomically flat. Steps, terraces and other inhomogeneities form cavities where the initial surface of a growing nucleus is considerably reduced.

Three distinct growth modes can be distinguished as illustrated in Fig. 3-3. The adhesion between the atoms and the surface of the electrode depends on a number of factors. The chemical bonds between identical metal ions and between metal ions and the electrode surface control how and where atoms are preferably adsorbed and hence contribute to the nucleus. This depends not only on the relative free energies of the electrode surface and the dissolved metal ions in the electrolyte, but also on the lattice mismatch between the deposited material and the electrode, the deposition rate and the temperature.[173,174]

If the adhesion between deposited material and substrate is strong and similar to the adhesion between individual atoms of the metal, and there is a low lattice mismatch, the material will grow in layers which ideally cover the whole substrate surface before a new layer is started. This growth is called Frank-van der Merwe growth (Fig. 3-3a). Strain due to a lattice mismatch adds up with increasing number of layers. Above a critical value, the strain will be relieved as the

material starts to form 3D crystal islands instead of forming another layer, this growth is then called Stranski-Krastanov growth (Fig. 3-3b). A low surface free energy of the substrate leads to a lower adhesion between substrate and deposit. Hence, once a nucleation site on the substrate is occupied, it is energetically more favourable to increase the size of this nucleus than occupying a new site. This mechanism is called Volmer-Weber growth (Fig. 3-3c).[167] This mechanism is obviously the most interesting growth mode for electrodeposition of single 3D structures. As substrates with low surface free energy highly oriented pyrolytic graphite (HOPG) or boron doped diamond (BDD) are ideal materials. Additionally, both materials are chemically inert and can easily be prepared. The surface of HOPG is atomically flat in large parts of the surface with numerous step edges between the flat terraces. The BDD surface consist of randomly oriented grain surfaces and grain boundaries.

The crystals nucleate on the electrode in a semi-random manner. Fig. 3-4a shows three possible sites on a non-atomically flat surface. The different sites vary by the number of neighbouring atoms in the lattice. The site labelled (α) has three neighbouring atoms, while (β) has two and in (γ) only one side of the nucleus will be in contact with the electrode. On HOPG, crystals grow prevalently along step edges, as terraces are almost electrochemically inert.[175] These step edges form every time in a random manner when the HOPG is prepared. In Fig. 3-4b tin crystals on HOPG are shown where two large step edges are visible. In contrast to HOPG, where step edges are the preferred nucleation sites, on BDD the density and occurrence of nucleation sites depends on the orientation of the individual crystalline grains and their surfaces. Fig. 3-4c shows densely grown tin crystals on a BDD surface, illustrating the effect of different grain orientations and grain boundaries.

Crystal growth

Once a stable nucleus has been created, its growth depends mainly on the mass transport from solution to the nucleus and the surface reaction in which the integration of the atoms into the nucleus are controlled. Three main mechanisms control the mass flow to the nucleus; diffusion, convection and migration.[176] Con-

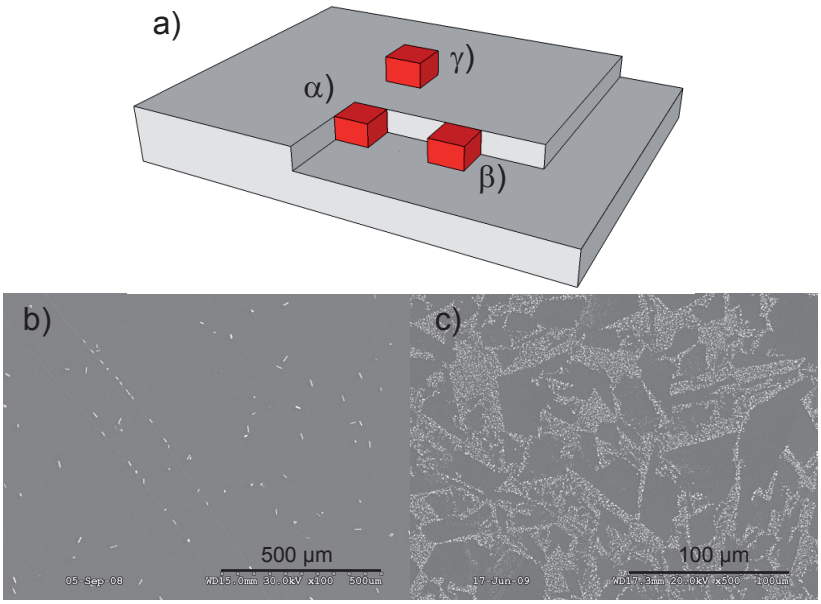

Figure 3-4: (a) Sketch of the available sites for nuclei to form on a crystal surface. (b): Nucleation along step edges on HOPG and (c) on particular grains on BDD.

vective mass transport is unimportant for crystals smaller than 10 µm and small applied potentials.[171,176] Migration can be suppressed by adding a high concentration of charged molecules to the electrolyte, which masks the charge build-up due to the ion separation.[176]. The main process responsible for the mass transport is diffusion of the ions, hence the process is said to be diffusion controlled.

The nucleus draws the ions from a semi spherical diffusion zone around it. The dimensions of the nucleation zone are controlled by the applied potential, the concentration of ions and the time from the moment when the potential was applied. As the diffusion zones grow, the diffusion zones of two crystals in proximity will overlap (*cf.* Fig. 3-5). The initial 3D semi spherical diffusion for an isolated crystal will be confined by the merging diffusion zones. In the limit of very long times, the diffusion changes from 3D semi spherical to 1D linear diffusion (Fig. 3-5a). Scharifker and Hills analysed this behaviour in detail.[177] Nucleation and growth happens in two different ways. For instantaneous nucleation, all nuclei form at the same time and from that time, the diffusion zones grow. All crystals have the same "age" (Fig. 3-5b, top). If new crystals are formed at all times during the crystal growth, the nucleation is called progressive nucleation (Fig. 3-5b,

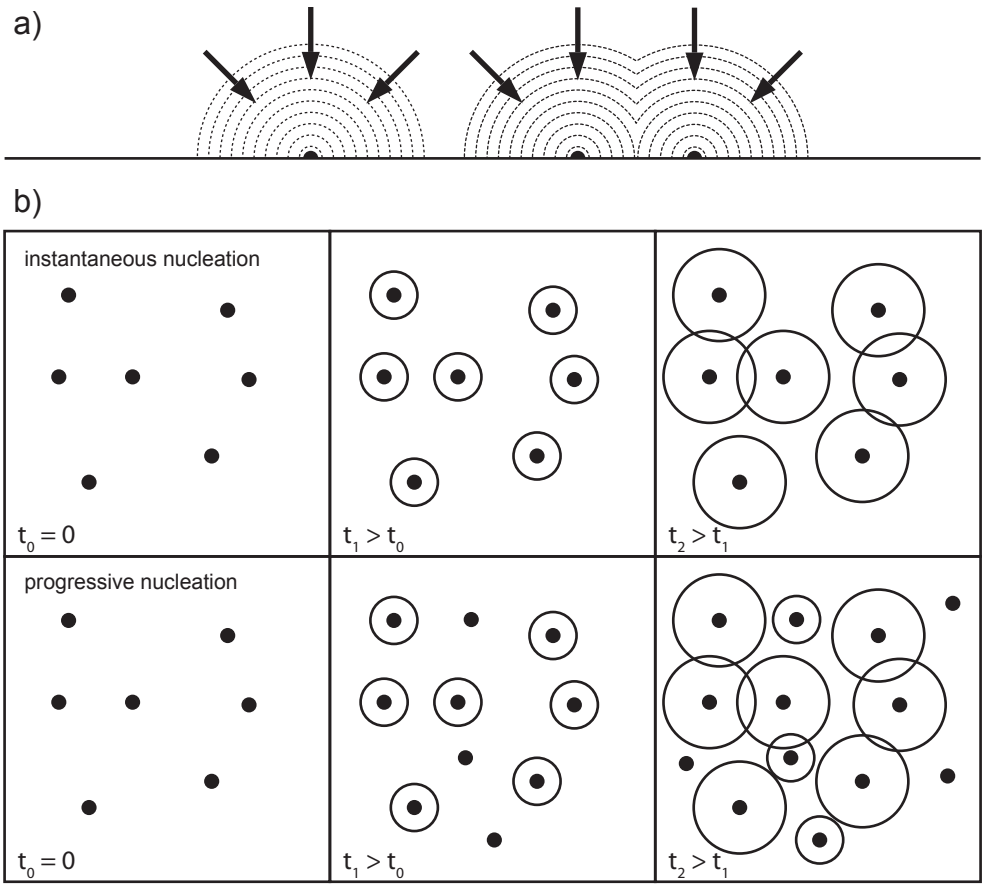

Figure 3-5: A sketch showing the growth and merging of diffusion zones for neighbouring crystals. The side view (a) illustrates the crossover from 3D spherical diffusion to 1D linear diffusion. The top view shows the difference between instantaneous and progressive nucleation for three different times $t_0 < t_1 < t_2$ after initial nucleation took place (b).

bottom). The distribution of crystal dimensions is obviously more homogeneous for the instantaneous nucleation than for the progressive nucleation. The way in which the crystals nucleate governs the way in which the overall current changes and hence can be investigated via the current/voltage transient. The method is named after its proposers Scharifker and Hills and uses the number of nuclei for progressive nucleation at a given time t which is

$$N = N_0 \left(1 - e^{-At}\right), \tag{3.3}$$

depending on the saturation nucleus density (number of active sites on the elec-

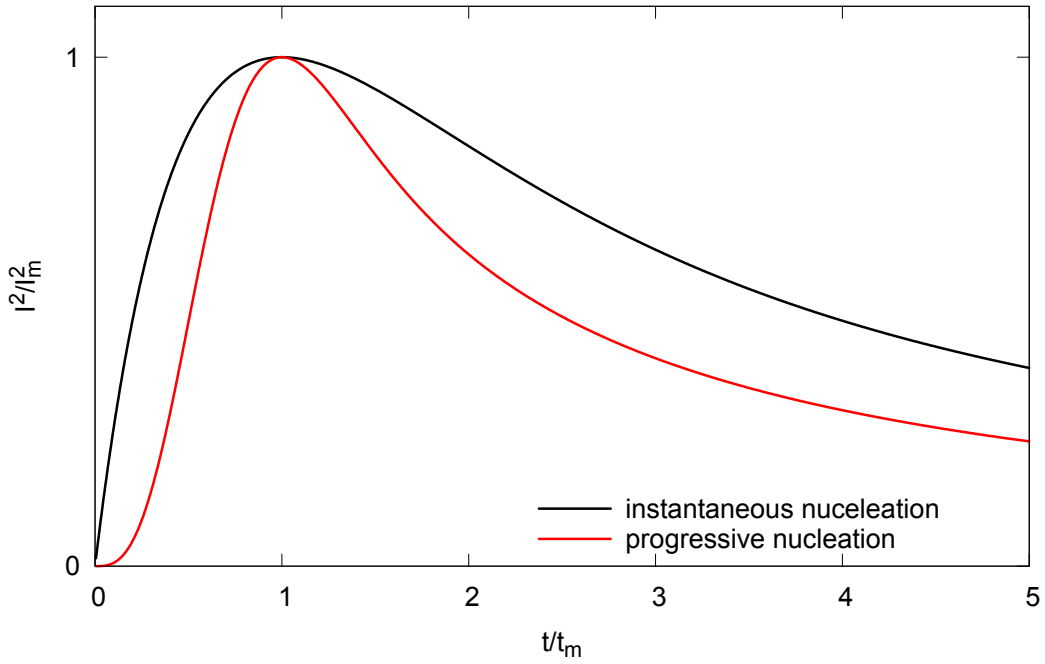

Figure 3-6: The $\frac{I^2}{I_m^2}(t/t_m)$ functions for instantaneous and progressive nucleation as described by Scharifker and Hills.[177]

trode) N_0 and the nucleation rate constant A.[178] For instantaneous nucleation, it is clear that $N = N_0 \neq N(t)$. Due to conservation of mass, the total mass incorporated in the crystals can be identified by the integrated current over the time of the crystal growth

$$\int_0^t I(u) \left(\frac{\mathrm{d}N(t)}{\mathrm{d}t}\right)_{t=(t-u)} \mathrm{d}u. \tag{3.4}$$

This was solved numerically by Scharifker and Hills (S-H) for the two cases of instantaneous nucleation ($N = N_0 \neq N(t)$) and progressive nucleation ($N = N(t)$). The result is expressed in the form of normalised currents and times where $I_m(t_m)$ represents the maximum current I_m and the time t_m at which the

maximum current occurs:

$$\left(\frac{I^2}{I_m^2}\right)_{\text{inst}} = \frac{1.9542}{t/t_m}\left(1-e^{-1.2564(t/t_m)}\right)^2 \tag{3.5}$$

$$\left(\frac{I^2}{I_m^2}\right)_{\text{prog}} = \frac{1.2254}{t/t_m}\left(1-e^{-2.3367(t/t_m)^2}\right)^2. \tag{3.6}$$

These functions are shown in Fig. 3-6. Although the Scharifker Hills nucleation model gives a good estimation of the nucleation process from the $I(t)$ characteristic, it oversimplifies the actual nucleation process. Without knowledge of further parameters, such as optical images of the actual nuclei, it is not suitable to unambiguously evaluate the nucleation process.

3.2 Experimental set-up

Fig. 3-7a shows a sketch of the electrochemical set-up. A polytetrafluoroethylene (PTFE) container was used as electrochemical cell which holds the electrolyte. PTFE was chosen because of its chemical inertness. Usually about 50 mL of electrolyte were used in the cell. 10 mm diameter PTFE disks were used to hold the working electrode (WE), which was either a 3 mm $\times$ 3 mm boron-doped diamond (BDD) (Windsor Scientific, Berkshire, U.K.) with a boron content of about 0.1 %, or a 5 mm $\times$ 5 mm square piece of highly ordered pyrolytic graphite (HOPG). For the BDD, the PTFE disk was fitted with a cavity to hold the diamond, which was then on exactly same level as the top of the disk. Electrical contact was established with a metal screw through the back of the disk, to which the BDD was glued with silver loaded epoxy. This mounting made it easy to polish the diamond, as its surface was levelled to the rest of the PTFE disk (Fig. 3-7b). The HOPG was glued to the top of the PTFE disk, which was fitted with a screw again to gain electrical contact. To allow only the surface of the BDD or HOPG to come into contact with the electrolyte a piece of Kapton tape with a 2.5 mm diameter hole was used to seal off everything but the central part of the electrode, Fig. 3-7c. A hole in the centre of the cell took the screw of the electrode. PTFE tape was used to make sure that the cell was sealed, and the electrode was connected to the potentiostat using a nut and a crocodile clip.

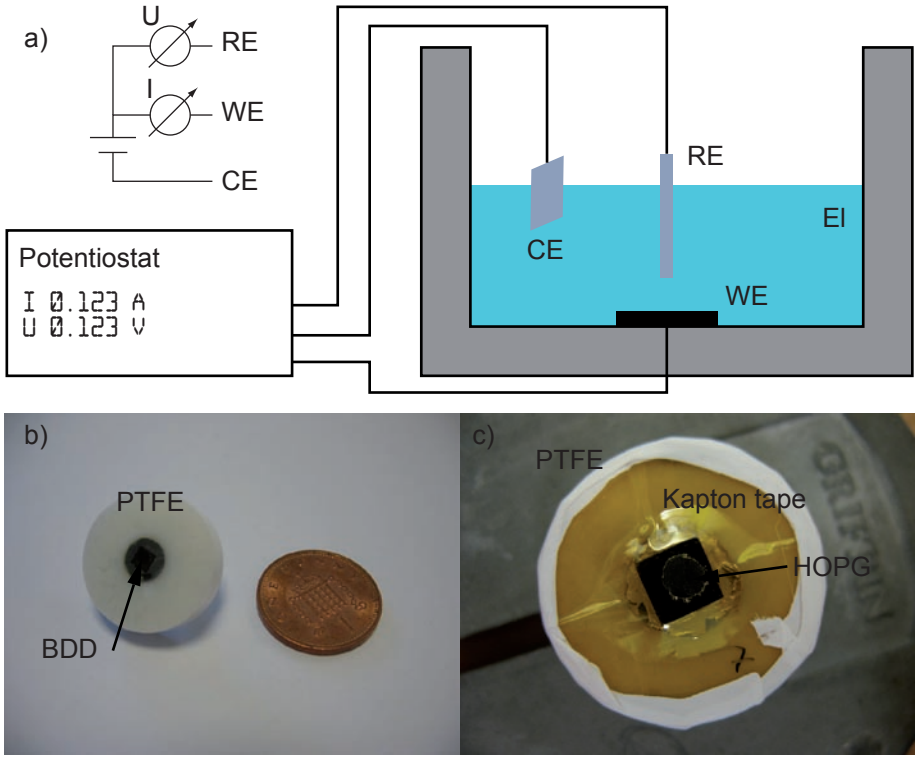

Figure 3-7: A sketch of the electrochemical set-up showing the electrochemical cell with electrolyte (El), working-, reference- and counter electrode (WE, RE and CE respectively) connected to the potentiostat. The inset shows a simple model of the potentiostat (a). (b) and (c) show a BDD and an HOPG working electrode respectively.

The BDD was polished using 3 µm and 1 µm alumina powder (Buhler) on a microcloth (Buehler, Lake Bluff, IL) and thoroughly rinsed in DI water to get a clean surface prior to each use. The HOPG was cleaved using a piece of scotch tape. Large flakes on the surface were carefully removed with the corner of a piece of scotch tape. Contact between scotch tape and the surface of the electrode, which was used to plate, was avoided. If the surface was still uneven, the cleavage was repeated.

During the experiment the working electrode was horizontally flat when immersed in the electrolyte. Counter and reference electrodes (CE and RE) were attached to a lid which was placed on top of the cell during the experiment. As a counter electrode a piece of platinum (Pt) foil (Advent Research Materials Ltd., Oxford, U.K.) was used which was attached to the potentiostat using a crocodile clip. A silver/ silver chloride (Ag/AgCl) electrode was used as a reference electrode.

The reference electrode was freshly prepared before each set of experiments. A Ag wire (Advent Research Materials Ltd., Oxford, U.K.) was immersed in saturated NaCl solution and a potential of +2 V was applied for about 10 s, during which time the wire turned completely black. The same electrode was used as a reference electrode for all experiments in one series. Between experiments the wire was kept in the dark to avoid degradation.

The potentiostat was connected to a computer which allowed full control over the applied potential.

The electrolyte solutions were freshly prepared prior to each experiment from tin(II)tetrafluoroborate ($Sn(BF_4)_2$) or lead(II)tetrafluoroborate ($Pb(BF_4)_2$) solution, Fluoroboric acid solution (HBF_4) (all Sigma-Aldrich, U.K.) and Milli-Q water (Millipore, resistivity of 18.2 $M\Omega \cdot cm^{-1}$). All solutions were de-aerated with argon before use.

3.3 Crystal growth

The following section explains the experimental methods used to grow the crystals for this work with the equipment described above (*cf.* also Appendix A).[179] Prior to starting the growth process a potential of +1 V was applied for 30 s to strip off any impurities on the electrode and give it a final clean. The potential was reduced to 0 V for another 30 s to let the solution and the potentiostat settle, after which a constant overpotential was applied for a predefined timespan or until a certain charge was transfered and the required material deposited. After deposition the working electrode was removed from the electrolyte and carefully rinsed with DI water. The DI water was then blown off with a stream of argon, the deposit examined under an optical microscope and imaged with a scanning electron microscope (SEM) (S-4300 Scanning Electron Microscope, Hitachi) or an atomic force microscope (AFM) (MFP-3D, Asylum Research).

3.3.1 Pure tin crystals

One of the main goals of this work was to establish a method to electrodeposit 3D tin crystals for further analysis. Previous works had focused on the deposition of thin films[180] as well as dendritic growth[181,182] and the growth of nanostructures.[183–186] Gómez *et al.*[187] investigated the nucleation and electrochemical growth of microcrystallites with relatively poorly faceted habits.

The techniques used in these experiments were refined to electrocrystallise samples with a better surface quality and a better controllability of their dimensions. The shapes, which can be grown from tetrafluoroboric Sn(II) solutions, range from square cuboids to complex dendritic shapes as Sn(II) concentration and growth potential are increased. All solutions used in these experiments had a concentration of 1 M BF_4^- and a Sn(II) concentration between 10 mM and 100 mM.

Fig. 3-8a shows a typical cyclic voltammogram (CV) for a tin concentration of 25 mM and 1 M BF_4^-. The CVs for other concentrations are qualitatively identical. The only differences in the CVs for different tin concentrations are that the curve is shifted on the potential axis and the charge transfer is larger for higher Sn(II) concentrations. The CV was recorded from $-1\ \text{V} \leq U \leq 1\ \text{V}$, but for $U > -0.4\ \text{V}$ no current flowed and this part is not shown in the graph. A negative current in the CV means that the Sn(II) ions are reduced and hence material is deposited. A positive current indicates the oxidation and stripping of ions of the material from the electrode surface. Deposition starts where the current suddenly decreases to a negative value. For the CV in Fig. 3-8a this happens at -710 mV. A reduction peak is visible at -890 mV. An oxidation peak is visible for increasing voltages at -515 mV. For the deposition, a constant voltage is applied and the current is recorded. Three depositions from the 25 mM Sn(II) solution at three different potentials are shown in Fig. 3-8b. The curves at -720 mV (black), -760 mV (red) and -780 mV (green) illustrate the two main regimes which were used to grow the crystals. The lowest overpotential leads to a continuously rising current and hence slow nucleation and growth of the crystals, for such low potentials, the diffusion of material occurs faster than the incorporation of new material in the crystal, and this growth is kinetically limited.[188] The bottom

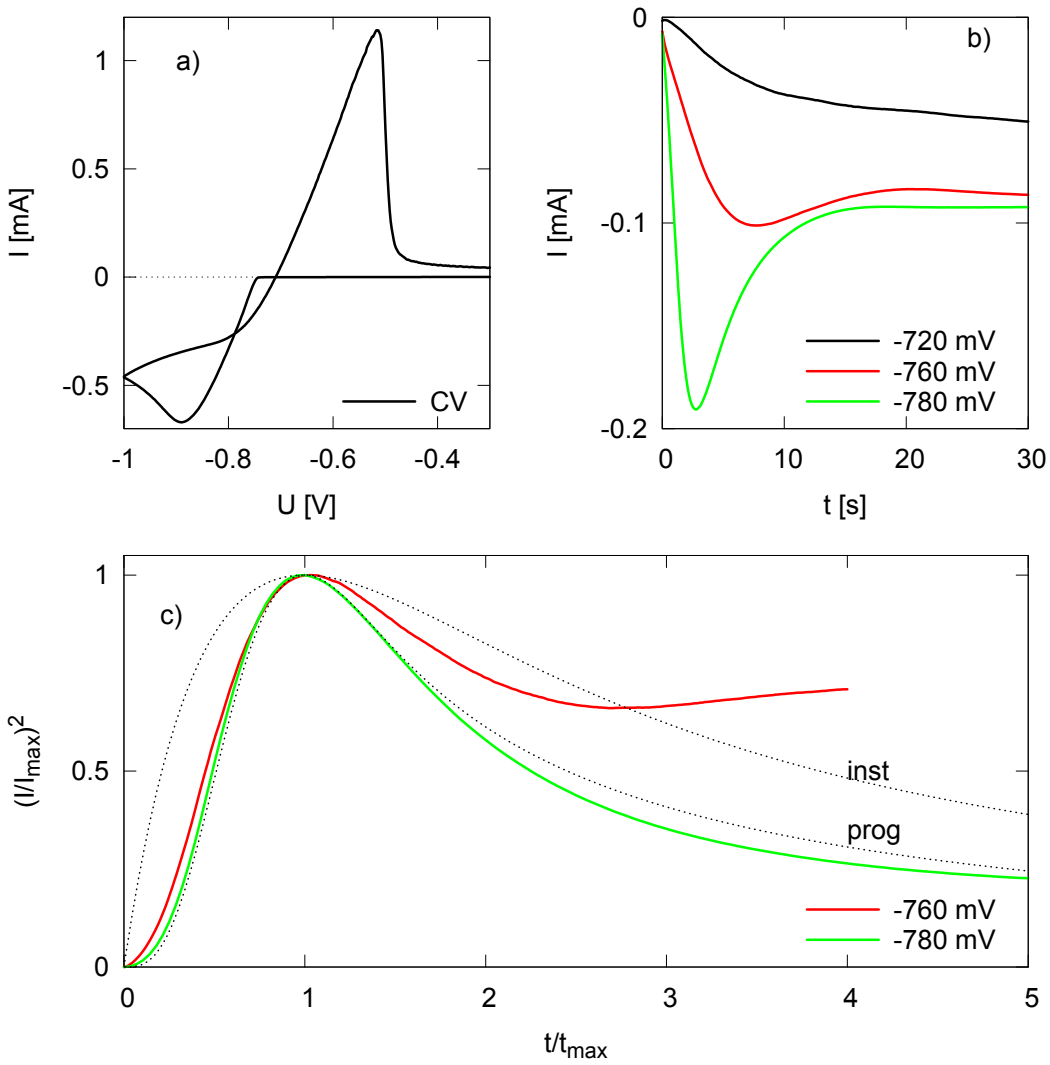

Figure 3-8: (a) Typical cyclic voltammogram for 25 mM Sn(II) solution with respect to the Ag/AgCl reference electrode. Scan rate: 50 mVs^{-1}. The deposition of tin starts at -710 mV. A reduction peak is visible at -890 mV and an oxidation peak at -515 mV. (b) *I-t* curve for three different potentials (-720 mV, black; -760 mV, red and -780 mV, green) in 25 mM Sn(II) solution. (c) $I_r^2\,(t_r)$ curve for two measurements with a clear maximum $I_m\,(t_m)$. The model of instantaneous (inst) and progressive (prog) nucleation after Scharifker and Hills[177] are shown as dotted lines.[179]

curve in Fig. 3-8b is at the highest overpotential of -780 mV and shows a rapidly increasing current for the first 2.8 s and a decrease thereafter (diffusion limited growth). The curve in the middle at -760 mV shows some intermediate behaviour. The *I-t* characteristics of the curves shown demonstrate that at low overpotentials

a small number of simple shaped, faceted crystals such as cuboids, which have a low surface energy, form. Higher overpotentials lead to a higher density of crystals and much more complex shapes can form. Complex snow flake like crystals or dendrites with high surface energies form at high overpotentials. The nucleation in the diffusive regime occurs as progressive nucleation according to the model by Scharifker and Hills.[177] In Fig. 3-8c the two high potential curves from Fig. 3-8b are plotted in the form $\frac{I^2}{I_m^2}\left(\frac{t}{t_m}\right)$ (*cf.* Sec. 3.1.1 and Fig. 3-6). Both curves fit very well to the model of progressive growth, especially for times shorter than t_{max}. The lower overpotential, however, deviates from the numerical model for long times, indicating that the process in this case is not fully diffusion controlled as described in the Scharifker and Hills model, and that the process has a significant kinetic component.[189]

The growth of tin crystals from $Sn(BF_4)_2$ follows the Volmer-Weber mechanism as it is more favourable for the tin atoms to bind to an existing nucleus than to start growing a new nucleus. The number of active sites depends strongly on the material used for the working electrode. The number of crystals on BDD is typically higher than on HOPG, but the general size and shape distribution is similar on the two substrates. The growth mechanism of tin dendrites from $SnCl_2$ in HCl was extensively investigated and described by Wranglén.[181] This work can be used and adopted to understand the growth and crystal orientation of the microcrystals prepared in this work. The dimensions of the crystals were accurately measured using SEM and AFM images as well as using an optical microscope, where a micromanipulator was used to move and turn the crystals while observing them, which allowed a full 3D view of individual crystals.

Tin crystallises in two different configurations at room temperature, but only β-tin is able to form large faceted crystals. β-tin crystallises in a body-centred tetragonal lattice with a two atom basis and $a = b = 5.82$ Å and $c = 3.17$ Å. The second atom of the two atom basis is at $\frac{1}{2}a$ and $\frac{1}{4}c$. Wranglén observed that dendrites grow along the [110] direction and are formed from single pyramids whose tips point in the [001] direction. Simple geometrical considerations show that the theoretical angle between the (001) base plane of the pyramid and the side of the pyramid (101) is 28.6°. Although these pyramidal dendrites were not observed in this work, the same geometrical considerations explain the observed shapes of

crystals. Due to the very low cohesion energy of tin[187] and the low overpotentials used, the atoms were given plenty of time to rearrange on the crystal, forming the energetically most favourable shape. The evolution of crystal habits as a function of Sn(II) ion concentration and applied overpotential is shown in Fig. 3-9. Generally, an increase of complexity is visible with increasing Sn(II) concentration and overpotential. The first row of images shows crystals that were grown from 10 mM Sn(II). Fig. 3-9(a and b) show relatively large square cuboid rods, while the crystal in (a) seems to be hollow. For higher potentials, (c - f), the crystals look like the outer skeleton of a square cuboid with defects along the middle and in the centre. The crystals grown from a 25 mM solution are larger for the same growth time, but still show a general cuboid shape. Low overpotentials, (g - i), lead to ordered square cuboid crystals, while higher overpotentials and longer growth times, (j - l), yield mostly hollow skeletons with an exterior cuboid shape. The two bottom rows show crystals from the highest investigated concentrations. Low overpotentials still lead to rather complete, solid square cuboids (m) while higher overpotentials lead to very complex, dendritic crystals, (o - r and t - x). There are, however, still cuboid structures visible in the crystals. For example in Fig. 3-9(u and w) the crystal 'scaffold' looks like a number of cuboids held together by an outer skeleton. The pyramid angle described above can be seen in many of our crystals *e.g.* in Fig. 3-9(c, e, h and k). Here the end of the cuboid is cut at exactly this angle (*cf.*, Fig. 3-10b), while for Fig. 3-9(h and n) the end is cut at an angle of about 30° (*cf.*, Fig. 3-10c). For the crystals in Fig. 3-9(c, e and k) the cavity is symmetric around the centre of the crystals, suggesting that a twin plane runs through the crystal. These observations indicate that the long axis of the cuboids corresponds to the [001] direction, while the two (equal) short lengths are along the two equivalent directions [100] and [010] (*cf.* Fig. 3-10a), consistent with the conclusions of Gómez *et al.*.[187] This is the shape expected for a slow kinetically-limited growth when the energetically-favoured high atomic density surfaces are selected.

For higher concentrations and overpotentials the growth mechanism changes. The fastest growth seems to happen along the body diagonal [111] direction (*e.g.* Fig. 3-9(o and p)) while the faces of the cuboid are only partially developed. For the highest concentration (Fig. 3-9 bottom row) the crystals grow in a dendritic,

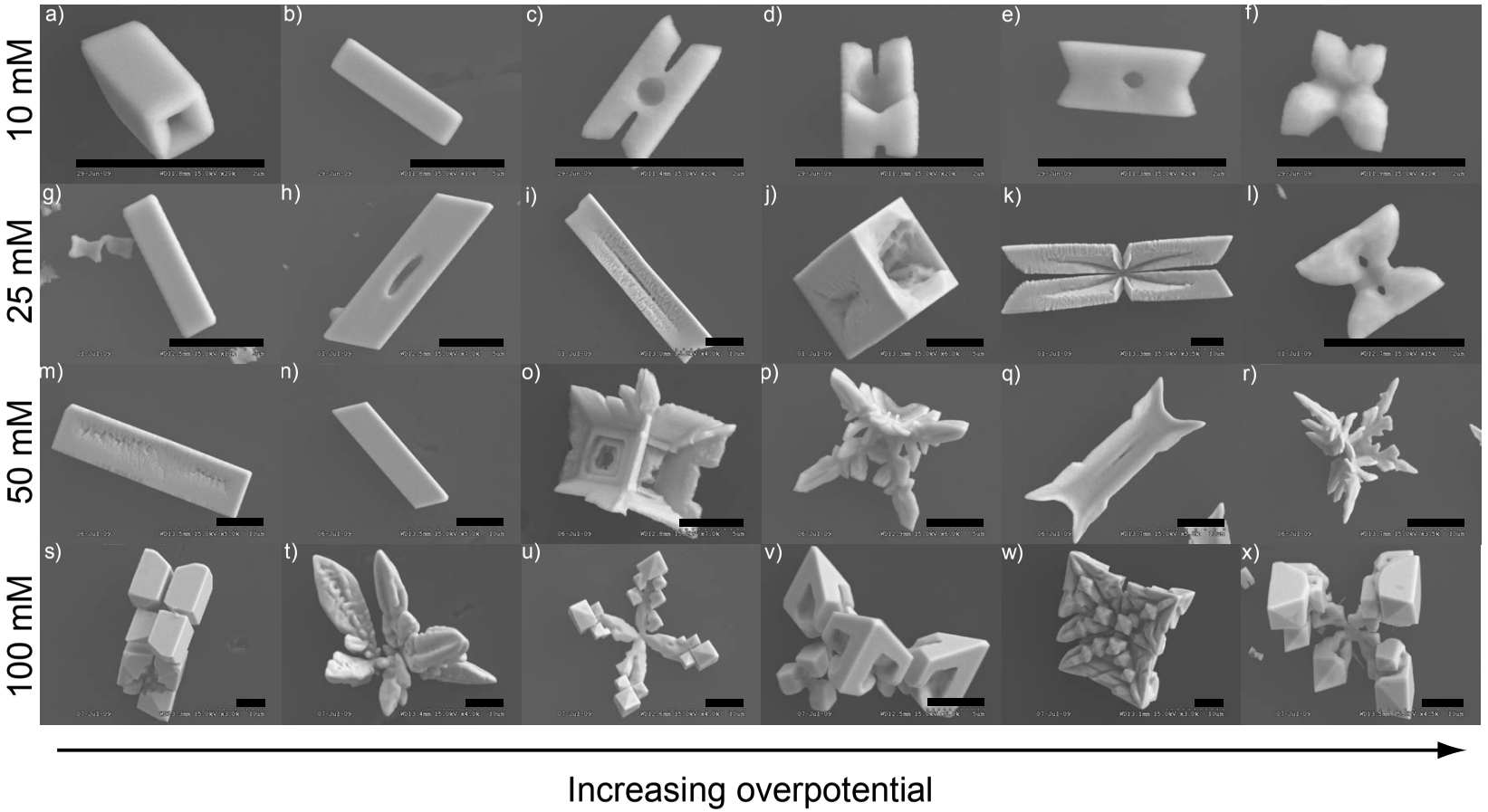

Figure 3-9: Electron micrographs of crystals grown under different conditions. Row one: 10 mM, a) and b) 30 s at -740 mV, c), d) and e) 30 s at -760 mV, f) 30 s at -900 mV. Row two: 25 mM, g) and h) 30 s at -720 mV, i) 30 s at -730 mV, j) and k) 90 s at -730 mV and l) 30 s at -780 mV. Row three: 50 mM, m) and n) 30 s at -720 mV, o) and p) 30 s at -760 mV, q) and r) 30 s at -800 mV. Row four: 100 mM, s) and t) 30 s at -800 mV, u) and v) 30 s at -820 mV, w) 30 s at -860 mV and x) 30 s at -900 mV. The scale bar is 5 µm in all cases.[179]

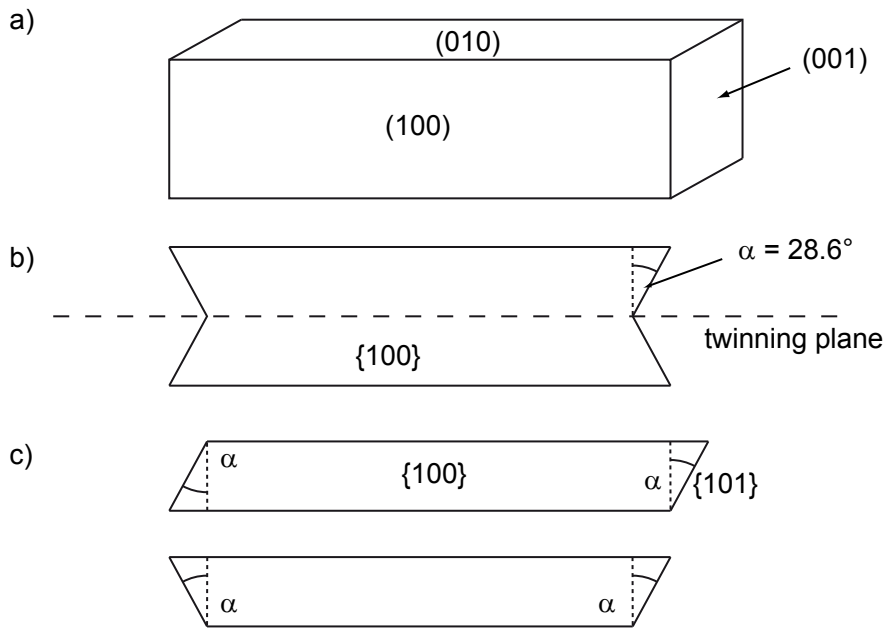

Figure 3-10: The crystallographic orientation of some of the structures observed. a) the general growth planes and directions, b) symmetric growth about a twinning plane, c) asymmetric growth.[179]

fern-like manner. The crystals in Figs. 3-9(u and x) show, in particular, that the structures still grow as single crystals, albeit multiply-twinned ones. The main branches are of quite irregular shapes but at the end caps the cuboid parts are arranged along identical axes. Spherical diffusion layers are formed around more acute pointed parts of the crystal, resulting in more efficient 3D diffusion. This leads to faster growth at these locations and incident atoms have little time to diffuse on the surface, resulting in a highly non-equilibrium surface structure. This explains the formation of the skeletons, since the fastest growth occurs at the corners rather than the faces of the crystal. This is also the origin of the dendritic growth when, even further away from equilibrium, the crystal grows preferentially at the crystal corners rather than at edges or on faces.[182]

Despite the large variety of crystal shapes, the most interesting shape for the measurements in the work are simple cuboids, *e.g.* in Fig. 3-9b. Although the ideal crystal should have a square cross-section, this is not always true for real crystals. Many crystals had a slightly lower "height" than "width" when grown flat on the electrode.

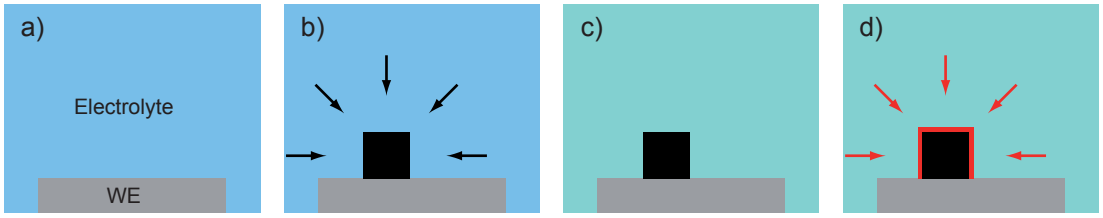

Figure 3-11: A sketch of electrocrystallisation and electroplating to form a core-shell structure. An electrolyte with the ions for the core is used to grow a crystal on the working electrode (WE) (a and b). After the growth process, the electrolyte is exchanged to another electrolyte (c) and the shell is plated on all but the bottom side of the existing crystals (d). Ideally no shell-material will be deposited on the electrode.

3.3.2 Core-shell crystals

Electrodeposition offers an easy way to plate a crystal of one material with another material whose overpotential for plating is higher than the one for the first material. This condition is true for the plating of Pb on Sn from fluoroboric acid solutions. The basic principle of growing a core and plating it with a shell is shown in Fig. 3-11. The core is grown from Sn(II) solution as described above (Sec. 3.3.1). After growth of the core, the electrolyte is replaced by another electrolyte. The solution for the lead shell was typically 10 mM Pb(II) and 1 M BF_4^-. The overpotential for lead is slightly higher than the overpotential for tin as shown in Fig. 3-12. For the HOPG working electrode used and the Ag/AgCl reference electrode, tin starts to deposit at an overpotential of -730 mV and lead at -760 mV. To plate the tin crystals with lead, but not reduce the tin from the already formed crystals, the potential for plating has to be larger than the potential for reducing tin. Good results were achieved for a plating potential slightly higher ($\approx$ 10 mV) than the potential for the tin growth. HOPG led to generally better results than BDD. On BDD a considerable amount of lead formed crystals on the electrode, while on HOPG almost no lead deposit was visible at the electrode surface. This is probably due to the much lower number of active nucleation sites on the HOPG compared to the BDD. After the plating the crystals had a rough look (*cf.* Fig. 3-13a - c), indicating that the lead film is polycrystalline on top of the tin. The shell covers all exposed surfaces of the tin crystal. Only one side, where the crystal is attached to the electrode, is not completely covered in lead. If the bottom of the crystal is not completely attached

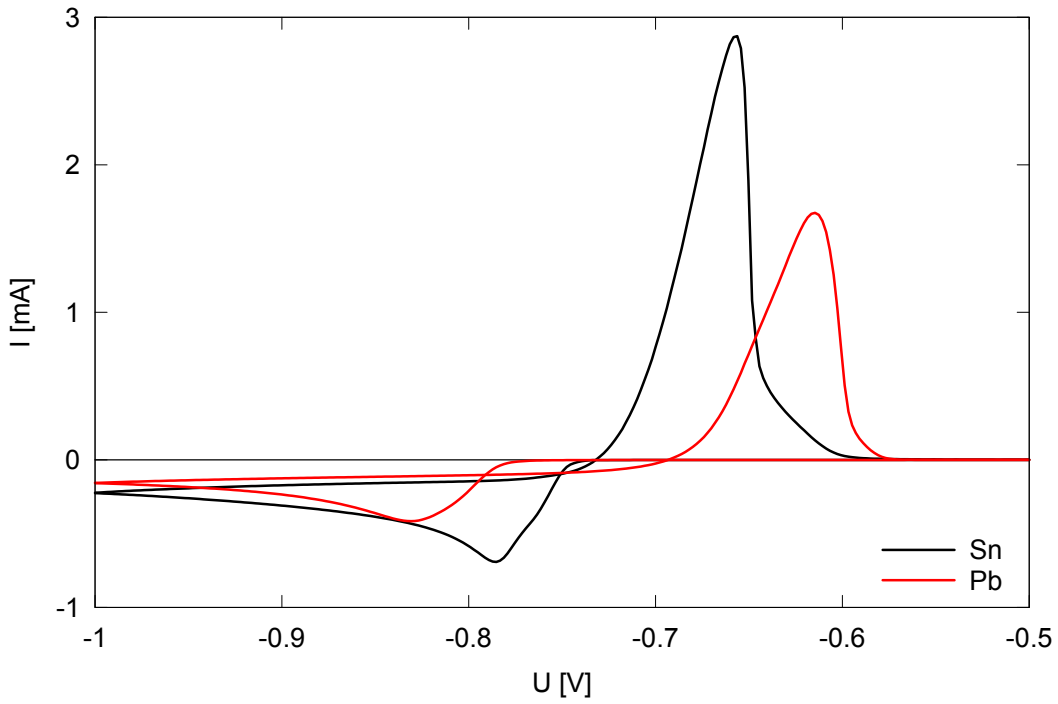

Figure 3-12: Cyclic voltammogram for 10 mM Sn and 10 mM Pb solutions on the same HOPG electrode. The electrode was freshly prepared before the measurements. The graph shows the last of six consecutive scans.

to the electrode, a partial coverage of the bottom is possible. The thickness of the shell was estimated by comparing the charges of the tin and lead deposition. The total charge $Q = \int I(t)\mathrm{d}t$ is a measure for the amount of material deposited and is directly proportional to the deposited mass $Q \propto M$. The dimensions of the core-shell structure are measured using an AFM scan and lead to the volume of the shell

$$\begin{aligned} V_{shell} &= V_{tot} - V_{core} \\ &= l \cdot w \cdot h - [(l - 2d) \cdot (w - 2d) \cdot (h - d)] \end{aligned} \tag{3.7}$$

using the length l, width w and height h of the crystal, as well as the unknown thickness of the shell d. Under the following assumptions, the thickness of the shell can be approximated:

(i) The shell is even on all five sides of the cuboid, which were exposed to the electrolyte during deposition.

(ii) The amount of material used to form one core and the amount of material to form the shell on that specific core are proportional to the total charge transmitted during the electrodeposition.

(iii) All deposited material counts towards the shell thickness.

Although these conditions are not perfectly met, this approach yields a reasonable value for the thickness d. The proportion of the volumes and the charge can be connected through the density ρ of the material and give

$$\frac{V_{shell}}{V_{core}} = \frac{m_{shell}}{m_{core}} \cdot \frac{\rho_{core}}{\rho_{shell}} = \frac{Q_{shell}}{Q_{core}} \cdot \frac{\rho_{core}}{\rho_{shell}} \tag{3.8}$$

which can be solved for d.

A much more precise measurement of the dimensions of the structure is possible with a focused ion beam (FIB), which can be used to slice and mill a portion of the crystal. Fig. 3-13d shows a sketch of the dual beam system. While the FIB is used to mill the crystal perpendicular to the electrode surface, the electron beam of the scanning electron microscope (SEM) is used to image the cross-section while the milling is in progress. The SEM looks at the cross-sectional interface at an angle of 52° due to the construction of the dual beam system. After milling to the desired depth, the intersection is imaged using the same SEM to record a high resolution image. Fig. 3-13a, b show two cross sections of two different core-shell structures which were measured at the dual beam FIB-SEM at the IAC in Bristol with the assistance of Dr. P. Heard. For the sample in Fig. 3-13a the charge ratio was exactly $\frac{Q_{shell}}{Q_{core}} = \frac{1}{2}$ and the result of Eq. (3.8) gives a shell thickness of $d \approx 200$ nm with $\rho_{\mathrm{Pb}} = 11.34$ g/cm^3, $\rho_{\mathrm{Sn}} = 5.769$ g/cm^3 ([190]) and the dimensions $l = 6$ µm, $w = 4$ µm and $h = 4$ µm, while the shell thickness measured from the image is $d \approx 120 - 220$ nm depending on the position of the measurement. These values are in good agreement which shows that, although strict assumptions apply, the result of Eq. (3.8) gives a good estimation for the shell thickness. Fig. 3-13b shows the cross section of a tilted grown rod. As illustrated in this image, the lead plates also on the lower surfaces of the rod. Only where the rod touches the electrode no lead film is visible.

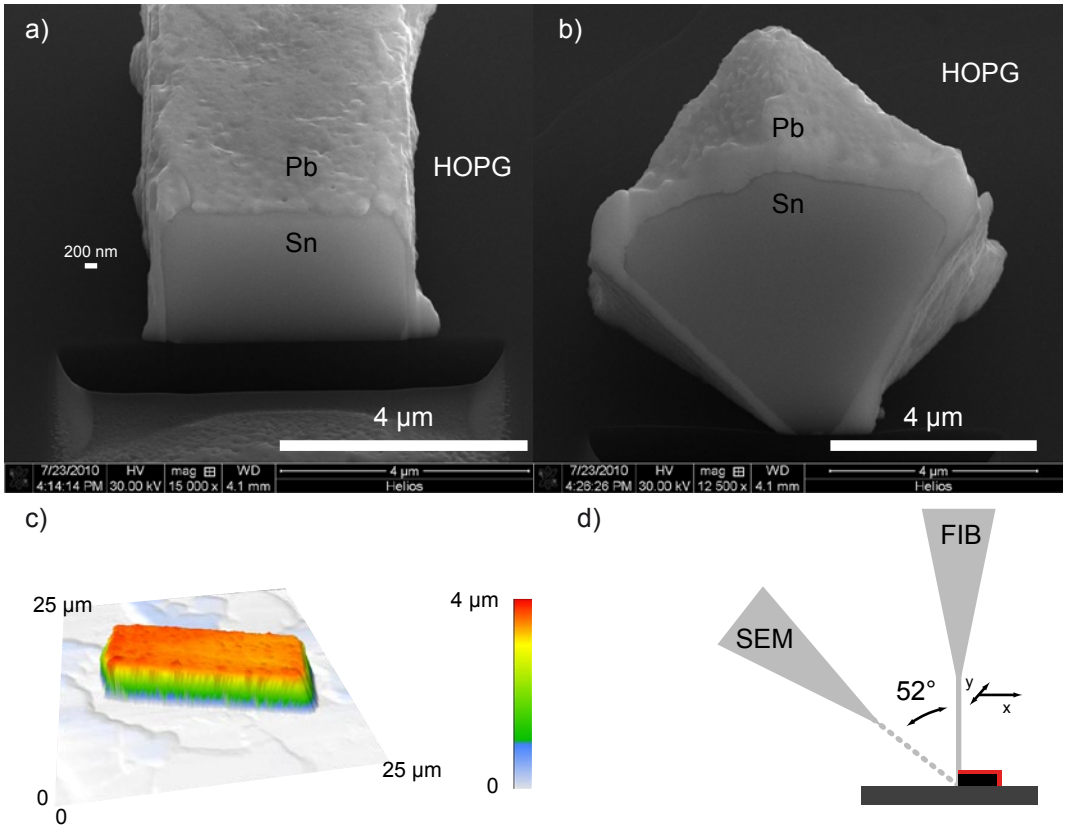

Figure 3-13: Two FIB milled cross-sections of Sn-Pb core-shell structures (a and b) and an AFM scan of a cuboid Sn-Pb core shell structure (c). The geometry of the dual beam FIB used to mill and image the crystals is shown in the sketch in (d).

Attempts were made to examine the Pb-Sn interface using energy-dispersive X-ray spectroscopy (EDX) at the centre for electron optical studies (CEOS) at the University of Bath, but the spatial resolution of the system was not high enough to resolve details at the interface. The typical resolution of the system used is $\approx$ 1 µm and as the X-rays are emitted from as deep as 1 µm inside of the sample, no quantitative conclusion could be made. Nevertheless, careful analysis of the images in Fig. 3-13a, b does suggest that no alloying occurs at the interface between the tin core and the lead shell.

The preparation of core-shell structures is not limited to the growth of Sn-Pb core-shell structures. Pb-Ni and Sn-Ni superconducting-ferromagnetic core-shell structures were prepared in a similar way by Sara E. C. Dale.[136] Results for these crystals are shown in Sec. 7.

Chapter 4

Hall magnetometry

4.1 Introduction

The Hall effect, which is utilised in a magnetic probe in this work, was discovered in 1879 by Edwin Herbert Hall at the Johns Hopkins University in Baltimore while working on his doctoral thesis.[191] He found that, when exposed to a magnetic field, the force acting on the charge carriers in a metal strip, which are in motion due to a current flow through the metal, generates a voltage difference between opposite sides of the metal.

Fig. 4-1a describes the Hall effect schematically. A current $\vec{I}$ is flowing through a metal strip of thickness d. The current results in the electrons flowing in the opposite direction with the drift velocity $\vec{v}_d$. An applied magnetic field $\vec{B}$ perpendicular to the plane of the sample results in the Lorentz force $\vec{F}_L$ which drives the electron towards one side of the sample. If a hole is considered, this force will point in the opposite direction and hence leads to a separation of the charge carriers. The accumulation of negative charge on one side and positive on the opposite side of the sample generates an electrical field $\vec{E}_H$ and associated force $\vec{F}_H$ on the electrons which opposes the Lorentz force. In equilibrium, these two forces are balanced and a constant Hall voltage U_H builds up between opposite sides of the channel. With $\vec{B}$ and $\vec{I}$ perpendicular to each other as shown in the

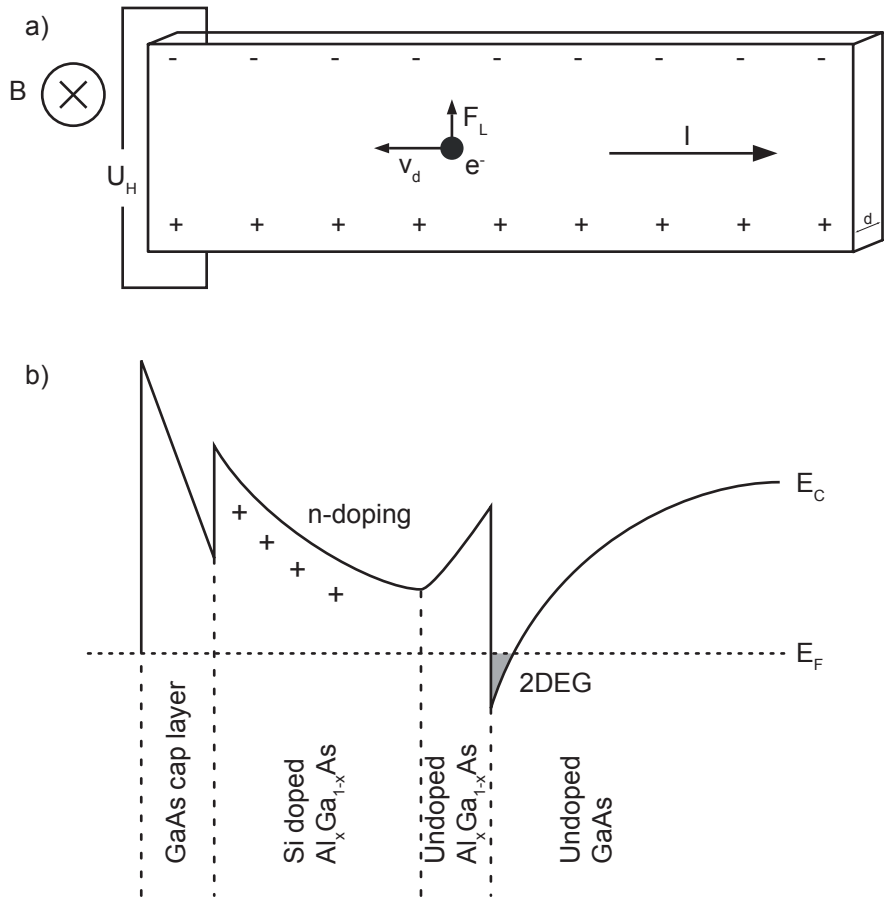

Figure 4-1: a) The Hall effect for electrons (e^-) moving with the drift velocity $\vec{v}_d$ due to a current $\vec{I}$ in a magnetic field $\vec{B}$. The Lorentz force $\vec{F}_L$ on the electrons results in the Hall voltage U_H. b) Sketch of the band structure of a 2DEG Hall probe as used in this work.[192,193]

sketch in Fig. 4-1a, the Hall voltage is expressed by

$$U_H = R_H \cdot |I| \cdot |B| \,. \tag{4.1}$$

The Hall coefficient in general is $R_H = (n \cdot e \cdot d)^{-1}$, with the charge carrier concentration n, the electron charge e and the sample thickness d, and depends on the material and the sample dimensions.

The use of a two dimensional electron gas (2DEG) in the material enhances the Hall effect at low temperatures and gives a better signal-to-noise ratio (SNR) for measurements with small Hall probes and at low temperatures as will be

explained in the following chapter. Most state-of-the-art systems currently use semiconductor heterostructure GaAs/AlGaAs Hall probes.[192,194,195]

To form a 2DEG, two materials with different band gaps are used to form a heterojunction. The lattice constants for GaAs and AlAs are very similar, especially for GaAs and $Al_{0.3}Ga_{0.7}As$ where they are almost identical, while the band gap is different, this makes the latter two materials ideal candidates to form such a heterojunction.[192] The difference in the two band gaps and the screening of the charge carriers due to the different position of the Fermi enegry E_F leads to a V-shaped potential well at the interface, where the conduction band E_C dips below the Fermi energy in a spatially confined layer. The thickness of this narrow layer is of the order of 10 nm. The band structure for a 2DEG in a GaAs/AlGaAs device as used in this work is shown in Fig. 4-1b.

For a 2DEG, the Hall coefficient becomes $R_H = (n_{2D} \cdot e)^{-1}$ in terms of the 2D charge carrier concentration n_{2D}, which results from the dimensional confinement of the states. As a 2D system is considered, the Hall coefficient becomes independent of the thickness d of the flow channel, as this dimension is no longer available for the electron movement.

Semiconductor Hall probes are the best choice for the fabrication of very sensitive Hall probes. As can easily be seen from Eq. (4.1), a low charge carrier concentration results in a large Hall coefficient R_H and hence in high sensitivity to an applied magnetic field. To increase the second parameter in Eq. (4.1), I, the conductivity of the systems needs to be as high as possible at low temperatures. This is achieved by the spatial separation of the doped layer and the 2DEG.[196] The electrons, caught in the 2DEG, are separated from their donor impurities by an undoped layer of AlGaAs, which virtually eliminates ionised impurity scattering, the main mechanism that limits the low temperature conductivity of bulk doped semiconductors.

To estimate the quality of a Hall probe the signal to noise ratio (SNR) is usually used. The SNR of Hall probes, as mentioned above, is usually limited by Johnson noise.[197–200] The root mean square (r.m.s.) voltage U_{JN} for a bandwidth $\Delta\nu$ is

given by[197]

$$U_{JN}^2 = 4k_B T R_C \Delta\nu. \tag{4.2}$$

k_B is the Boltzman constant, T the temperature of the system and R_C the resistance of the current channel. The ratio between the signal U_H and the noise U_{JN} is the SNR $= U_H/U_{JN}$. The SNR of our Hall probe is, where μ is the carrier mobility,

$$\text{SNR} \propto \sqrt{\frac{\mu}{n_{2\text{D}}}} \cdot I \tag{4.3}$$

which shows that materials with a high mobility μ and a low charge carrier concentration $n_{2\text{D}}$ are ideal for applications as Hall probes. Both criteria are met in a GaAs/$Al_{0.3}Ga_{0.7}$As 2DEG Hall probe. ($n_{2\text{D}} = 2.7 \times 10^{11}$ cm^{-2} and $\mu = 30\ m^2/Vs$ at $T = 4$ K in the dark.[199])

Microfabricated GaAs/$Al_{0.3}Ga_{0.7}$As Hall probes are ideal devices to probe magnetisation at low temperatures. In addition to the excellent SNR and the low detectable fields, the electrons move ballistically inside the Hall cross at low temperatures. This is due to the large mean free path of the electrons at low temperatures, which is of the order of or larger than the Hall cross. While in the diffusive regime, the magnetisation measured by the Hall cross is rather complicated to determine as a much larger area, including parts of the leads, has to be taken into account, in the ballistic regime the Hall voltage is mainly connected with the average magnetic induction across the junction $\langle B \rangle$ by a simple, linear relationship,[201,202]

$$U_H \propto R_H = \frac{\alpha \langle B \rangle}{n_{2\text{D}} e} \tag{4.4}$$

where α is a coefficient accounting for the collimation of the electrons. The collimation of the electrons becomes more complex with increasingly rounded corners of the Hall probe (*cf.* Fig. 4-2, increasing r).[203,204] Qualitatively this effect can be described by the trajectory of an electron through the Hall cross. The Hall effect is quenched if the electrons pass the channel in an almost straight line (T_1) so that no potential is generated between the two leads, or if the electrons are moved along a cyclotron orbit smaller than the width of the channel (T_3). T_2 shows the ideal path for the electron to follow in order to maximise the Hall coefficient and hence maximise the sensitivity of the Hall probe. Extremely rounded

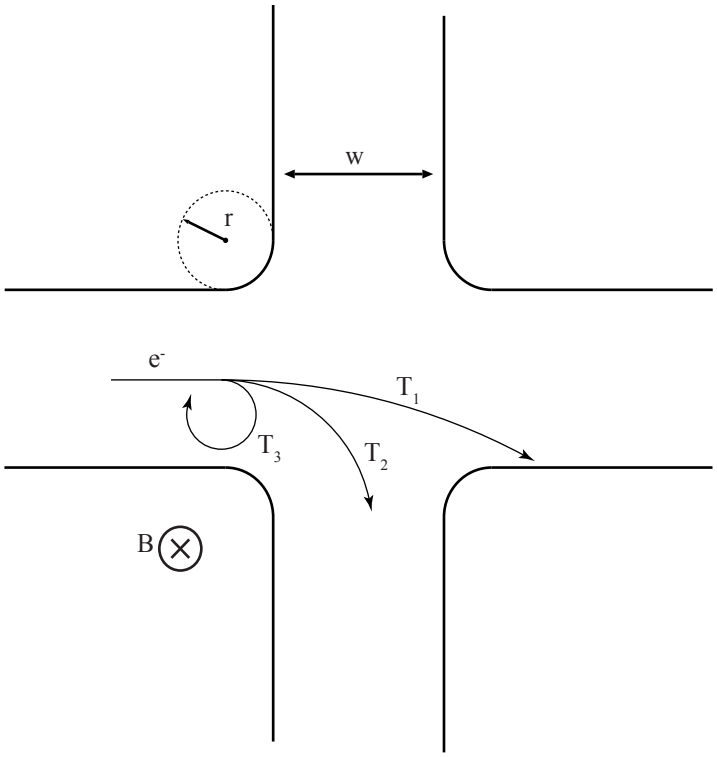

Figure 4-2: Sketch of a Hall cross with rounded corners (with radius r), width w and three different trajectories (T_1, T_2 and T_3) for an electron.

corners as shown in Fig. 4-2 lead to "guiding-center drift" which basically guides the electrons around the corner, leading to the enhancement of the resistance up to the value of the contact resistance of the lead, which is practically independent of the magnetic field.[205] It has been shown that slightly rounded corners of the Hall probe do not affect the magnetisation measurements dramatically.[206] While a perfect, square cornered, Hall cross responds linearly to the magnetisation through the central square w^2, for a Hall cross with rounded corners of radius r the field within an area of $(w + 1.4r)^2$ has to be taken into account and the relation is approximately linear within an error of about 2 % (*cf.* Figure 3 in ref.[206]). The average magnetic field is $\langle B \rangle \propto \int B \, \mathrm{d}x \, \mathrm{d}y$, *i.e.* the measured Hall voltage is proportional to the flux through the area of the sensor. Therefore, these Hall sensors can be considered as micro fluxmeters, comparable to a SQUID with a very small detection loop. Knowing the external applied field H by measuring it with an empty Hall cross, without a sample on top, the local magnetisation is

defined as

$$M = \frac{\langle B \rangle}{\mu_0} - H \tag{4.5}$$

where the first term is directly proportional to the Hall voltage. All these effects influence the quality of the Hall probe. If the corner radius becomes too large, more electrons will be guided along the side walls, which affects the Hall coefficient at moderate magnetic fields. At very high magnetic fields, when the cyclotron orbit of the electrons becomes smaller than the Hall cross, the electrons move in skipping orbits along the edges of the channel. In this case, not only the magnetic field in the Hall cross, but also the field through the leads will influence the Hall voltage. With increasing temperatures, the mean free path of the electrons decreases, leading to a crossover from the ballistic regime to the diffusive regime at high temperature, which gives rise to greatly increased noise in the Hall probe.[207] Signatures of the quantum Hall effect (QHE), which also causes a strong non-linear behaviour of the Hall voltage at high magnetic fields, were suppressed by the use of high currents in the Hall probes. In addition, most measurements were taken at fields much lower than the fields where these effects start to govern the behaviour of the Hall probe (typical magnetic fields at which the measurements were taken were ≈ 10 mT and are much lower than fields of the order of 1 T where the QHE is usually observed).[207–209] Most of these problems can be overcome, by measuring an empty Hall probe as a reference, whose signal can then be subtracted.

4.2 Design and fabrication of the Hall-probes

The design used for the fabrication of the Hall probes has nine active areas in a linear arrangement. All Hall probes could be contacted individually to measure the Hall voltage, while the current is applied through one shared current line. In the last fabrication step, two different sizes of Hall probes were available, one with 1 µm × 1 µm and one with 2 µm × 2 µm active areas. A detailed description of the layout can be found in the PhD thesis of M. Engbarth.[193]

The Hall probes were fabricated from a GaAs/AlGaAs wafer (C2276 and A3542)

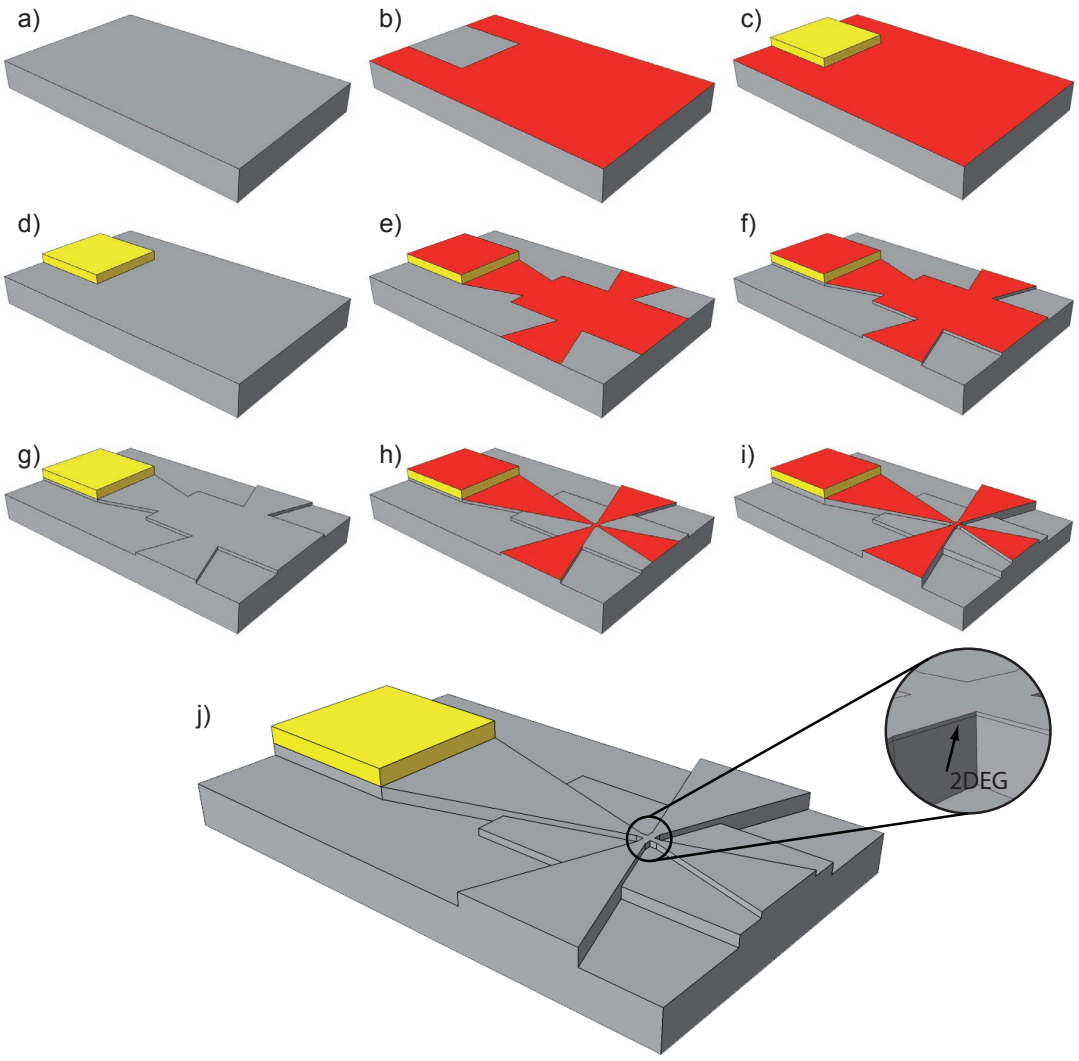

Figure 4-3: Sketch of the photolithography steps performed during the fabrication of the 2DEG Hall probe devices. The process is shown for one Hall cross. The steps are discussed in the text.

with a 2DEG about 70 nm below the surface. The 2DEG is formed between a 60 nm AlGaAs top layer and the undoped GaAs. The electrons for the 2DEG are provided by a 40 nm Si doped AlGaAs layer with a doping density of $N_D = 1.1 \cdot 10^{18}$ m^{-3}. A 10 nm layer of GaAs protects the surface serving as a cap layer. Before starting the photolithographic process, the wafer was cut into square pieces with a size of 3.8 mm $\times$ 3.8 mm, the maximum size to fit into the cavity of the chip carriers. A small number of chips were than fabricated in parallel.

Prior to starting the fabrication, the chips were cleaned. The cleaning was done in an ultrasonic bath for five minutes in three solvents, trichloroethylene, acetone and isopropanol. The chips were then blown dry with clean nitrogen gas and glued to a glass slide to simplify handling.

In the first step, Ohmic contacts are prepared on the chip (Fig. 4-3a). It was first covered in photoresist (Shipley Microposit S 1813) and spun at 3500 rpm for 30 s. The chip was then placed in an oven at 90°C. After 15 min, the chips were taken out and soaked in chlorobenzene for 3 min and then baked for another 15 min. The chlorobenzene bath half way through the baking process removes some of the solvents in the photoresist and hence hardens its top surface. A chrome mask of the desired pattern was then used to expose the photoresist with UV light where the Ohmic contacts should be placed. The exposure time varied slightly with the age of the UV lamp in the mask aligner, and was roughly between 10 s and 30 s. The exposed photoresist was then removed by immersing the chip in diluted (3.5:1) Microposit 351 developer for about 20 s. A number of test chips were prepared in the same way before the actual chips, to determine the optimal exposure time. After developing, the chips were washed in deionised (DI) water and blown dry with nitrogen. The hardened top surface develops less than the bulk of the photoresist, forming an overhanging profile, which is necessary for a successful lift-off in the next step (Fig. 4-3b).

To remove surface oxides from the GaAs cap layer, the chips were dipped for 30 s in 1:1 HCl:H_2O and then washed in DI water. The chips were then mounted in a thermal evaporator which was then evacuated immediately. An argon glow discharge was applied for 10 min to further clean the surface of the chips. Then, 66 nm germanium (Ge), 133 nm gold (Au), 20 nm titanium (Ti) and another

200 nm gold were deposited onto the chips (Fig. 4-3c). The chips were then removed from the thermal evaporator and placed in a beaker with acetone. The acetone dissolves the photoresist and hence lifts-off the unwanted material from the chip, leaving only the Ohmic contacts (Fig. 4-3d). Most of the material was lifted-off after 48 h, any remains were carefully removed either by squirting acetone on the chip or placing the beaker in a low power ultrasonic bath.

The cleaned chips were then annealed for 15 s in a 95 % N_2 + 5 % H_2 atmosphere at 410°C. In this step an n^+ region is formed between the GaAs and the deposited Ge/Au below the pad, which results in a low resistance contact. The two top layers (Ti/Au) form a good top surface for the later bonding of the device.

After assuring that all contact pads have a good, low resistance contact to the chip, using a micro probing station, the chips are cleaned again and re-glued to a cover slide. The sample is again covered with photoresist and spun at 5000 rpm for 30 s. For the following steps a very close contact between the photoresist surface and the mask is absolutely necessary to transfer sharp details of the pattern. If the mask is not in perfect contact with the photoresist, the UV light will be scattered at the corners of the pattern which results in unsharp edges. When the sample is spun with the photoresist, edgebeads form on one or more corners of the chip. To remove these, an edgebead mask is exposed into the photoresist. This mask is exposed for 30 s and subsequent development removes the resist around the corners, ideally leaving a perfectly flat square for the next step. If, however, an edgebead survives this step, it is carefully removed with a scalpel. A coarse mask is then exposed in the photoresist, which covers the central area of the chip, where the Hall crosses will be, as well as the leads from the Ohmic contacts to the Hall probes, Fig. 4-3e. Again, a series of test samples was prepared to find the exposure time which leads to the best result and the sharpest corners.

A solution of H_2SO_4, H_2O_2 and H_2O in ratio 1 : 8 : 160 was prepared to etch the structure into the chip. After a 30 s bath in 1:1 HCl:H_2O to remove the surface oxides, the chips were etched to a depth of about 100 nm. The etch rate was calibrated with a couple of test chips and a Dektak profiler (Fig. 4-3f). The photoresist was then removed with acetone (Fig. 4-3g).

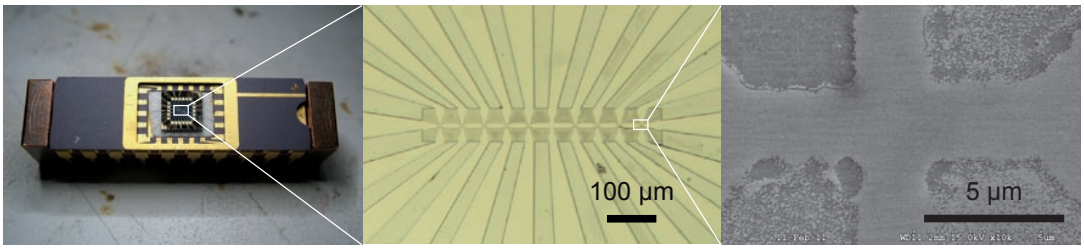

Figure 4-4: The ready Hall probe array attached and wire bonded to a 20 pin DIP chip carrier (left), an optical micrograph of the nine active Hall crosses (middle) and an electron micrograph showing a single 2 µm Hall cross.

For the fine etch, the chips were prepared as in the last step, and spun at 7500 rpm for 30 s. First, the edge beads were removed, and then the final mask with 1 µm or 2 µm Hall crosses was exposed into the photoresist (Fig. 4-3h). Finally the chip was etched another 40 nm (Fig. 4-3i), leaving the Hall crosses and leads as structured mesas on the chip. After removing the photoresist with acetone (Fig. 4-3 j), the chips was cleaned again and the resistances of the Hall probes were checked again using the micro probing station. This two step etching is beneficial as, for the small features such as the actual Hall probes, as little as possible should be etched, ensuring the survival of fine details in the pattern. On the other hand, for the leads, it is beneficial to etch slightly deeper, to get a good separation of the 2DEG in the contact leads from the rest of the chip.

4.3 Experimental set-up

The final chips, fabricated in the last step, were then mounted on a 20 pin ceramic dual inline pin (cerDIP or DIP) chip carrier package. (*cf.* Fig. 4-4a) The DIP has the advantage, that a large area of the chip carrier can be brought into close contact with the copper heat sink of the sample holder, and hence allows a good control of the temperature of the chip. To be able to image the samples on the Hall array with an AFM, the chips were first glued on a piece of alumina and then put into the cavity of the DIP package. In that way, the chip was slightly raised, making it accessible to the tip in the AFM.

The 20 pins of the DIP were then wire bonded to the Ohmic contact pads on

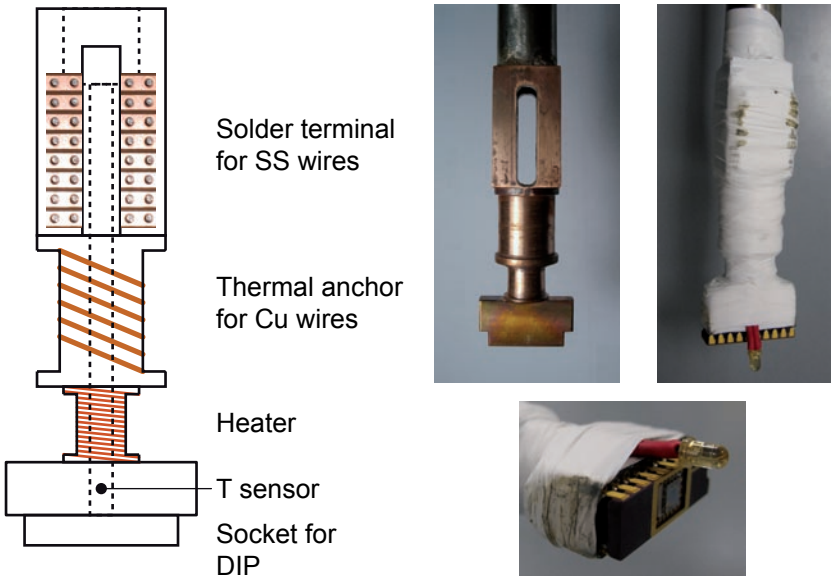

Figure 4-5: Sketch and photograph of the new sample holder. The core is made from copper. The connected and loaded sample holder is wrapped in PTFE tape for protection and insulation. The close up shows the IR LED, used to illuminate the 2DEG.

the chip, using 25 µm gold wire. Two connections were used for the current line, shared for all Hall crosses and the other eighteen for the voltage leads of the nine Hall probes. To lower the risk of loosing a Hall probe if the wire pops off, either by the vibrations of the vacuum pump, or by thermal strain due to cooling down or heating up the sample, all connections between the chip and the DIP package were made twice, using two wires bonded parallel to each other to the same contact pad and the same contact on the chip carrier.

A new sample holder was constructed, which is shown in Fig. 4-5, to hold the 20pin DIP packages with the Hall arrays. In the old system, thermal contact between the copper heat sink and the sample was made only by a small copper braid (*cf.* Engbarth 2010)[193] allowing only poor control over the temperature of the sample. For the new sample holder care was taken that the full bottom surface of the DIP was in contact with the copper part of the sample holder. Some Apiezon Grease N was used to bond the DIP non-permanently to the copper and get a good thermal contact. As can be seen in Fig. 4-5, the temperature sensor is in a hole bored in the copper, just next to the sample. Above that, a high resistance wire is wound around the holder acting as a heater. Above that, a

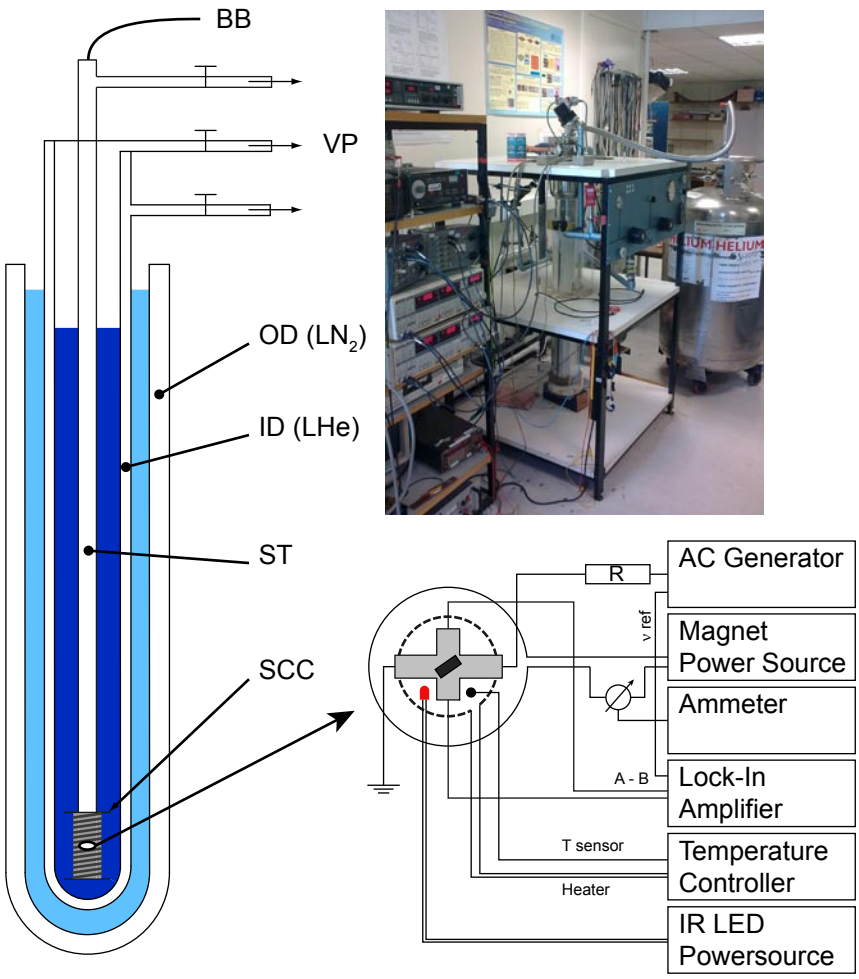

Figure 4-6: Sketch of the cryostat and the electrical set-up. A photograph shows the set up during the process of filling it with liquid helium. The details are described in the text.

large area is provided to thermally anchor the twisted pairs of copper wires which come from the DIP socket. The wires were glued to the sample holder, using GE varnish. Above that, the Cu wires are soldered to stainless steel (SS) wires, which have a very low thermal conductivity, which are then brought up through a stainless steel tube to the breakout box. An infrared light emitting diode (IR LED) is glued to one side of the sample holder. The LED could be used to illuminate the Hall probes, which excites electrons from deep-donor states in the AlGaAs layer into the conduction band.[210] This was only done if the resistances of the Hall probes were much higher than usual.

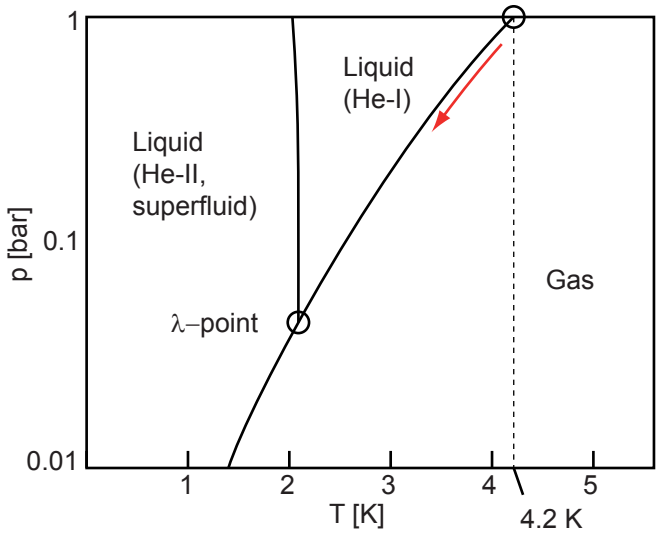

Figure 4-7: The phase diagram of ^{4}He. At ambient pressure, ^{4}He boils at 4.2 K. If the pressure is lowered, one moves down the phase boundary (red arrow) and hence T is decreased as well.

Fig. 4-6 shows the cryostat and the electrical set-up for the experiments. The cryostat, which was used for the measurements presented in this work, consists of two glass dewars. The outer dewar (OD) has a sealed insulating vacuum jacket and was filled with liquid nitrogen (LN_2) to cool the inner dewar (ID). The vacuum jacket of the inner dewar could be connected to a vacuum pump (VP), and the vacuum was renewed before every measurement. The top of the inner dewar was fitted with a rubber O-ring and sealed vacuum tight against a metal flange. The inner dewar was usually filled with liquid helium (LHe). The helium chamber was also attached to the piping of the vacuum pump. Pumping on the helium was necessary for temperatures lower than 4.2 K (*cf.* Fig. 4-7). The rotary pump used in combination with the cryostat was able to lower the vapour pressure of the liquid helium to achieve a base temperature of about 2 K. The sample tube (ST) with the attached superconducting coil (SCC) was immersed in the liquid helium in the inner dewar. It was attached to the vacuum pump as well, allowing one to evacuate the sample chamber and fill it with helium gas prior to filling the inner dewar with liquid helium. Three vacuum tight feed throughs were used to connect the cables from inside the sample tube to the breakout boxes (BB). The superconducting coil was attached to the outside of the sample tube and hence directly immersed in liquid helium whenever the cryostat was in

use. Sample tube and sample holder were designed in such a way, that the Hall array was placed exactly in the middle of the coil, where the magnetic field is most homogeneous. (data sheet for Superconducting Magnet Job Number 2907, Cryogenic Ltd.)

The magnetic field was controlled by a Kepco bipolar power supply which was run in voltage mode. The voltage was applied to a resistance of 22.5 Ω, 50 Ω or 200 Ω which was connected in series with the superconducting coil. The current was measured with a Keithley Ammeter (Keithley 199 System DMM/Scanner Multimeter). This configuration had the advantage, that the full range of 50 V of the powersupply could be used, resulting in very small field steps. For the work on tin samples (see Sec. 5) magnetic fields of H_{max} =250 G were sufficient, while a small step size $\Delta H \approx 0.1$ G was preferable. Both devices, the ammeter and the power supply, were connected to a computer via a general purpose interface bus (GPIB). The current for the Hall probes was provided by a Philips PM 5109 low distortion AC generator with an output of 10 V which was applied to a resistance of 500 kΩ, which is much higher than the resistances of the current line. Usually a frequency of $\nu_{ref} \approx 314$ Hz was used. This frequency was used as the reference signal for two (three) Stanford Research SR830 digital lock-in amplifiers. The two voltage leads of the Hall probe were connected to the two inputs and the difference voltage was measured. Usually one lock-in was used to measure an empty Hall probe, while the second lock-in was used to record the signal from the actual sample. Depending on the noise level of the Hall probe and the strength of the measured signal, the time constant (TC) was set between 30 ms and 1 s. The phase was set by pressing "auto phase" at a low, positive magnetic field. Usually the phase could be kept constant for a whole series of measurements. The lock-ins were connected to the computer using GPIB connections as well.

The temperature was controlled with a Lakeshore DRC-91CA temperature controller, which was calibrated to the carbon glass temperature sensor in the sample holder. For measurements at $T < 4.2$ K, we waited until the pressure in the helium chamber stabilised and a constant base temperature was reached. The sample holder was not in thermal contact with the helium bath, hence the temperature equalisation occurred only via the helium gas in the chamber or by radiation. Especially for $T < 4.2$ K, most of the helium gas was condensed at the

bottom of the sample tube and the thermal equalisation became very slow. We observed a slight offset between sample temperature and measured temperature when the sample was heated. At T_c^{Sn} this offset was typically $\approx$ 200 mK. To account for that offset, a linear correction between the base temperature and T_c of the sample was applied to the reduced temperature scale. To illuminate the sample, an ordinary battery was connected to the LED.

A custom designed LabVIEW program was used to sweep the external magnetic field and record the Hall voltages of the individual Hall probes. The wait time between loops was set to a value $\approx 3 \times$ TC of the lock-ins. A typical data set consisted of an initial sweep from $H = 0$ to $H = +|H_{max}|$ (red curve in Fig. 4-8), than a sweep from $H = +|H_{max}|$ to $H = -|H_{max}|$ (green curve in Fig. 4-8) and a last sweep from $H = -|H_{max}|$ to $H = +|H_{max}|$ (blue curve in Fig. 4-8). If the latter two sweeps were not mirror inverted, one knew that there was a problem with the measurement. The curves in the figure are offset for clarity.

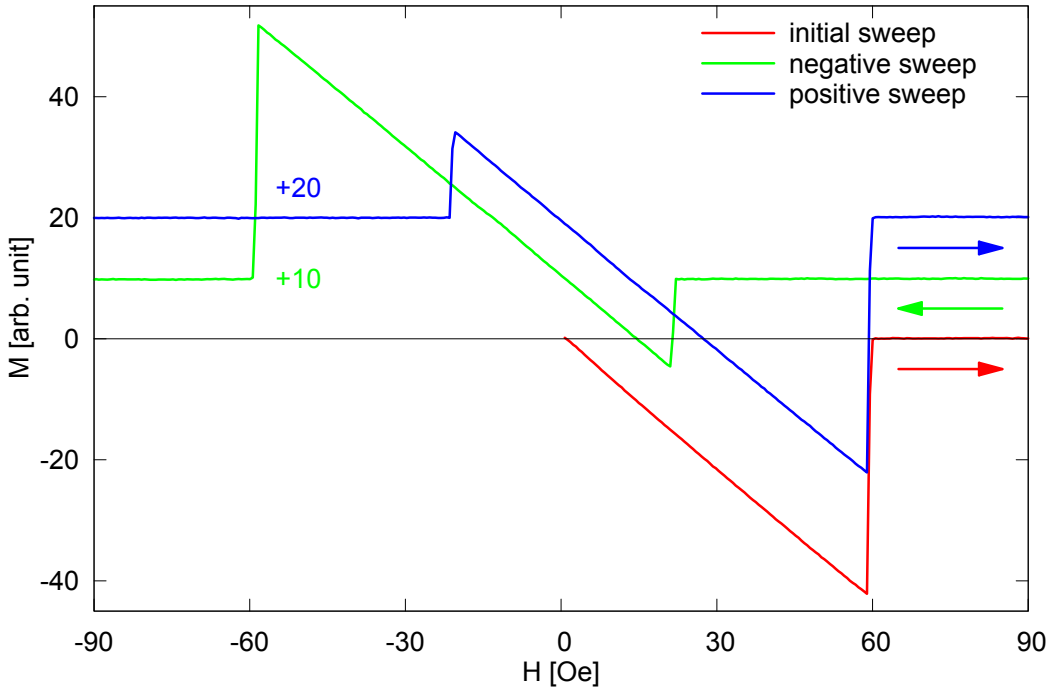

Figure 4-8: A graph showing a whole sweep for one sample. The initial sweep from zero field (red), a negative sweep (green) and a positive sweep (blue). The curves are offset for clarity.

4.3.1 Sample preparation

For the micromagnetic measurements the sample needs to be positioned near to the centre of one Hall cross. Usually, a single crystal is chosen from the working electrode and transferred to the Hall array. To manage the transfer of the sample from the electrode to the Hall probe a micro/nano manipulator is used. The manipulator consists of a cantilever attached to a piezoelectric three-axes positioner. The piezo positioner is able to move the lever in steps of about 200 nm and can be fitted *e.g.* with either a 1 µm tungsten tip (W-tip) or a nylon hair, attached to a needle. The base which is used to hold the sample can be heated to melt the paraffin wax which is used as both lubricant and glue for the samples.

To pick up a sample, the tungsten tip was covered in paraffin wax. Paraffin wax was placed on a glass slide and heated above its melting temperature. The

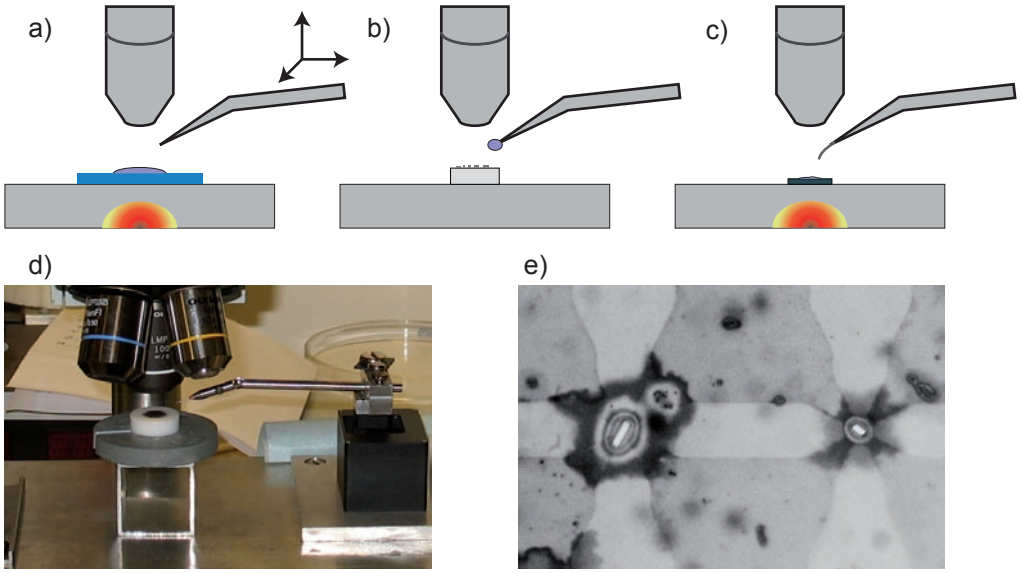

Figure 4-9: Sketch of the steps to position the sample (a-c), discussed in the text. A photograph of the set-up is shown in d) and an optical micrograph of two tin rods on two adjacent Hall probes is shown in e).

tungsten tip, still at room temperature, was dipped in the wax and a small amount of wax frozen around the tip, Fig. 4-9a. The glass slide was then replaced with a working electrode, on which the samples of interest were grown. The W-tip

with the wax blob was then brought into contact with the desired sample. Under the microscope it is possible to navigate to a certain sample and pick this up, just by touching it with the wax, Fig. 4-9b. The wax blob with the sample was than carefully lifted and the working electrode was exchanged to a Hall array. The Hall array was heated and the W-tip was brought close to one of the leads connecting the Ohmic contacts and the active Hall probe areas. Care was taken that the W-tip was not touching the surface of the Hall array, especially not close to the active central part of the Hall probes, to avoid any damage to the cap layer and the 2DEG of the chip. To move the sample to one Hall probe, the W-tip was exchanged for a needle with a nylon hair from an artist's brush glued to the tip Fig. 4-9c. The tip of the nylon hair was typically of size < 1 µm. The chip was kept at a temperature above the melting point of the wax. That way, the wax acted as lubricant for the samples, which were now pushed to the centre of a Hall probe using the nylon hair. Usually eight of the nine Hall probes were loaded with a sample by repeating the above mentioned steps, while one Hall probe was left empty as a reference.

After finishing the micromanipulation, the heater was switched off and the Hall probe was allowed to cool down, freezing the wax. The frozen wax is here an ideal glue to hold the samples in place on the Hall cross and has the additional benefit of providing some protection from the air, hence slowing down the process of sample oxidation. Fig. 4-9e shows an optical micrograph of two samples on two different Hall probes. The frozen "puddle of wax" is easily visible in this image. An argon filled, overpressured chamber was used to store the completed chips prior to their transfer into the sample tube in the cryostat.

To reuse the Hall probes, the Hall array was heated up and the samples were simply pushed away from the Hall cross and moved far away from it. Sometimes the samples were stuck and could not be moved with the nylon hair, in this case cleaning the sample with acetone and isopropanol in an ultrasonic bath was used to clean the sample. This treatment usually removed most of the bond wires between the chip and the chip carrier as well, requiring the sample to be re-bonded. This was usually avoided if possible, as the unintended removal of the bond wires usually caused some damage to the bond pads.

4.3.2 Preparation of measured data

The LabVIEW program used for this work was capable of controlling and recording the current flowing through the superconducting coil, as well as recording the Hall voltage of up to three lock-ins. The steps necessary to convert the current and voltage to magnetisation data are shown in the following paragraph.

The magnet used for the measurements in this work produces a magnetic field of

$$\frac{B}{I} = 0.112414\frac{\mathrm{T}}{\mathrm{A}} = 1.12414\frac{\mathrm{G}}{\mathrm{mA}}. \tag{4.6}$$

This is used to calculate the applied field from the current flowing through the coil. The graph in Fig. 4-10a shows the raw data of a tin rod, U_H vs H_{ext}. The Hall coefficient for the loaded (black) and the empty Hall probe (red) are slightly different, which is visible in the different slopes of the data. This is due to the fact that no two fabricated Hall probes are identical. To extract the Hall coefficient for the loaded Hall probe, the parts of the data, where there was clearly a magnetisation signal from the sample were masked out and to the rest of the curve a linear fit ($f_1(x) = a_1 \cdot x + b_1$) was applied (dotted curve). If no signal from the sample is apparent, the measured magnetisation and the applied field should be identical. This slope therefore gives the coefficient to convert U_H to M.

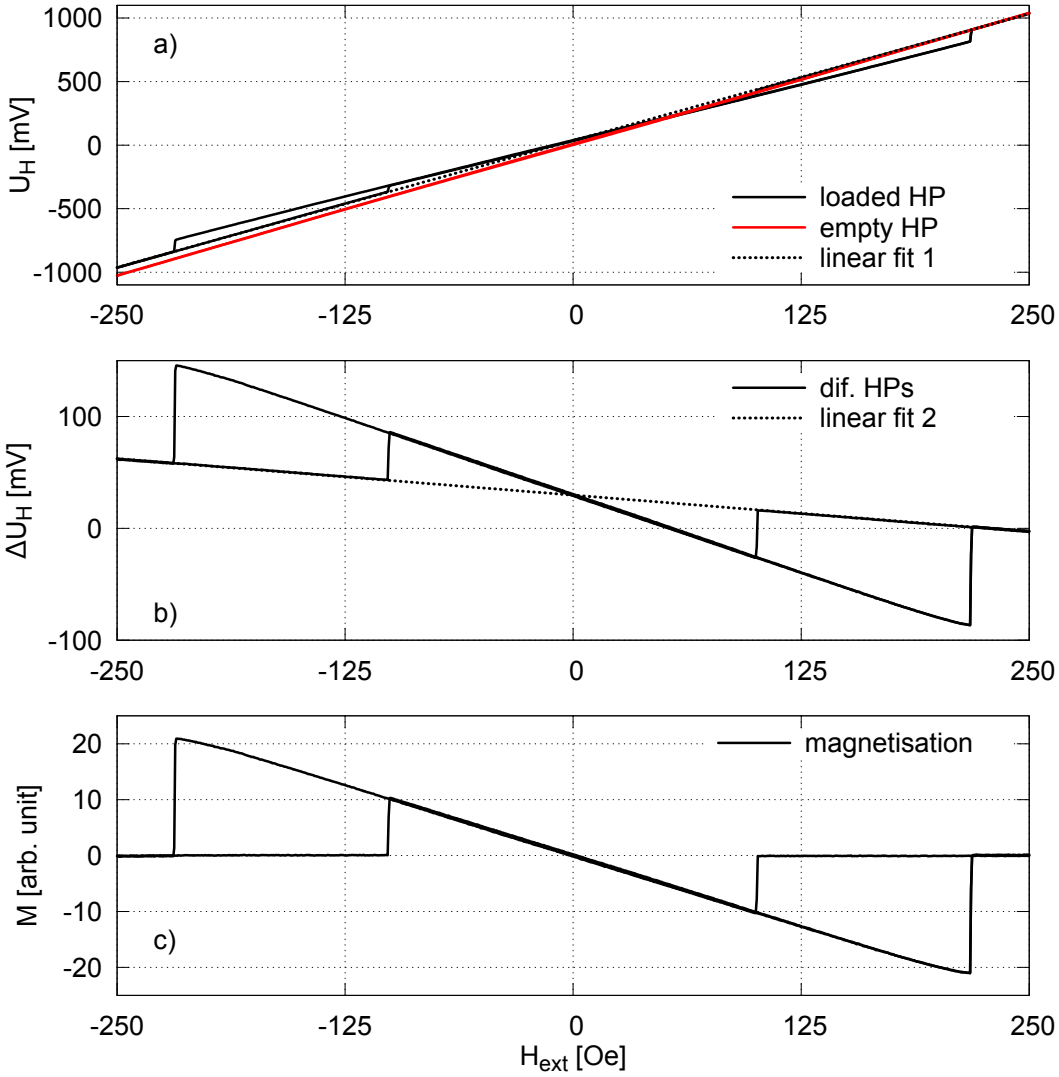

Figure 4-10: The measured Hall voltage U_H for a loaded and an empty Hall probe (HP), and a linear fit to the background of the loaded HP (a). Subtraction of the empty HP and another background fit (b) and the final magnetisation data (c).

In the next step, Fig. 4-10b, the data from the empty Hall probe is subtracted from the data of the loaded Hall probe. Usually the data was recorded simultaneously, giving identical applied field data for any measured point. The two different Hall coefficients for the Hall probes require another linear fit ($f_2(x) = a_2 \cdot x + b_2$) to the difference data of the sample. In the last step, Fig. 4-10c, this slope is subtracted from the difference and the data is divided by the slope from the first fit (the Hall coefficient), leading to the magnetisation

$$M = \frac{((U_H^{\text{loaded HP}} - U_H^{\text{empty HP}}) - f_2(H_{ext}))}{a_1} \tag{4.7}$$

which is measured by the loaded Hall probe.

For some Hall probes, especially at large fields, a simple linear fit was not sufficient to remove the nonlinearities between the loaded and the empty Hall probe. In these cases a cubic fit ($f(x) = a \cdot x^3 + b \cdot x^2 + c \cdot x + d$) of the data was used instead of the linear fit. However, for measurements of ferromagnetic samples (*cf.* Sec. 7), the saturation magnetisation of the sample has to be taken into account as well. Here a fit to $f(x) = a \cdot x^3 + b \cdot x^2 + c \cdot x + d + e \cdot \frac{|x|}{x}$ was used to take this into account. The last parameter e, which is a measure of the magnetisation due to ferromagnetic behaviour, was discarded after the fitting and only the cubic part of the function was subtracted from the data.

From the magnetisation data analysed in this way two critical fields are measurable. The superheating field H_{sh} and the supercooling field H_{sc} are accessible, depending on the sweep direction. Fig. 4-11a shows the same data as Fig. 4-10c for negative external fields around the critical fields. Here, data were recorded every $\Delta H_{ext} \approx 0.5$ G. Fig. 4-11b, c show the abrupt jump at H_{sh} for increasing fields (black curve) and H_{sc} for decreasing field (red curve) respectively. For the value of the superheating field H_{sh}, the first datapoint wich shows $M = 0$ was taken as the value for the given temperature. For the value of the supercooling field H_{sc}, the last point with $M = 0$ was taken as the value for the given temperature. This definition allowed consistent determination of the critical fields for all measured temperatures, especially close to T_c, where the jump is not as sharp as for $T \ll T_c$. The so determined dataset of $H_{sh}\,(T)$ and $H_{sc}\,(T)$ can then be analysed further, as shown in the next chapters.

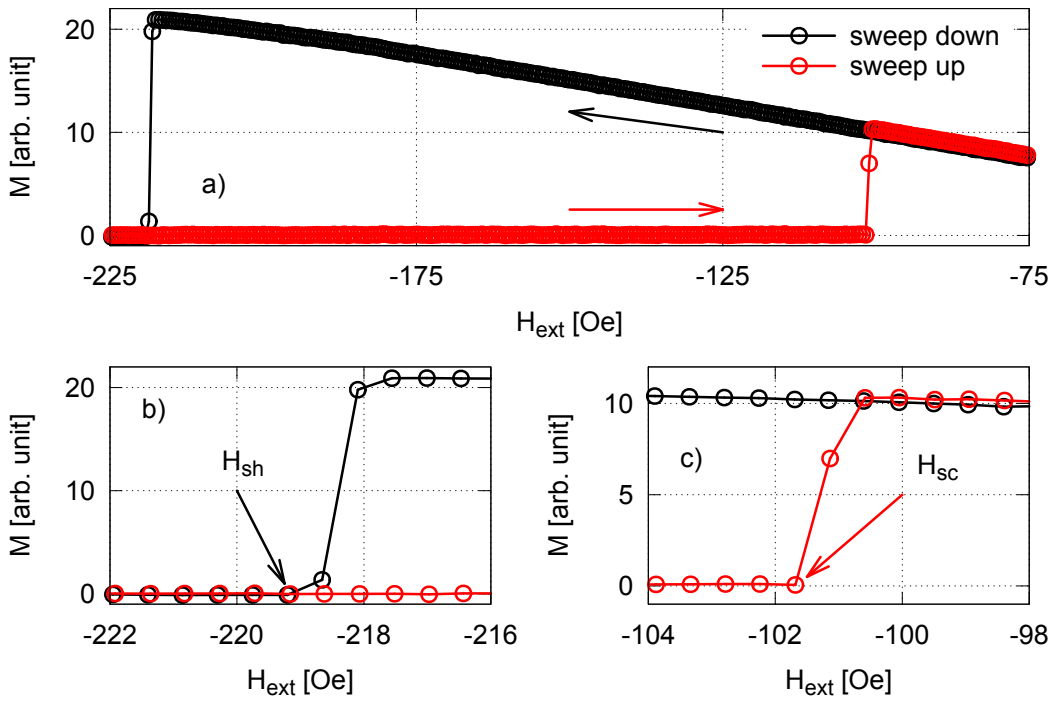

Figure 4-11: A close up of the graph in Fig. 4-10c is shown in (a), indicating the sweep directions. The two critical fields H_{sh} (b) and H_{sc} (c) are defined by the first(last) point where the criteria $M = 0$ is met.

For the fitting, Origin 6.1 was used, while for the determination of the critical fields a data picker program was written in LabVIEW. The program allows the quick comparison of curves recorded at different temperatures, alleviating the difficulties of identification of the critical field in very noisy data, or data recorded very close to T_c, while all the background corrections could be made for either all curves, or individually for each measurement.

Chapter 5

β-tin micro crystals

The following section concentrates on pure β-tin microcrystals of various sizes and shapes. Bulk tin is a type I superconductor with $T_c = 3.7227$ K and $H_c(0) \approx 303$ G.[24,211–213] $H_c(0)$ in particular, shows some spread in the values obtained by different groups. Studies show that the coherence length, ξ, and penetration depth, λ, depend on the crystallographic directions, although most studies focus on polycrystalline films or randomly oriented samples.[58,59,71,87,90,214,215] The value of the GL-parameter, κ, which depends on ξ and λ, is hence not known unambiguously.[48,59,211,216] Values in the literature range from $\kappa \approx 0.09 - 0.15$. However, a recent study suggests that the discrepancy arises mainly from different methods of calculating κ from the critical fields and that the actual value is closer to $\kappa = 0.1$.[217]

All samples investigated in the following sections were grown electrochemically. For the rod-shaped samples, with the simplest geometry to discuss mesoscopic effects, a close study of the effect of different sizes, especially the widths of the samples, was made. The thin slab is well studied theoretically, mainly because it is easy to simulate a rectangular geometry (*cf.* Sec. 2.3.4). Results from triangular platelets are also discussed in Sec. 5.2.

5.1 Tin cuboid crystals

5.1.1 Sample preparation

The preparation of all the samples was by electrodeposition as described in Sec. 3.3.1. Cuboid shaped samples form at the low end of deposition potential and tin concentration as shown in Fig. 3-9b or in the inset in Fig. 5-1. Although one would expect the samples to be similar in width and height, some of the crystals were much flatter than wide. To pick the crystals with $w/h \approx 1$ the crystals were imaged using an AFM, which allows full 3D imaging, before positioning them on the Hall array. The AFM is an excellent tool to measure the height of the crystals, however, measuring the width is more complicated, as the shape of the tip and the sharp steep sides of the samples lead to some artefacts in the scans. For the measurement of width w and length l of the crystal, SEM images were used instead. The positioning of the samples was described in Sec. 4.3.1.

5.1.2 Magnetisation data

The recording and preparation of the magnetisation data was already described in Sec. 4.3.2. The magnetisation curves $M(H)$ for three different rods (the largest, one intermediate sized and the smallest sample) at a temperature of 3.35 K ($T/T_c = 0.9$) are shown in Fig. 5-1, with the original SEM images as an inset. It will be seen, that the most important dimension of t6he crystal is the width and hence the pyramidal cap of the largest rod is probably without any effect to the final results. The individual critical temperatures as measured from the experimental data are spread by ≈ 10 mK. At first sight it is clear that all transitions from the normal to the superconducting state and *vice versa* are perfectly type I like, with no hint of an intermediate state. At low temperatures, all magnetisation curves showed a similar behaviour. The curves in Fig. 5-1 were recorded with a negative sweep direction (sweep from positive to negative fields, corresponding to right to left in the figure), and are identical to the mirror-inverted curves in the opposite sweep direction. Both critical fields, $H_{sc} = H_{c3}$, which is identified

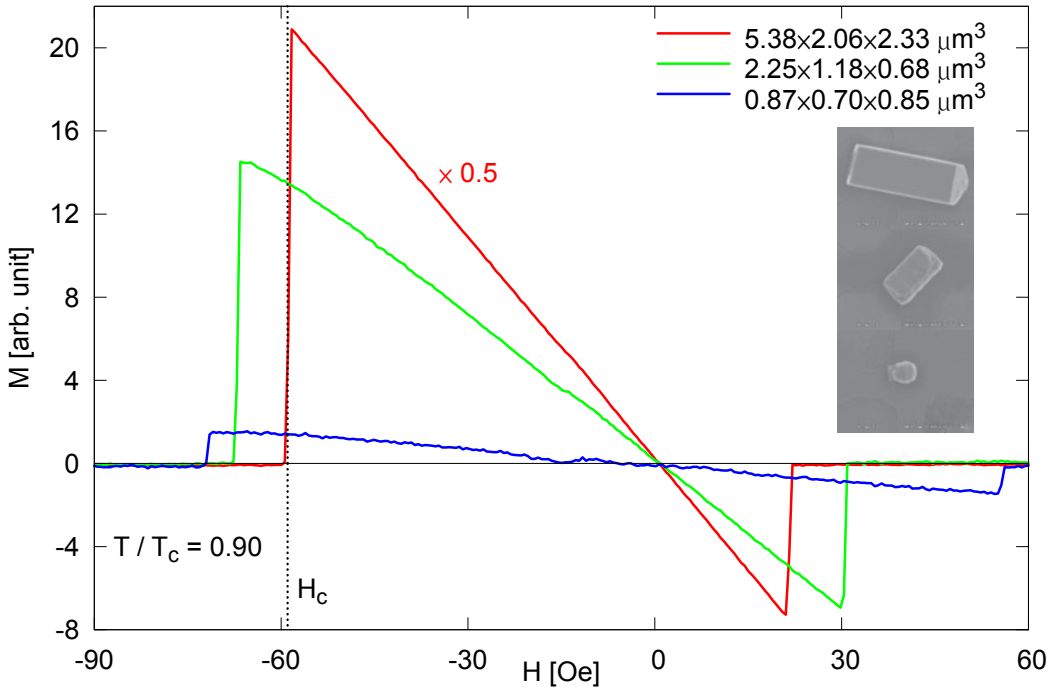

Figure 5-1: Magnetisation data $M(H)$ for three different sized crystals at a temperature of $T/T_c = 0.9$. The data for the largest rod were scaled for clarity. The field was swept from positive to negative field (right to left in the image), the values for the supercooled and superheated critical field clearly change for the different samples. The inset shows SEM images of the three crystals.

with the field where superconductivity nucleates in the sample (here at positive values of H) and H_{sh}, where superconductivity is destroyed in the sample (at negative values of H) are clearly size-dependent at this temperature. The exact dependencies are discussed below.

The dependence of the critical field on the width of the sample was discussed in Sec. 2.3.4. Fig. 5-2 shows the values for H_{sh} and H_{sc} as a function of the reciprocal width w^{-1} for four different temperatures. The top graph displays the superheating field, which is approximately independent of temperature and size. This is different from the supercooling field, which clearly exhibits a T-dependence. In terms of the two superconducting length scales, $\xi(T)$ and $\lambda(T)$, samples enter the mesoscopic regime either upon decreasing the sample size, or increasing the temperature, which increases both lengths ξ and λ. The graph in Fig. 5-2 illustrates both effects for the supercooling field. A bulk sample

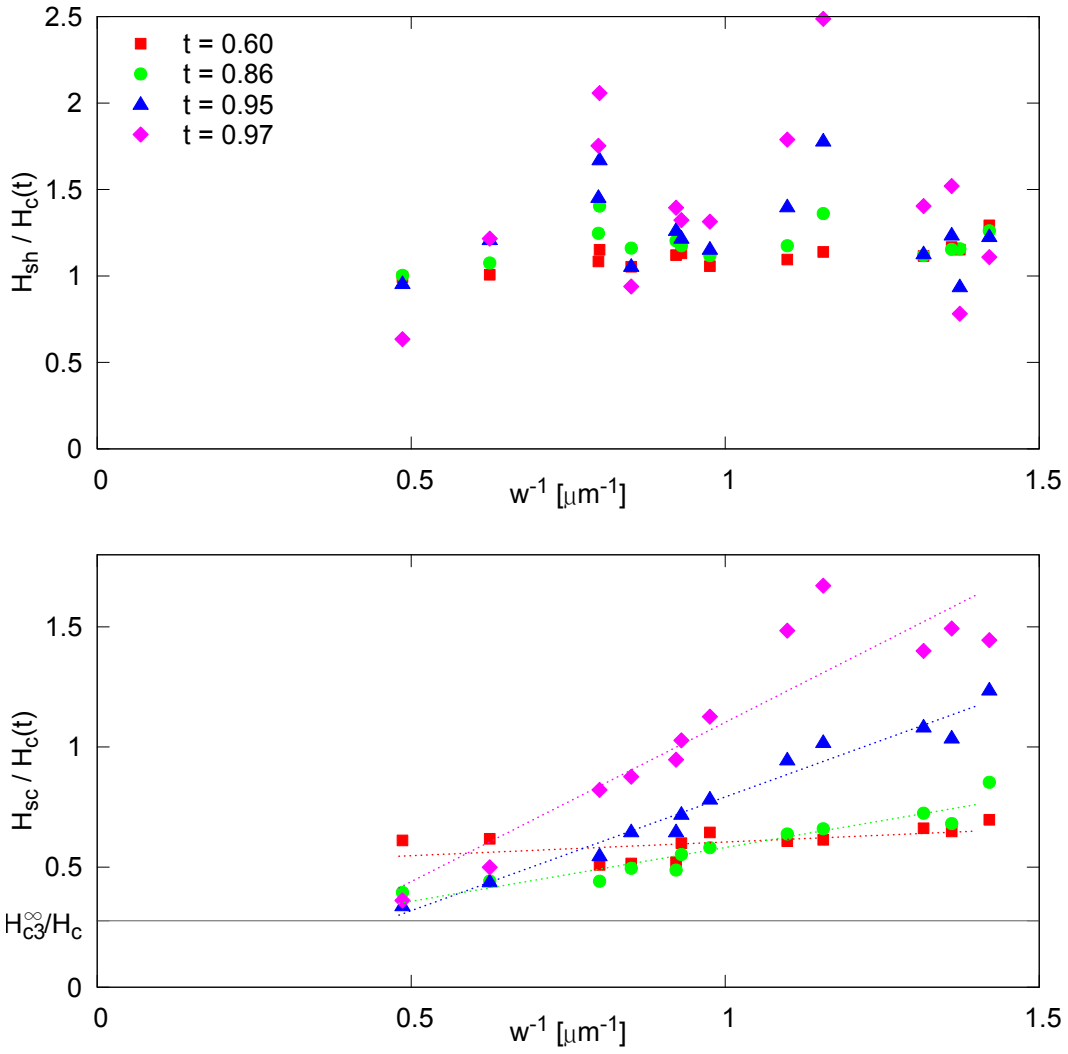

Figure 5-2: Superheating, H_{sh}, and supercooling fields, H_{sc}, as a function of the reciprocal sample width w^{-1} for different temperatures t. While H_{sh} shows no clear trend, H_{sc} shows a clear w^{-1} dependence. The bulk value for right angled samples, H_{sc}^{∞}, is marked as grey line.

$w \gg \xi, \lambda$ and hence $w^{-1} \to 0$ enters the mesoscopic regime at a temperature extremely close to T_c, while smaller samples do so at lower temperatures. At low temperatures ($T/T_c \ll 1$) none of the samples is in the mesoscopic regime (red squares at $T/T_c = 0.6$). For higher temperatures (green circles at $T/T_c = 0.86$ and blue triangles at $T/T_c = 0.95$) the supercooling field for the largest samples is basically unchanged, while it increases considerably in small samples. At a temperature of $T/T_c = 0.97$ (purple diamonds), very close to T_c, the increase

is most dramatic. A linear fit to the data at a given temperature is drawn as a dashed line. Although, theoretically, none of the samples is in the limit of $w \ll \xi$, the $\lambda(T)$-dependence expressed by Eq. (2.80) still works well for the samples.

In bulk GL-theory, the supercooling field is not a function of temperature or size, just a function of the angle at the corners. If, however, the sample is regarded as a thin plate in a parallel field, as was discussed in Sec. 2.3.3, the size-dependent behaviour of equation (2.80) is expected. Further, this equation can be used to estimate $\lambda(T)$ as, in this approximation, $H_{sc}/H_c(T)$ can be identified with

$$\frac{H_{sc}}{H_c} = \sqrt{24}\lambda \cdot w^{-1} \tag{5.1}$$

showing that the slope of the lines in Fig. 5-2 is proportional to $\lambda(T)$. Using the value for the slope to estimate the value of λ for a given temperature one gets $\lambda(T/T_c = 0.6) = 0.023$ µm, $\lambda(T/T_c = 0.86) = 0.091$ µm, $\lambda(T/T_c = 0.95) = 0.193$ µm and $\lambda(T/T_c = 0.97) = 0.270$ µm. Especially the values for higher temperatures considerably overestimate the actual literature value of the penetration depth, $\lambda_L(0) = 25 - 36$ nm,[71], because Eq. (5.1) is only valid for $w \ll \xi(T)$. Nevertheless this clearly shows how the samples enter the mesoscopic regime when their dimensions become small compared to the superconducting length scales. For the full temperature range this is better illustrated in the reduced magnetisation plots shown in Fig. 5-3. Here, the change of the superheating and supercooling fields with temperature is easily visible. The bottom panel of Fig. 5-3 shows GL-simulations with the exact measured sample dimensions and ($\xi(0) = 174.5$ nm, $\kappa(0) = 0.25$, $H_c(0) = 303$ G and $T_C = 3.7227$ K) which were performed by Milorad V. Milošević in Antwerp.[218] The agreement between experiment and the simulation is very good with the exception of the increasing experimental superheating field for the smallest sample. The small differences in behaviour can be attributed to the isotropic model used in the simulation, while tin actually has a strongly anisotropic coherence length and penetration depth. Experimentally, only the two transition fields are accessible, while the theoretical plot shows the simulated G-L critical field as a dotted line in addition. This is defined as the field when the superconducting and normal state have equal energies in numerical G-L simulations. The most remarkable

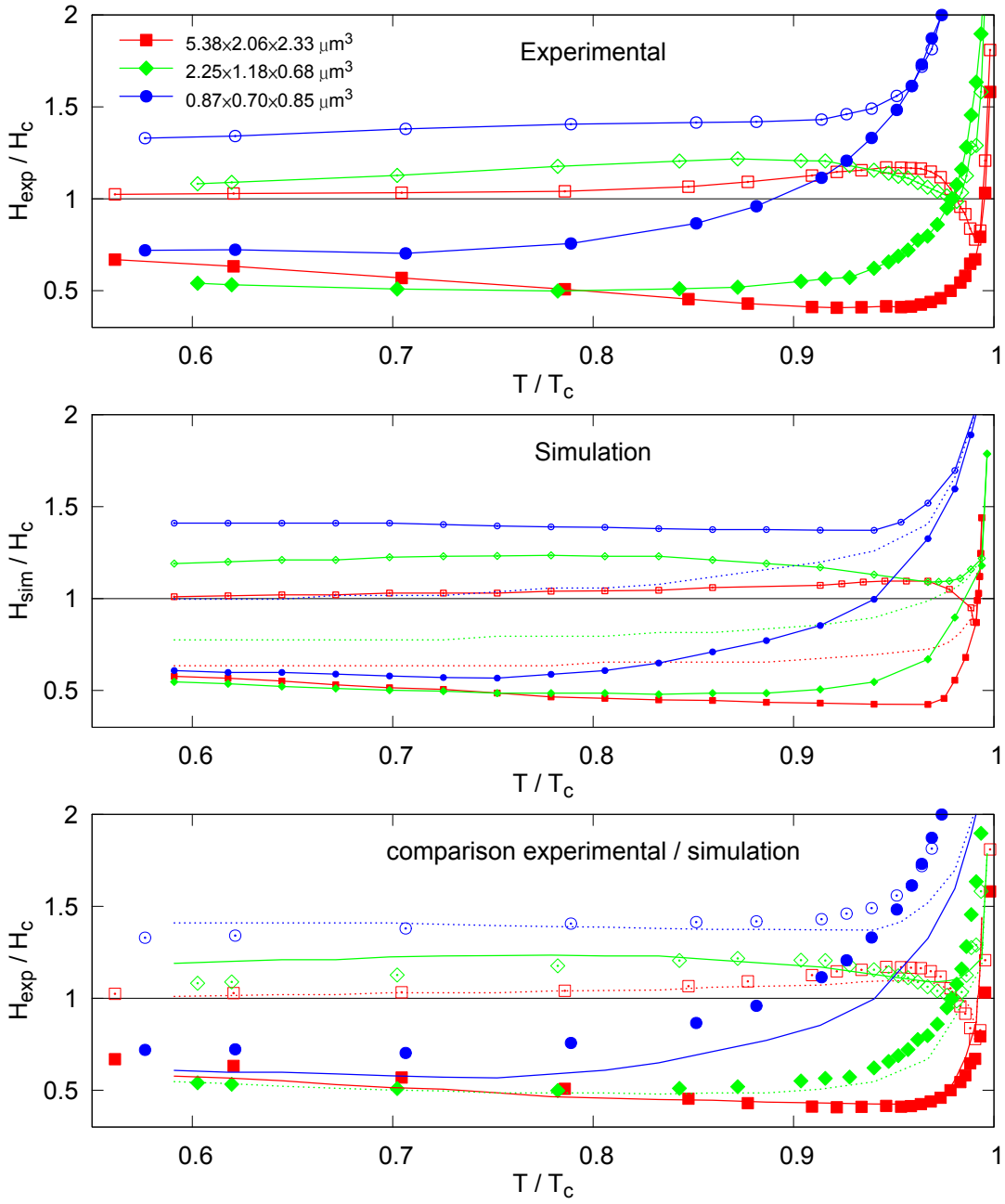

Figure 5-3: Plots of the normalised critical fields H_{sh}/H_c (open symbols) and H_{sc}/H_c (filled symbols) versus reduced temperature T/T_c. The experimental data are shown in the top graph, while simulations with the exact sample parameters are shown at the bottom for comparison. The simulated GL critical field is shown as dotted lines. The bottom graph shows the experimental data as dots with the simulation data as lines for direct comparison.

feature of both experiment and simulation is the drop of the superheating field (defined as the breakdown of superconductivity in the sample) below the bulk H_c value for temperatures approaching T_c, before both fields rise and are enormously enhanced in the regime very close to T_c, where ξ and λ diverge and the samples enter the mesoscopic regime. This region close to T_c, is shown without normalisation in Fig. 5-4. Data are shown for the smallest and largest rod only. The largest rod exhibits "bulk" behaviour up to a temperature of $T/T_c \leq 0.95$, where the temperature dependence of the supercooling field (Eq. (2.52)) is predominantly governed by the temperature dependence of κ (Eq. (2.36)),

$$H_{c3}^{\text{bulk}} \propto \kappa(T) \propto \frac{1}{1+(T/T_c)^2}, \tag{5.2}$$

which is shown by the purple fit to the low temperature data. The smallest sample on the other hand clearly exhibits the temperature dependence of λ for $T/T_c \geq 0.95$ as predicted for the critical field of a very thin slab (Eq. (2.80)) and hence

$$H_{c3}^{\text{slab}} \propto \frac{1-(T/T_c)^2}{\sqrt{1-(T/T_c)^4}}. \tag{5.3}$$

This temperature dependence was calculated for a superconductor where the order parameter at opposite faces is strongly coupled and hence $w \ll \xi(T)$. Saint-James has calculated the width at which superconductivity nucleates in the centre rather than at the edges of the slab (*cf.* Sec. 2.3.3)[91]

$$w = 1.84\xi(0)\frac{\sqrt{1-(T/T_c)^4}}{(1-(T/T_c)^2)}. \tag{5.4}$$

This criterion is met for the small 700 nm wide sample for $T/T_c > 0.81$ and for the large 2000 nm wide sample for $T/T_c > 0.98$. In this regime G-L simulations suggest that the transition is of first order. The order of the phase transition changes from first to second order if the sample size is further decreased with respect to the penetration depth, *i.e.* for a sample with a width $w/\lambda < \sqrt{5}$. For $\lambda(0) = 43.65$ nm this corresponds to a temperature $T/T_c = 0.995$, which is difficult to address experimentally even in small samples. For the blue plot on the graph in Fig. 5-4 for $T/T_c \geq 0.95$, both critical fields converge and the magnetisation of the sample becomes reversible and fits the temperature dependence

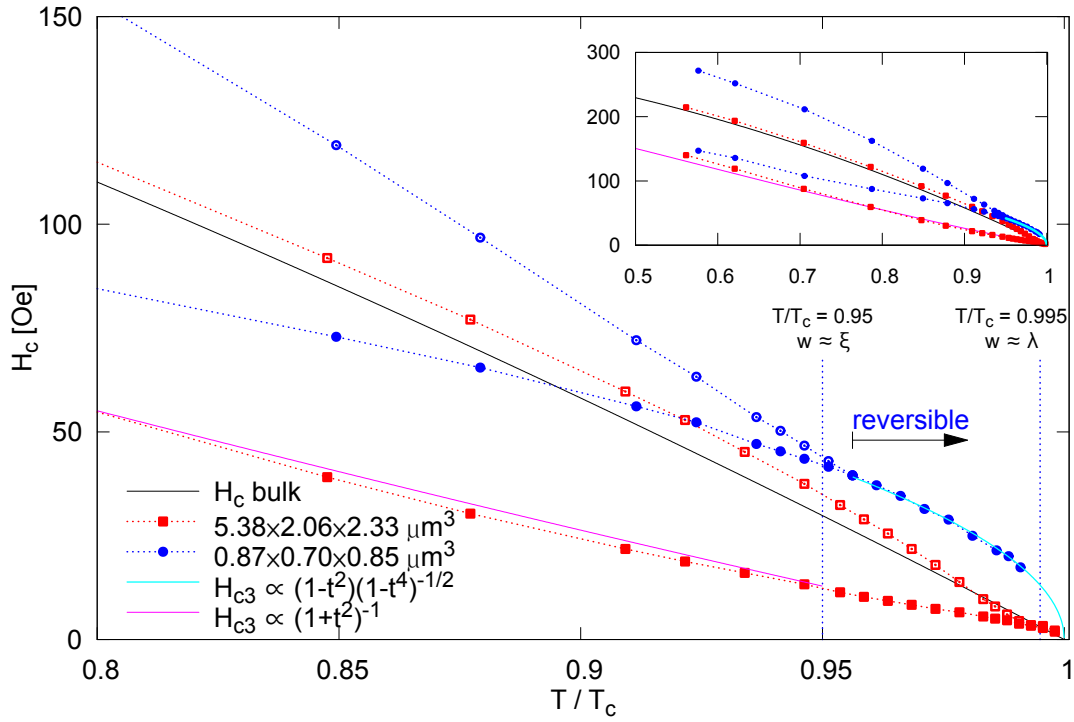

Figure 5-4: Critical fields for the smallest and largest samples examined illustrating the full range of changes in the supercooling (closed symbols) and superheating (open symbols) fields. While for the largest sample (red squares) the bulk model can be well fitted to the supercooling field (red line), the smallest sample enters the mesoscopic regime at a much lower temperature and the data obey the model for very thin slabs in a parallel field (Eq. (2.80)). The inset shows the full temperature range of the recorded data.

of Eq. (5.3) (turquoise line) very well.

As the temperature is increased towards T_c the samples pass through three regimes. For low temperatures ($T \ll T_c$) the samples behave like bulk superconductors with distinct supercooling and superheating fields where $H_{c3} < H_c < H_{sh}$. When the size of the sample becomes much less than the coherence length, supercooling and superheating fields converge on one another $H_{c3} = H_c = H_{sh}$ and the transition, and hence the magnetisation curve, becomes reversible. Even closer to T_c the temperature dependent penetration depth increases until it is comparable to the sample width and the transition changes from a first order reversible to a second order reversible transition. From the experimental data it is not possible to extract the exact temperature at which this last change occurs. Fig. 5-5 shows

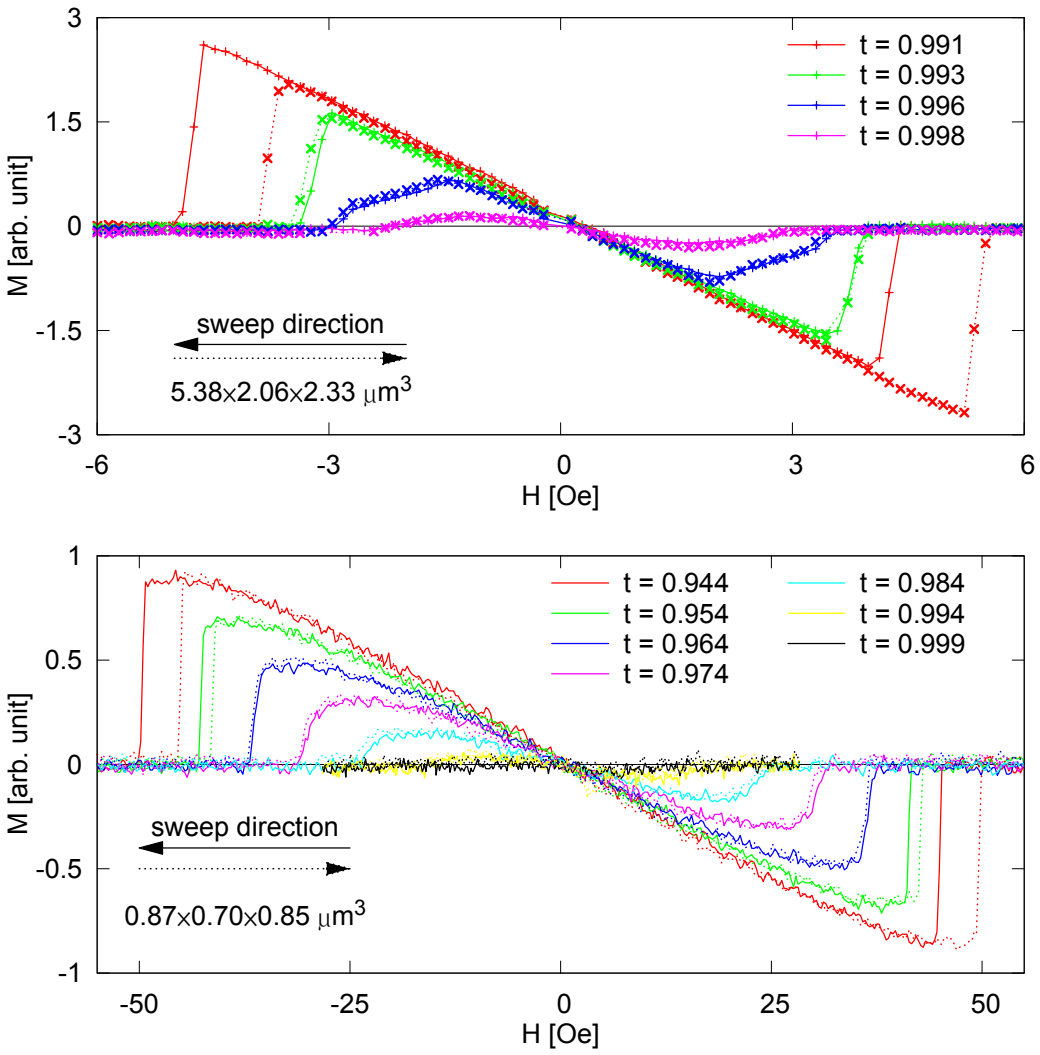

Figure 5-5: $M(H)$ magnetisation curves for the largest and smallest sample just below T_c. For the largest sample, data is limited by the minimum temperature step size, ΔT, of the set-up. The change from irreversible (red curve) to reversible (green curve) is easily seen. For the smallest sample, this change occurs at much lower temperatures and for much larger critical fields. Here the signal to noise ratio limits the measurement close to T_c. Note the different scales for H and M.

magnetisation curves recorded just below T_c. The transitions from the normal state to the superconducting state and *vice versa* of the largest rod occur at two different fields up to a reduced temperature of $t = 0.991$ and are reversible above that value. The smallest possible temperature steps ΔT of the set-up are 10 mK, which limits the recorded temperature resolution of the measurements. Hence,

only two curves in the reversible regime were recorded which appear to show a smooth transition. However, the step size of the magnetic field sweep does not allow a clear statement about the order of the transition to be made. Due to the different volume of the samples, the magnetisation of the smallest rod is comparable for applied fields that are an order of magnitude larger than for the largest sample (note the different H scales in Fig. 5-5). Although the temperature steps are now sufficiently fine to map the onset of the mesoscopic regime as discussed above, the signal-to-noise ratio of the Hall probes limits the data as $T \to T_c$ and the magnetisation of the sample M is very much less than 1 G. The change from irreversible to reversible transitions occurs for this sample between the green and blue curve at $t = 0.964$, *i.e.* at a much lower temperature and much higher fields than for the largest rod. Close inspection of the simulation data of Fig. 5-3 shows that the transition also occurs at a much lower temperature than predicted by the numerical G-L simulation. The change from an abrupt magnetisation jump to a smooth transition is much clearer for this sample. However, the change from a first order phase transition (with a discontinuity in the derivative) to a smooth second order transition (with a continuous change of the derivative) is impossible to identify unambiguously from experimental data since, even if the low field magnetisation changes gradually, the final step might still be discontinuous. In addition, the magnetisation of the smallest rod falls below our noise floor where the crossover from first to second order is expected according to the GL theory (*cf.* Eq. (2.80)).

5.2 Other shapes

In Sec. 3.3.1 it was shown that tin can crystallise in various shapes. Very rarely, thin triangular platelets were found on the electrode. In Fig. 3-10 the corner angle of tin crystals is shown to be $\alpha = 28.6°$. Tin is hence able to grow in triangular shapes with all three edges close to $60° \approx 2 \cdot 28.6°$, forming an almost perfect equilateral triangle as illustrated in Fig. 5-6. AFM images show that these crystals were usually flat with steep edges. This is in contrast to triangular lead samples, which are truncated icosahedra, with slanted edges.[193] However, these shapes only form under certain, not fully understood, conditions. On an electrode

with an approximately 10 mm^2 surface, at most one or two of these triangular platelets were found amongst a large number of rods at settings similar to the ones which were used to grow the rods discussed in the last section.

5.2.1 Sample preparation

The samples were prepared in the same way as the β-tin rods. Fig. 5-6 shows three AFM scans of such triangular platelets. Most triangles were not perfect equilateral triangles such as the one shown in Fig. 5-6a. One edge is slightly rounded, which results in different angles at the corners. In Sec. 2.3.4 it was shown, that the corners play an important role for the surface superconductivity nucleation field. The crystal in Fig. 5-6b has a cut on one side, and the opposite face is not as acute as expected for a triangle, or a perfect "V"-shape. The remaining two corners of the triangle, however, have acute corners with the expected angle for tin. The crystal shown in Fig. 5-6c however, has dimensions close to an equilateral triangle. The main crystallographic facets which are observed during tin growth are illustrated in Fig. 5-6d (*cf.* also Fig. 3-10c for the directions and Fig. 3-9h and n for SEM images) which can form triangular crystals as drawn in Fig. 5-6e. All crystals appear to be relatively flat. The V-shape is probably formed of two rods (such as the one in Fig. 3-9h or n) which are joined at a twin plane (Fig. 5-6e). The plane (10 0 3) is almost perfectly perpendicular to the (101) plane with an error of less then 1°. Untwinned triangles are also possible with one {001}-axis (green colours in Fig. 5-6d and e) along the middle of the triangle. Although the latter are not necessarily twinned, the general morphology of tin, as discussed in Sec. 3.3.1, suggests that the crystals grow from a central spot in all directions and hence twinning and/or a large number of defects are possible along the {001}-axis. In addition, if the two legs of the "V" are not ended with a (101)-face but in a (001)-face, this could also form a triangle, which is not distinguishable from the other configurations. All these triangles have two 61.4° and one 57.2° angle. Without further investigation, the crystal structure of the triangles cannot be determined. However, the "V"-shape indicates that the latter process is possible and that triangles exist with at least two different internal structures. It is later seen that two different behaviours are observed in

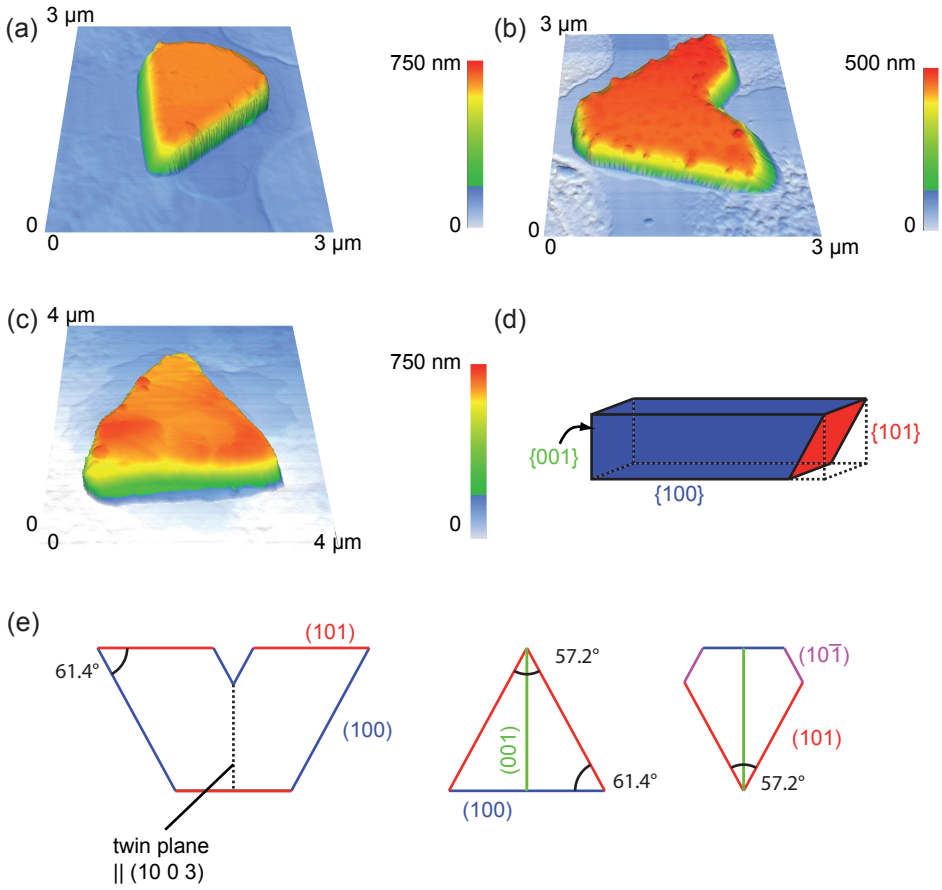

Figure 5-6: AFM images of three different tin samples with an approximate triangular shape. Most samples were triangular platelets as the ones in (a) and (c), while one sample had a cut on one side, forming a "V"-shaped sample (b). The growth directions of a cuboid (d) and possible triangular tin crystals (e) are sketched, where different colours stand for different growth directions.

the triangles, which supports this presumption. Lattice defects are very likely to accumulate along twin planes. The somewhat rough appearance of the top of the crystals in the AFM scans originates mainly from the paraffin wax which was used to glue the crystals to the Hall probe prior to imaging.

5.2.2 Magnetisation data

The magnetisation of triangular samples shows a complex pattern, arising from the formation of intermediate states in the sample. The precise topology and

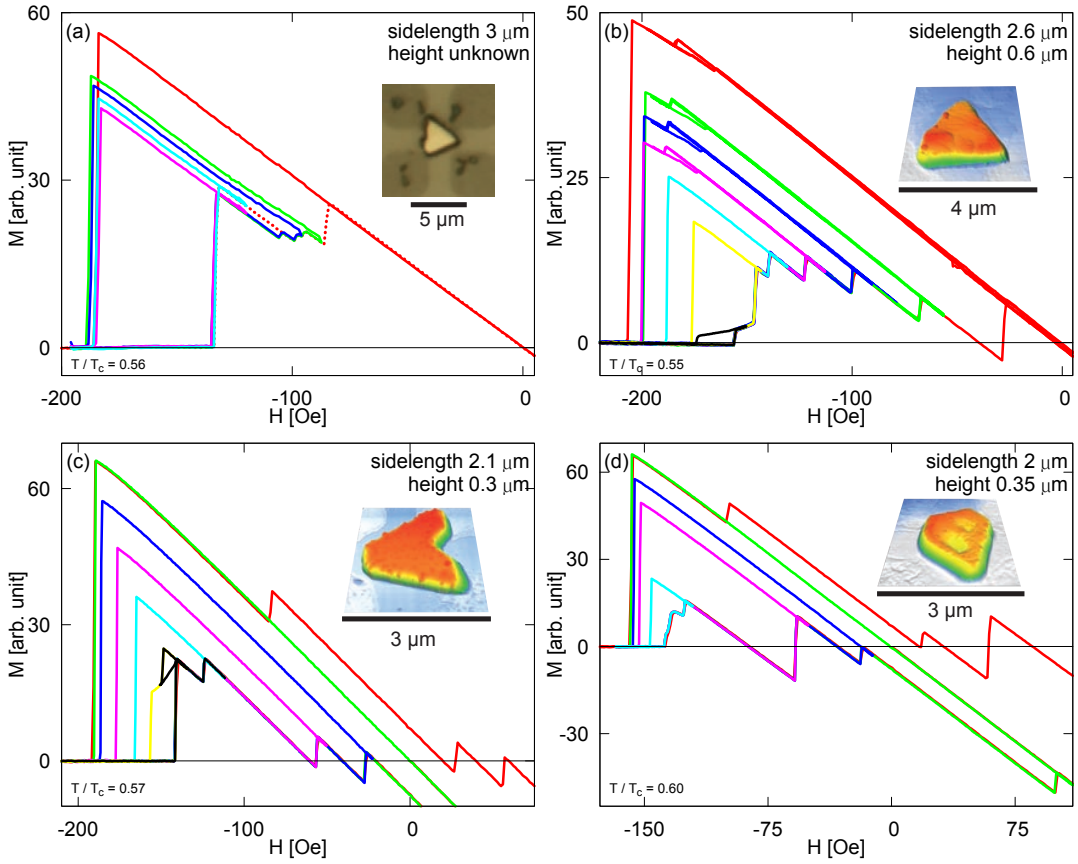

Figure 5-7: Magnetisation data for four different triangular samples at low temperature. The samples display a complex pattern of intermediate states. The data in (a) were recorded using a 2 µm Hall probe, while a 1 µm Hall probe was used for (b)-(d). The insets show an optical image (a) or an AFM image of the sample on the Hall probe ((b)-(d)).

structure of the intermediate state cannot be determined from the experimental data. Moreover some of the triangles display perfect type I behaviour with no evidence of an intermediate state down to the lowest accessible temperatures, while others show an intermediate state at low and intermediate temperatures. This is likely to be caused by defects along twinning planes as discussed above. However, at temperatures close to T_c the magnetisation behaviour of all triangular samples is similar to the tin rods discussed above. Magnetisation data for four different triangles is shown in Fig. 5-7. In addition, consecutive minor loops were recorded where the field was swept from well above H_{sh} until a number of flux quanta had penetrated the sample. At that point, the sweep was stopped and

its direction changed. In this way, the stability of the different flux states can be investigated. These data were measured using a 2 µm Hall probe for the curves in Fig. 5-7a and a 1 µm Hall probe for those in Fig. 5-7b-d. The difference in the data in the two cases is a different areal sensitivity to the formation of normal domains. The area in which the magnetic flux through the sample is measured is approximately four times larger for the 2 µm Hall probes than for the 1 µm Hall probes. It was shown in Sec. 4.1 that for real Hall probes, with slightly rounded corners, the active area is larger than just the central square. An ideal Hall probe with a 1 µm^2 area should record a 20.7 G jump if one flux quantum appears at the centre of the Hall cross. For a Hall probe with rounded corners (*e.g.* with a radius of $b = 0.5$ µm) the jump is much lower,

$$\Delta M = \frac{\Phi_0}{(w + 1.4b)^2} = \frac{20.7 \text{ G}\mu\text{m}^2}{(1 \text{ µm} + 1.4 \cdot 0.5 \text{ µm})^2} \approx 7 \text{ G}. \tag{5.5}$$

This value is larger than the jumps measured in Fig. 5-7 which are about $\Delta M \approx 3.8$ G for the 1 µm HPs and $\Delta M \approx 1.8$ G for the 2 µm HPs. However, as the values in the graph show the measured magnetisation, without the taking into account the effect of the demagnetising factor. Additionally this is just a rough estimate of the value for ΔM and other effects have to be taken into account as well. Flux is measured over the integrated area of the Hall probe and flux which sits off the centre of the sample, will yield a lower signal.

However, the intermediate states do not seem to be solely governed by the sample sizes; defects or small perturbations at the surface seem to facilitate them. Unfortunately we do not have details about the true crystal structure. As described above, the samples are probably not single crystals and the potential twinning plane through the middle of the triangle forms a line of defects which act as possible pinning sites. This internal structure is different for each sample, and hence so is the formation of the intermediate state which is strongly controlled by pinning sites. Nevertheless, the systematics of flux entry in the intermediate state for individual samples is interesting in itself. This process is illustrated in Fig. 5-8, where the magnetisation of the sample in Fig. 5-6c is shown for different temperatures. As the temperature increases, the complexity of the intermediate state changes. As $T \to T_c$, it was shown above that the characteristic supercon-

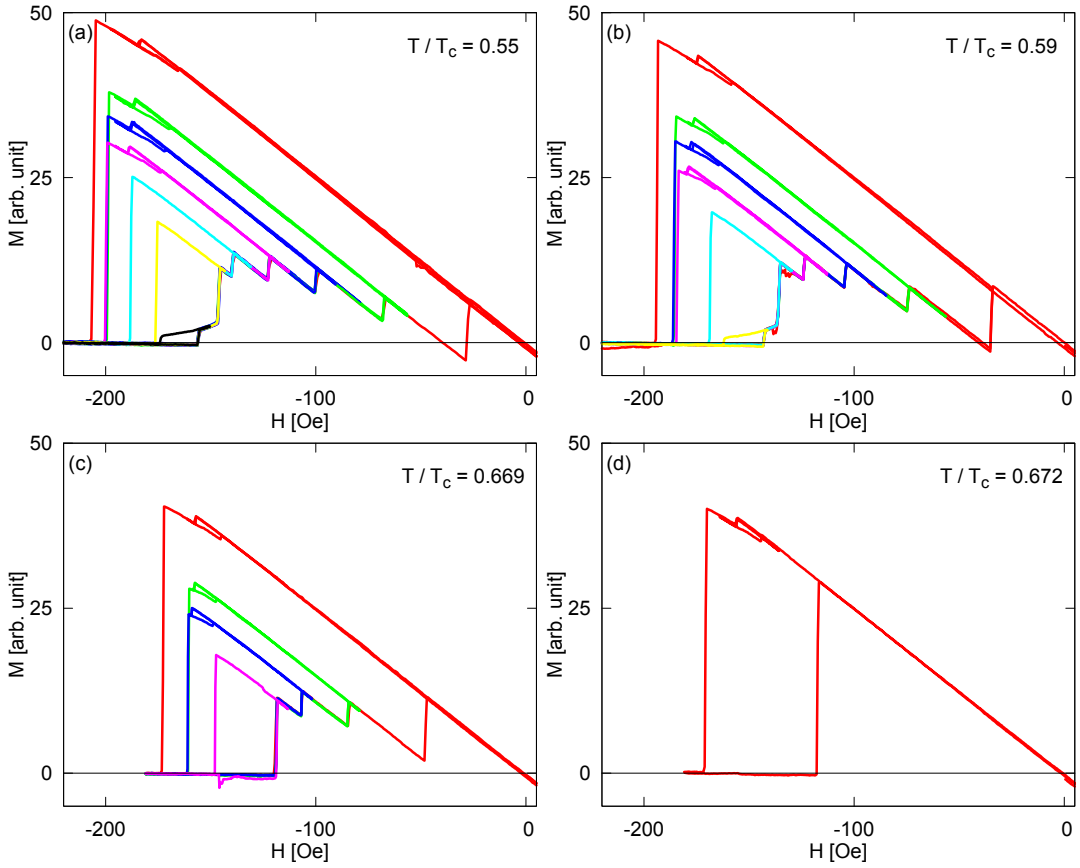

Figure 5-8: The structure of the intermediate state for the triangle shown in Fig. 5-6c and Fig. 5-7b for different temperatures. The number of flux quanta, able to enter separately, decreases with increasing temperature.

ducting length scales increase. In this sample this is reflected in the decreasing amount of flux which can exist inside of the sample. In Fig. 5-8a five stable configurations can be identified. The number of flux quanta penetrating the sample can be labelled by the angular momentum of the order parameter. This is called the vorticity. The states visible in this sample are the Meissner state ($L = 0$, red) where no flux penetrates the sample, as well as states with two ($L = 2$, green), three ($L = 3$, blue), four ($L = 4$, purple), five ($L = 5$, cyan) and six ($L = 6$, yellow) flux quanta within the sample. Surprisingly, the $L = 1$ state, which contains a single flux quantum, is absent. This was observed before in lead triangles and is a subject of current investigations, where it is believed to be a metastable effect related to thermal fluctuations.[193] In an increasing field, before superconductivity is destroyed, normal regions form at a field lower than H_{sh}.

These are represented by the small magnetisation jumps at all temperatures in Fig. 5-8. Flux through one of the corners of the sample, which are far away from the active region of the 1 µm Hall probe are, to a certain extent, hidden from the measurement and hence generate a much smaller change in magnetisation ΔM. However, the corners of a sample are usually the last parts to turn normal in an increasing field. Nevertheless, as these jumps are much smaller than for the single flux quanta which leave the sample as superconductivity is restored in a decreasing field, these are most likely due to one or more corners of the sample turning normal, and forming a metastable state, before the whole sample turns normal. This was only observed in this one sample, and could be caused by a very strong pinning site at one of the corners, possibly the one with the twinning plane through the top of the triangle (*cf.* Fig. 5-6e). With increasing temperature the states with the highest vorticity, L, disappear, until no intermediate state is observed at all above $T/T_c = 0.67$(Fig. 5-8d). The measurements of Fig. 5-8c and Fig. 5-8d are only 10 mK apart and by changing the temperature by this tiny increment it was possible to switch between those two configurations. Apart from the normal domain forming at one corner, at even larger temperatures the sample shows perfect type I behaviour. This is remarkable, as a tiny temperature change is able to suppress the whole intermediate state, including its sub-structure, which is completely restored upon reversing the temperature change.

Simulations for lead triangles, which were performed for M. Engbarth's PhD thesis, used different superconducting parameters, but can nevertheless be compared to the experimental results on tin triangles. Fig. 5-9 reproduces simulations for a 1.8 µm wide and 0.7 µm high triangular lead crystal. The G-L parameter of lead is slightly higher than for tin, but it is still in the type I regime. For the simulation a temperature dependent κ was used with $\kappa(0) = 0.3$ and the temperature was 6.4 K, which corresponds to a reduced temperature of $T/T_c^{\mathrm{Pb}} = 0.89$. The difference between the two simulations in Fig. 5-9 is only the tilt angle of the sides of the sample. Lead crystals, which are truncated icosahedra, have slanted sides, while tin, which is formed by the twinning of slanted rods, has straight vertical sides. The experimental data for a triangle of the exact dimensions and sloped sides, which is shown in blue, matches the appropriate simulation very

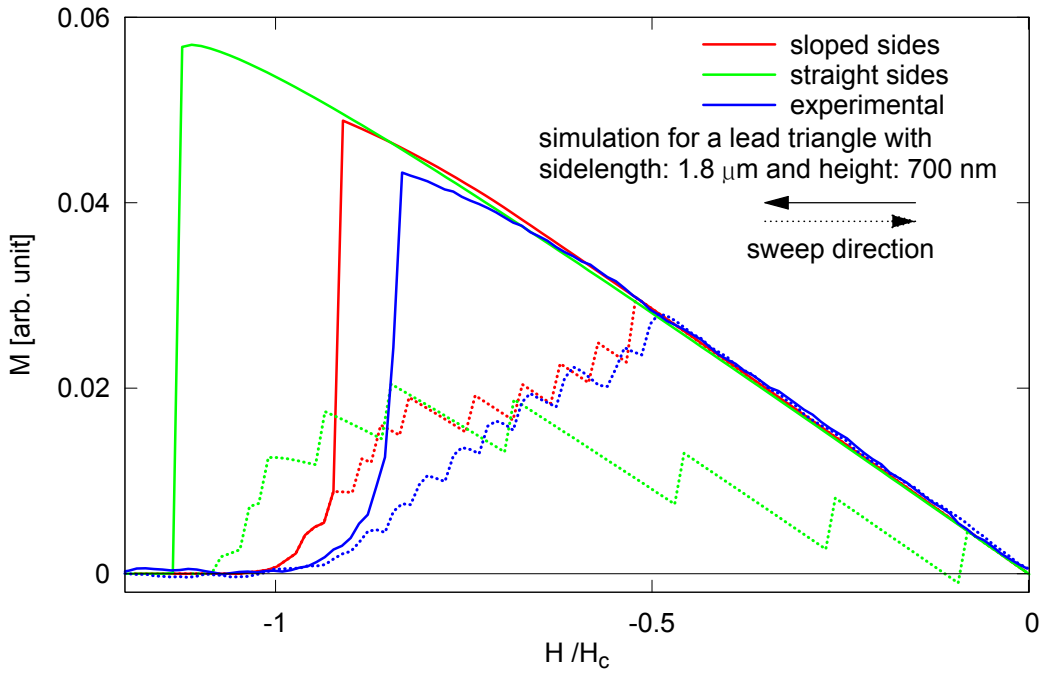

Figure 5-9: G-L simulations for triangular superconducting samples (reproduced from M. Engbarth's doctoral thesis).[193] These simulations use parameters for lead, for which $\kappa = 0.3$ is slightly higher than the value for tin ($\kappa \approx 0.1$). The simulation is for a triangle with 1.8 μm sides and a height of 700 nm at a temperature of 6.4 K ($T/T_c^{\mathrm{Pb}} = 0.89$). Although the simulation parameters are different, the general structure of the intermediate state is very similar to the tin triangles. The measured magnetisation of a lead triangle with exact dimensions and sloped edges is shown for comparison.

well. The graph of the simulation for straight sides exhibits a similar structure of entering flux as seen in the experimental data for a tin triangle (*e.g.* in Fig. 5-8) but at a much lower temperature. It reproduces nicely the entry of single flux quanta in a decreasing field with the onset of the Meissner state at a field very much lower than H_{c3}. In the simulation of the straight edged lead sample, the $L = 1$ state is observed, while it is absent in the intermediate state of the tin triangle shown in Fig. 5-7b. For the lead sample with sloped edges, however, the $L = 1$ state is missing in the simulation as well. However, a comparison of the two triangles of Fig. 5-7b and d reveals that this depends on the individual sample. The mechanism which leads to the formation of the intermediate state and hence the trapping of flux in the tin triangle, however, is governed by defects in the sample. This is qualitatively different from the formation of flux states in

lead, where their configuration is controlled purely by the energy of the states. Nevertheless, the most prominent point, which is illustrated by the comparison of the simulation with the experimental data for tin, is the role played by the edges of the sample and the resulting barrier for the flux to leave the sample. Although the simulation details are different from the actual system, the general shape is very well reproduced.

5.3 Conclusion

Pure β-tin crystals can be grown in a wide variety of shapes and sizes, and are hence an ideal model system for studying mesoscopic type I superconductivity. In tin rods, the full range of mesoscopic behaviours can be followed as the sample dimensions decrease with respect to the superconducting length scales. Two distinct regimes are traversed as first the temperature dependent coherence length and then the penetration depth becomes larger than the sample dimensions and strong quantum confinement occurs. Additionally, the classical irreversible type I first order phase transition between the superconducting and the normal state becomes reversible as the critical temperature is approached. The final change from a first order transition to a second order transition is at the limit of our experimental resolution and is difficult to confirm from the experimental data. However, the crossover from an abrupt magnetisation jump to a more gradual change is well observed in the data for small rods, in which the mesoscopic regime is entered much earlier than for the large samples. In all samples the critical fields at which these transitions occur are observed to be well in excess of the bulk critical field with values up to four times higher at temperatures very close to the critical field, which are experimentally accessible.

Tin can also form triangular platelets, although their formation is not as straightforward as for the tin rods. The formation of a triangular sample can involve the combination of two single crystals and these samples are twinned at one plane. Possibly due to strain and defects in these samples as a result of the twinning, the magnetisation is qualitatively different from sample to sample. A systematic study as was made for the tin rods in Sec. 5.1, or by M. Engbarth for lead

triangles[193] is hence not possible for these samples. However, an intermediate state is observed in some of the samples at low temperatures, which appears similar to the intermediate state in triangular samples of other materials, *e.g.* lead, which have been studied before. In the intermediate state a small number of flux quanta are trapped in the sample which leave the sample one by one as the field is decreased. The stability of different configurations as a function of the number of flux quanta contained is investigated via their minor magnetisation loops. Simulations of the intermediate state, and how this is affected by the shape of the edges of the sample, which were originally performed for lead samples, show a very good agreement with the observed structure of the intermediate state in tin. Although lead and tin are quite different in their superconducting properties, the effect of the edges is well confirmed by the data shown. The missing $L = 1$ vorticity state as observed in certain samples in this work, has been observed before and it is still not fully understood what circumstances lead to its absence. For one triangular sample, normal domains formed at a corner of the sample in an increasing field, which is very unusual but could possibly be explained by the complex internal structure of the sample and strong pinning sites at locations of the crystal where twinning occurs. For all samples, the intermediate state is suppressed as the temperature approaches T_c when ideal type I behaviour is observed in all samples.

Chapter 6

Sn-Pb core-shell structures

The pure β-tin crystals, discussed in the last section, can be plated with lead to form unique S-S' core-shell structures where two different superconducting materials are combined. The preparation of Sn-Pb core-shell structures, and micromagnetic measurements on these, are discussed in the following section.

The combination of a tin core (T_c = 3.72 K and $H_c(0)$ = 303 Oe in the bulk) with a lead shell (T_c = 7.19 K and $H_c(0)$ = 804 Oe in the bulk) yields a system of two type I superconductors in intimate contact. In the actual samples, the thin lead film can behave as a type I or type II superconductor, depending on the thickness.[89] In thin lead films, the effective penetration depth increases due to the decreasing mean free path of the charge carriers in the disordered and polycrystalline shell. If the effective G-L parameter becomes larger than $1/\sqrt{2}$, the material is of type II, easily allowing the penetration of single flux lines. As a rule of thumb the mean free path l of the charge carriers in a thin film, is comparable to the thickness of the film t.[219] Both the effective penetration depth $\lambda_{eff}(T)$ and the coherence length $\xi(T)$ are a function of the mean free path l.[34,35,220] As shown first by Miller (effective penetration depth) and discussed later by de Gennes and Tinkham (effective coherence length), the G-L parameter in a moderately dirty superconductor, such as the thin, polycrystalline lead film

in this work, can be approximated by

$$\kappa(0) = \frac{\lambda_{eff}(0)}{\xi(0)} \approx \frac{\lambda_L(0)\sqrt{1+\xi_0/t}}{0.855\sqrt{\xi_0 t}}, \tag{6.1}$$

where we have assumed $l \approx t$. This equation yields $\kappa(0) = 1/\sqrt{2}$ for the critical thickness of $t_c \approx 90$ nm, using $\lambda_L(0) = 37$ nm and $\xi_0 = 83$ nm. This value is also confirmed experimentally by Cody *et al.* to be of the order of $t_c \approx 50 - 100$ nm for lead at temperatures of ≈ 4.2 K.[89] As κ increases with decreasing thickness of the lead film, the critical field up to which superconductivity survives, $H_{c2} = \sqrt{2}\kappa H_c$, also increases. However, for thick films, $t > t_c$, the shell will be type I and the critical field H_c depends only very weakly on the film thickness. In all cases, the lead shell is superconducting at temperatures and fields much higher than the core. This leads to a boundary condition at the surface of the core, where the surface extrapolation length for the order parameter, b, is negative. This case was discussed in Sec. 2.4, where the order parameter in the core is enhanced at the surface due to intimate contact with the "stronger" superconductor. Baelus *et al.* showed theoretically, that this can lead to an enhancement of the core superconductivity in the form of increased critical temperature and critical field.[108] Experimentally, the electroplating of the tin core on all exposed faces, *i.e.* on five sides for cuboid shaped samples, is much more "complete" than in other experiments where two superconducting materials have been combined in the form of bi- or multilayers.[221–223] To the best of our knowledge, this is the first investigation of the proximity effect in such three dimensional samples. With micromagnetic measuremenents, the enhancement of T_c can be easily measured by identifying the core contribution to the net magnetisation. In addition, the extent of the proximity effect, *i.e.* how deep superconductivity penetrates the normal core when the shell is superconducting, can be estimated from variations in the net shell magnetisation at high temperatures.

6.1 Sample preparation

The samples which were used for these experiments were prepared as discussed in Sec. 3.3.1 (cores) and Sec. 3.3.2 (shells). We exploited the fact that the deposition potential of lead is slightly higher than the deposition potential of tin, allowing us to deposit these materials separately. The tin cores were grown at low overpotentials as described above. To grow the lead shell, the tin-electrolyte was removed and quickly replaced with the lead-electrolyte. The overpotential for plating was chosen to be ≈ 10 mV higher than the overpotential for the core deposition. Too low a potential resulted in the stripping of the tin crystals, while a much higher potential resulted in large amounts of lead deposited on the electrode. As can be seen in Fig. 3-13a and b, under optimal conditions no lead is deposited anywhere else on the HOPG. The deposition potential was kept constant while the deposited charge was recorded. The deposition was stopped manually when a pre-defined charge, and hence a certain amount of material, was deposited. For most of the crystals a ratio $Q_{\mathrm{Sn}}/Q_{\mathrm{Pb}} \approx 2/1 - 1/1$ was aimed for. The resulting shells were of the order of 50-400 nm thick for small tin crystals, according to the estimation made in Sec. 3.3.2, depending on the actual size of the crystal.

The positioning of the samples on the Hall probes was discussed before. Although the Pb-covered faces are rougher than the clean Sn-surface as seen from SEM images, this difference is not visible under an optical microscope or in an AFM scan after the crystals were immersed in the wax. Hence, it is not known exactly where the uncovered surface lies with respect to the plane of the Hall probe.

6.2 Magnetisation data

The magnetisation data were recorded as discussed above. However, the geometry of the core-shell structures results in a different appearance of the data as compared to pure tin crystals. In the latter case, the crystal covers the whole active area of the Hall probe and the measured magnetic flux through the Hall sensor is the flux close to the surface of the crystal and hence a direct measure of the magnetisation of the crystal. In the case of a superconductor, this magnetisation

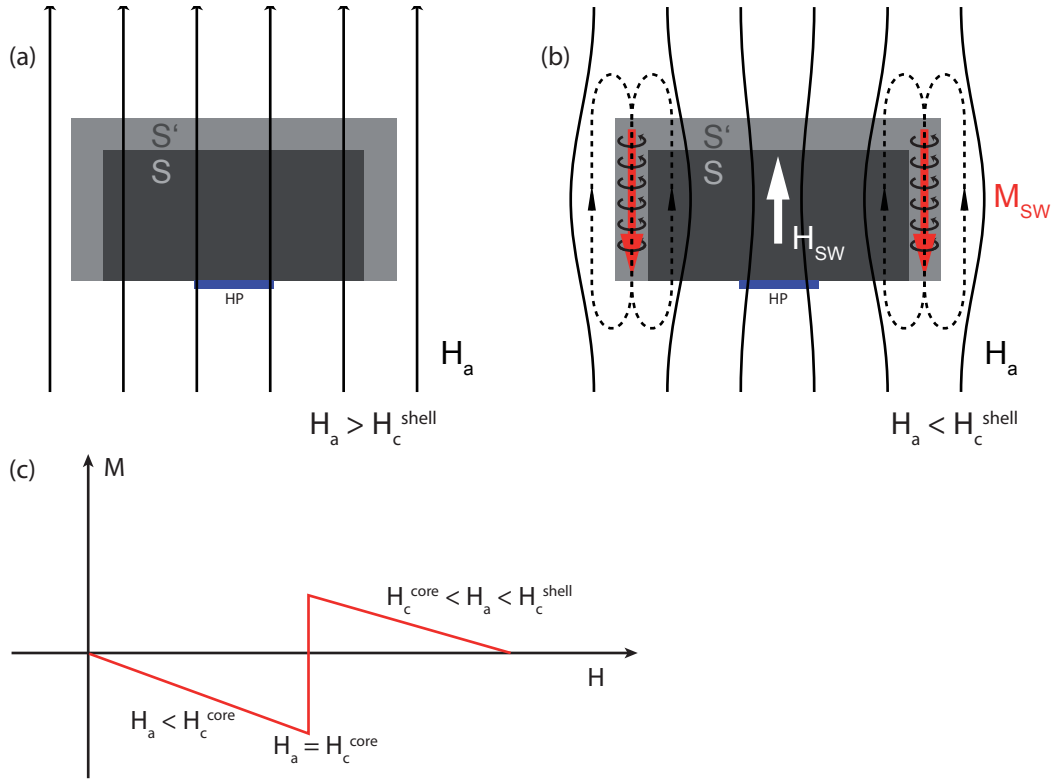

Figure 6-1: The geometry of the core magnetisation and the external field in a S-S' core-shell structure for $H_a > H_c^{\text{shell}}$ (a) and $H_c^{\text{core}} < H_a < H_c^{\text{shell}}$ (b) and the resulting measured magnetisation curve (c) for a negative sweep (*cf.* experimental data in Fig. 6-2c).

is diamagnetic and opposes the externally applied field. Some core-shell samples are larger than the Hall probes and hence for these crystals the shell is at some distance from the active sensor area. This is illustrated in Fig. 6-1a. If, however, an applied field H_a is reduced below the shell critical field H_c^{shell}, the shell walls become superconducting and magnetic flux is pushed towards the centre of the sample as illustrated in Fig. 6-1b. For a centrally placed sample, this results in a magnetisation curve as drawn in Fig. 6-1c. For a field $H_c^{\text{core}} < H_a < H_c^{\text{shell}}$ where only the shell is superconducting, the flux through the Hall probe is increased by the expelled field which is pushed towards the Hall probe. In this case, although the magnetisation of the shell walls, M_{SW}, opposes the external field, the shell wall stray field, H_{SW}, points in the same direction as the applied field, H_a. Only when the core becomes superconducting, as $H_a < H_c^{\text{core}}$, does the measured net magnetisation oppose the external field, as now almost the whole sample becomes

diamagnetic. However, at the interface between core and shell we expect flux to become trapped. If, however, the sample is not perfectly centrally positioned, or if the sample is small compared to the Hall probe area, this effect can be less pronounced.

The lead on top of the shell, which is perpendicular to the applied field, can be neglected here. In the polycrystalline lead film, increased scattering at the grain boundaries and the surface yields a decrease in the carrier mean free path, which enhances the effective penetration depth. A thin shell exhibits type II behaviour if the effective G-L parameter increases above $1/\sqrt{2}$ and the interaction between flux lines becomes repulsive.[224] Hence type II behaviour is expected in thin films on top of the shell with $d < 90$ nm. Demagnetising effects, as discussed in Sec. 2.3.1, play an important role in both type I and type II regimes and yield a very low penetration field, H_p or H_{c1}, for the top of the shell. Hence diamagnetism due to the Meissner state is mainly restricted to the side walls, which are oriented parallel to the applied field. The demagnetising factor for this geometry is much smaller (*cf.* Sec. 2.3.1). Flux is hence mainly screened out of the side walls, but can still penetrate through them and move into the thin top film. The fabricated shell thicknesses probably cover both, type I and type II, regimes, and hence qualitatively different phenomena are expected in different limits.

Another important change in the magnetisation behaviour of the shell in the two regimes is the critical field up to which superconductivity exists. In the case of a thick film, the critical field for the destruction of superconductivity is defined by the bulk critical field extended by possible superheating effects as expected for type I superconductors. In very thin films, the G-L parameter increases as well as the critical field $H_{c2} = \sqrt{2}\kappa H_c$ (*cf.* Sec. 2.2.6). Deep in the type II limit for thin films, when $H_{c2} \gg H_c$, superconductivity in the shell is maintained at much larger fields than for thick films.

Fig. 6-2 shows a compilation of magnetisation curves for different core-shell structures at the lowest achievable temperature in our experimental set-up ($T \approx 2$ K). The deposition ratio for the crystals was between $Q_{\mathrm{Sn}}/Q_{\mathrm{Pb}} \approx 3/2$ for (a) and $Q_{\mathrm{Sn}}/Q_{\mathrm{Pb}} \approx 2/1$ for (c) and (d). The shell thickness t as calculated by Eq. (3.8) is labelled in the graphs. For a large crystal with a thick shell in Fig. 6-2a, the mea-

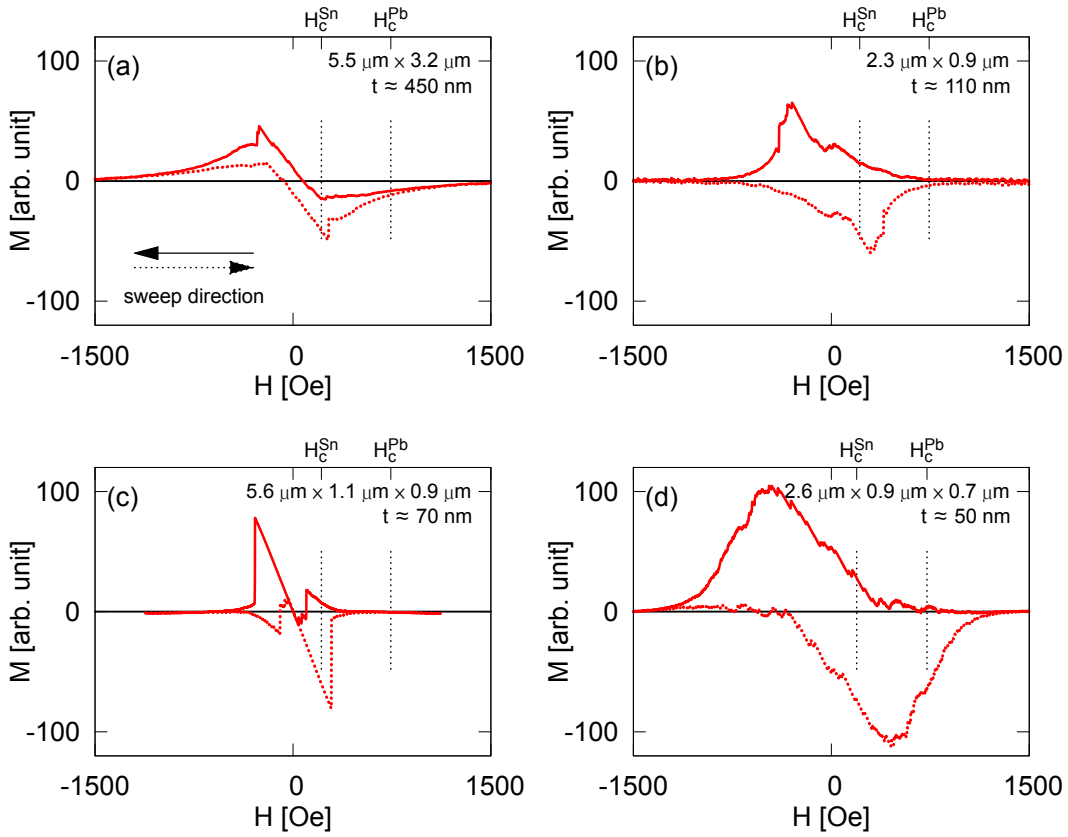

Figure 6-2: Magnetisation curves for various Sn-Pb core-shell samples at low temperature, $T \approx 2$ K. The samples are different sized rods. The core dimensions are given in length × width × height (if known) as well as the estimated shell thickness t. The bulk critical fields of lead and tin are marked on the positive H-axis. The superposition of core and shell magnetisation lead to very different, not yet fully understood, magnetic behaviour of the individual samples.

sured magnetisation is generated by both, core and shell, in roughly equal parts. A signature of the core is seen as the Meissner state in it is destroyed and the core turns normal in one large jump. This is also the case for smaller crystals with a slightly thinner shell (Fig. 6-2b). The shell is here clearly in the limit of $t \gg \lambda_{eff}$ and hence exhibits an intermediate state, as expected for a type I material. The large demagnetising factor of the top and the low demagnetising factor of the side walls gives rise to a complicated magnetisation behaviour. This changes for thinner shells, where type II behaviour is expected. With decreasing shell thickness, the core contribution to the measured magnetisation first becomes much more prominent as can be seen from the graph in Fig. 6-2c. A rather different

behaviour is seen in Fig. 6-2d, where a small core is plated with an even thinner shell. In contrast to the three samples discussed before, the shell is now thin enough to be well in the type II limit. This is reflected in the strongly enhanced critical field of the shell in the type II regime and much stronger vortex pinning (*i.e.* remanent magnetisation). The core magnetisation is completely hidden here by the shell magnetisation, or possibly suppressed by it. From the magnetisation data shown here, this cannot be unambiguously determined.

If the dimensions of core and shell are chosen carefully, the crystals show a sharp step in magnetisation when superconductivity in the core is destroyed. This transition is easy to distinguish at low temperatures. However, at higher temperatures, when the critical temperature of the core is approached, superconductivity in the core and hence diamagnetism in the core only occurs at very small applied fields and is easily concealed by the magnetisation of the shell. To overcome this problem and to get a strong signal from the core, one sample with a large core and a thin shell (core: $11.9 \times 3.2 \times 3.1$ µm^3, 40 nm shell) was prepared to measure the effect of the shell on the core which is discussed in the next section (Fig. 6-3.

To confirm the enhancement of the core compared to a "bare" tin crystal, one pure tin crystal of comparable dimensions was measured alongside the core shell crystals. To assist with the measurement of the T_c enhancement of the core, three lock-in amplifiers were used to record the signal of the core-shell structure, a "bare" tin rod and an empty Hall probe simultaneously. Even if there is an absolute error in temperature and/or magnetic field, this technique allows one to directly compare the values with confidence.

6.2.1 Enhancement of the core T_c

One of the effects which the shell has on the core is an enhancement of the critical temperature of the core due to proximity-induced superconductivity. Here, the tin core is the "weak" superconductor, while the shell is much stronger and has a higher T_c and $H_c(T)$ at a given temperature. The enhancement of the order parameter at the interface gives rise to an enhancement of the critical parameters of the core. For $T_c^{\text{core}} < T < T_c^{\text{shell}}$ and $H_c^{\text{core}} < H_a < H_c^{\text{shell}}$ the isolated core

is in the normal state, when Cooper pairs cannot form. The shell, however, is superconducting and hence acts as a source for Cooper pairs which can diffuse across the interface and into the core. This was theoretically demonstrated by Baelus *et al.*.[108] Fig. 6-3 shows magnetisation curves for a large Sn-Pb core-shell with a comparatively thin shell. The tin core has the dimensions $11.9 \times 3.2 \times 3.1$ µm^3, and is surrounded by an approximately 40 nm thick lead shell. A similar sized "bare" tin rod ($13.5 \times 3.3 \times 2.4$ µm^3) was measured simultaneously. Data are shown for three different temperatures close to bulk T_c^{Sn}. The red curve was recorded below the critical temperature of tin. The magnetisation curve for the tin rod is shown, offset by -10 G on the magnetisation axis, in the same colour. It is evident, that the critical field of the core is greatly enhanced for both "superheating" and "supercooling" branches. Although, in the core-shell the core would not technically be superheated or supercooled, this notation for the fields of the destruction and onset of superconductivity is retained in this section. If the temperature is raised above the critical temperature of bulk tin, the Hall probe under the bare tin rod does not detect any magnetisation signal. In the core-shell structure, however, the sharp transition of the core is still visible. Further, the slope of the $M(H)$ curve in the core superconducting state has a similar slope below and above the critical temperature, suggesting, that a similar amount of the core is superconducting above T_c^{Sn}. Assuming that the whole core is superconducting below the critical temperature, this means that the whole core, and not just a surface sheath close to the shell, is still superconducting at $T > T_c^{\mathrm{Sn}}$. In Fig. 6-4 the critical fields of the onset and destruction of superconductivity in the core are shown as a function of temperature. Both values are greatly enhanced compared to the values for the pure tin rod. It is notable that the reference tin rod does not show any superheating, in fact superconductivity is destroyed even below $H_c(t)$. This is probably due to the large size of these crystals; only the central part of the rod is measured by the Hall probe and the sample exhibits an intermediate state, as evidenced by magnetisation jumps at low temperatures in an increasing field. Hence superconducting domains at the corners, which are about 5 µm away from the Hall probe, are hidden from our measurement. Close to the critical temperature, this effect is not observed.

In the core-shell structure, the supercooling field of the core, H_{sc}, at which super-

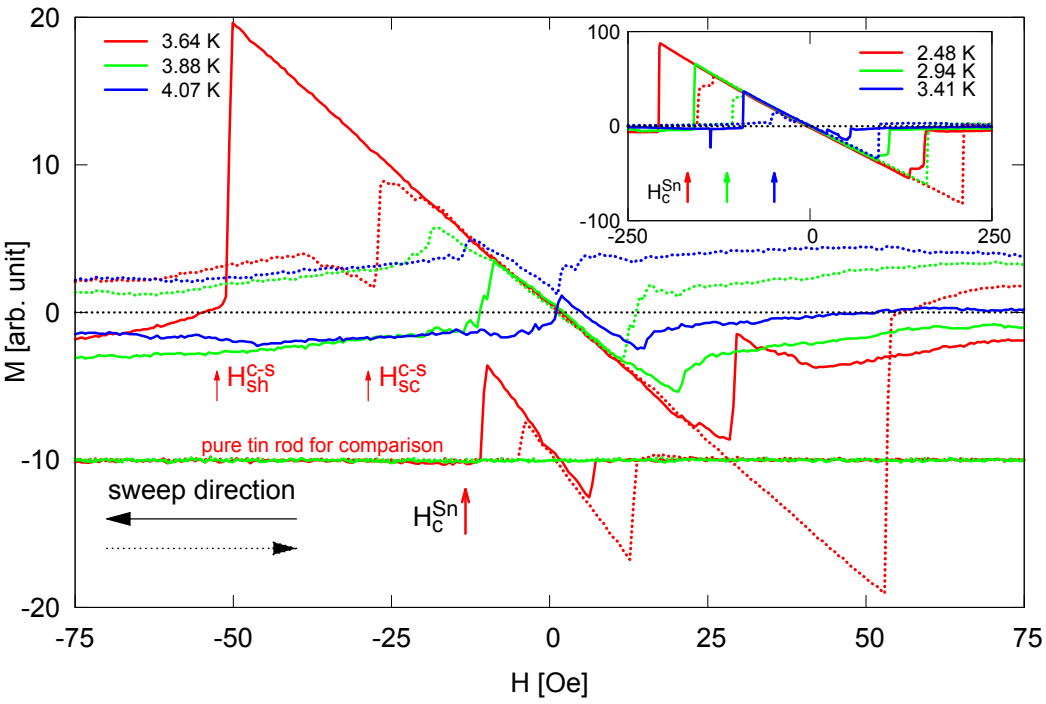

Figure 6-3: Magnetisation curves for a large Sn-Pb core-shell sample (core: $11.9 \times 3.2 \times 3.1$ µm^3, shell: ≈ 40 nm) and a Sn rod ($13.5 \times 3.3 \times 2.4$ µm^3) measured simultaneously for $T \approx T_c^{\mathrm{Sn}}$ which confirm the enhancement of T_c in the core. The inset shows magnetisation curves at lower temperature, when the shell is practically invisible in the magnetisation. The maximum fields of the sweep start and end point were chosen so that no shell magnetisation was detected at these fields. It was $|H_{max}| = 500$ G for the three corves close to T_c^{Sn}. The data in the inset was recorded with $|H_{max}| = 2000$ G. Two arrows mark the fields plotted in Fig. 6-4

conductivity nucleates in the core, has a similar temperature dependence to H_{sc} of the tin rod at low temperatures. When the critical temperature of bulk tin is reached this behaviour changes, and this critical field approaches zero much more gradually than before. The superheating field on the other hand approaches zero and has a value very close to zero at the highest temperatures where a core transition could be unambiguously identified. The values in the graph abruptly stop at $T \approx 4.3$ K. This is where the signature of the core almost completely vanished into the background shell magnetisation. The superconductivity in the core is probably still there, but is not detectable in our experiment. It is not possible to estimate the actual critical temperature of the core from the data presented, only a lower limit can be estimated of $T_c^{\mathrm{core}} > 4.3$ K $= 1.16\ T_c^{\mathrm{Sn}}$.

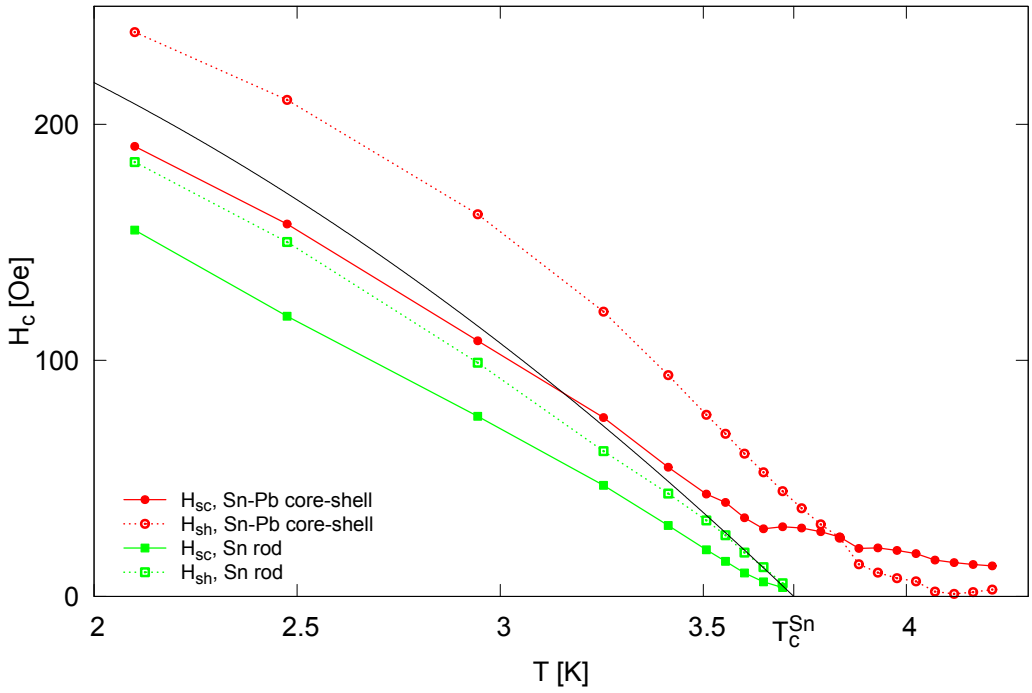

Figure 6-4: The critical field of the onset (H_{sc}) and destruction (H_{sh}) of superconductivity in the S-S' core and in the tin rod as a function of temperature.

It is interesting to note that superconductivity is restored in the core, in a decreasing field, even above the critical temperature of the core, while superconductivity is destroyed upon further sweeping to a reversed field with a *lower* absolute value above a certain temperature. The polycrystalline thin lead film that forms the shell is clearly in the type II limit in this sample and hence never exhibits a full Meissner state in a decreasing magnetic field, but contains vortices which are usually aligned parallel to the applied field. As the core stays in the Meissner state all the way to zero applied field, the trapped flux is still oriented in the same way, even after the sign of the applied field changed. An explanation for the missing Meissner state after the applied field changed its direction might lie in the configuration of the trapped flux. The flux that stays in the lead shell is pushed into the centre of the sample, as the shell walls become more superconducting in a decreasing applied field. When the critical field falls below the critical field of the core, the flux will be trapped at the interface between the tin core and the lead shell. The supercurrents in the core, generated by the flux along its perimeter have a particular direction of rotation. After changing the

direction of the applied field, additional currents are necessary to keep the core field free. Apparently, as soon as these currents start to form, superconductivity in the whole volume of the core is destroyed. This could be due to the fact, that at this temperature the core is only superconducting if Cooper pairs are provided by the shell which then sustain the proximity induced supercurrents in the core. However, it is not known exactly where magnetic flux is trapped in the sample and how this affects core superconductivity. Field cancellation effects of the shell magnetisation and the applied field might also play a role, but without knowledge of the magnetic flux in the sample, these cannot be unambiguously determined. It is hence not currently possible to explain all the observed effects by existing theoretical models.

6.2.2 Little-Parks oscillations in the shell

The measurement of oscillations of the net magnetisation at high temperatures required a very low sweep speed and a high applied field resolution. The ratio between field steps and maximum applied field is limited by the digital resolution of the power supply. All measurements hence represent a trade-off between the maximum applied field and the resolution. As a result, resolving these oscillations in magnetisation data is not possible at high fields, *i.e.*, for very low temperatures.

Little and Parks showed in their classic experiment that an oscillation of T_c of a cylindrical superconducting shell is observed, when H is varied.[40,41] Upon increasing the field, the temperature dependent resistance of the cylinder changed periodically and the periodicity of these so called Little-Parks oscillations is connected with the flux quantum Φ_0 and is a direct measure of the internal area A of the normal cross-section. The periodicity in an applied magnetic field is

$$\Delta H = \frac{\Phi_0}{A}. \tag{6.2}$$

Similar oscillations are observed in the core-shell structures in this work. In particular, at high temperatures the magnetisation data exhibits a periodic behaviour which is illustrated by the data in Fig. 6-5. In the original Little-Parks experiment the oscillations were observed in a perfect "ring", with the interior

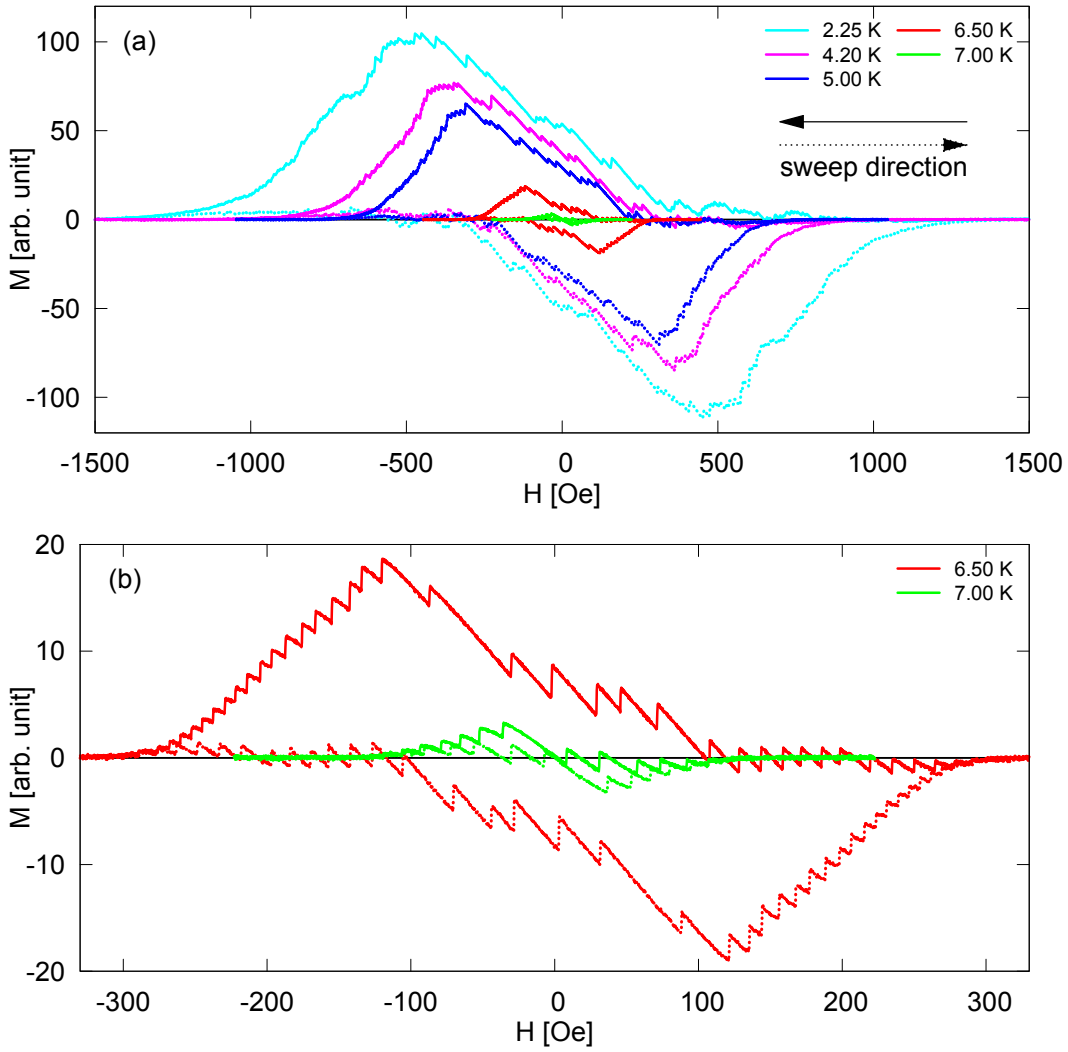

Figure 6-5: Magnetisation curves for a small Sn-Pb core-shell (core: $2.6 \times 0.9 \times 0.7$ µm^3, shell: 50 nm) at various temperatures (a). Oscillatory behaviour is most prominent at high temperatures as seen in the expanded graph in (b).

filled by an insulator. In the core-shell structures of this work, the loop is formed of the four side walls perpendicular to the plane of the Hall probe sensor. The area surrounded by this frame (defined by the core) is simply $A = l \cdot w$. The top lead film, perpendicular to the applied magnetic field, is ignored in this approximation for the reasons described above. As the shell is not filled with an insulator, but with another superconductor, the oscillations give a measure of how deep superconductivity spreads from the shell into the core. Fig. 6-5 shows

magnetisation curves recorded at different temperatures for one small core-shell structure. For this analysis a small crystal is necessary as, from Eq. 6.2, it is clear that a smaller area yields a larger step size, ΔH, which is needed to be able to resolve the oscillations. The crystal measured here has a core of $2.6 \times 0.9 \times 0.7$ µm^3 and a shell of $\approx$ 50 nm. At low temperatures ($T \leq T_c^{\text{core}}$) the magnetisation steps follow no clear resolvable pattern due to strong diamagnetism and vortex pinning in the shell. Only for temperatures well above T_c^{core}, *e.g.* 6.5 K, is a clear oscillatory pattern visible. For the two highest temperatures, the position and height of these jumps is recorded in Fig. 6-6. The top panel shows the magnetisation curves for 6.5 K and 7 K which clearly show a large number of steps which can be interpreted as Little-Parks like oscillations associated with closed superconducting loops around the perimeter of the crystal. From Fig. 6-5 it is clear that the steps occur for both sweep directions in a mirror inverted manner. The plots of ΔH and ΔM (Fig. 6-6b) show the values for both sweep directions. The data from the second sweep was mirror inverted to match the data of the first sweep, which is shown above in Fig. 6-6a. These plots convincingly confirm the reproducibility of the observed features.

The periodicity of the jumps expected for a lead shell with an empty core,

$$\Delta H_0 = \frac{\Phi_0}{A} = \frac{20.7 \text{ G} \cdot \text{µm}^2}{2.6\text{µm} \times 0.9\text{µm}} = 8.8 \text{ G}, \tag{6.3}$$

is marked as a dotted line in the ΔH plot in Fig. 6-6b. This value is only reached for the last jumps at large negative decreasing applied fields and *vice versa*. At both temperatures a slow approach of ΔH to this value is visible as the magnitude of the field is increased. The higher value of ΔH corresponds to a smaller flux containing area. This indicates, that superconductivity exists, to a certain extent, in the core as well. Assuming a thickness t for the superconducting sheath, so that the surrounded area becomes $A = (l - 2t)(w - 2t)$, with the core dimensions width, w, and length, l. The parameter t can be calculated from the magnetisation jumps ΔH. This is shown in the bottom panel of Fig. 6-6. The value $t = 0$ corresponds to the current flowing exactly around the perimeter of the core. The data show clearly, that at low fields, superconductivity is able to penetrate deep into the core while, for increasing fields, superconductivity is

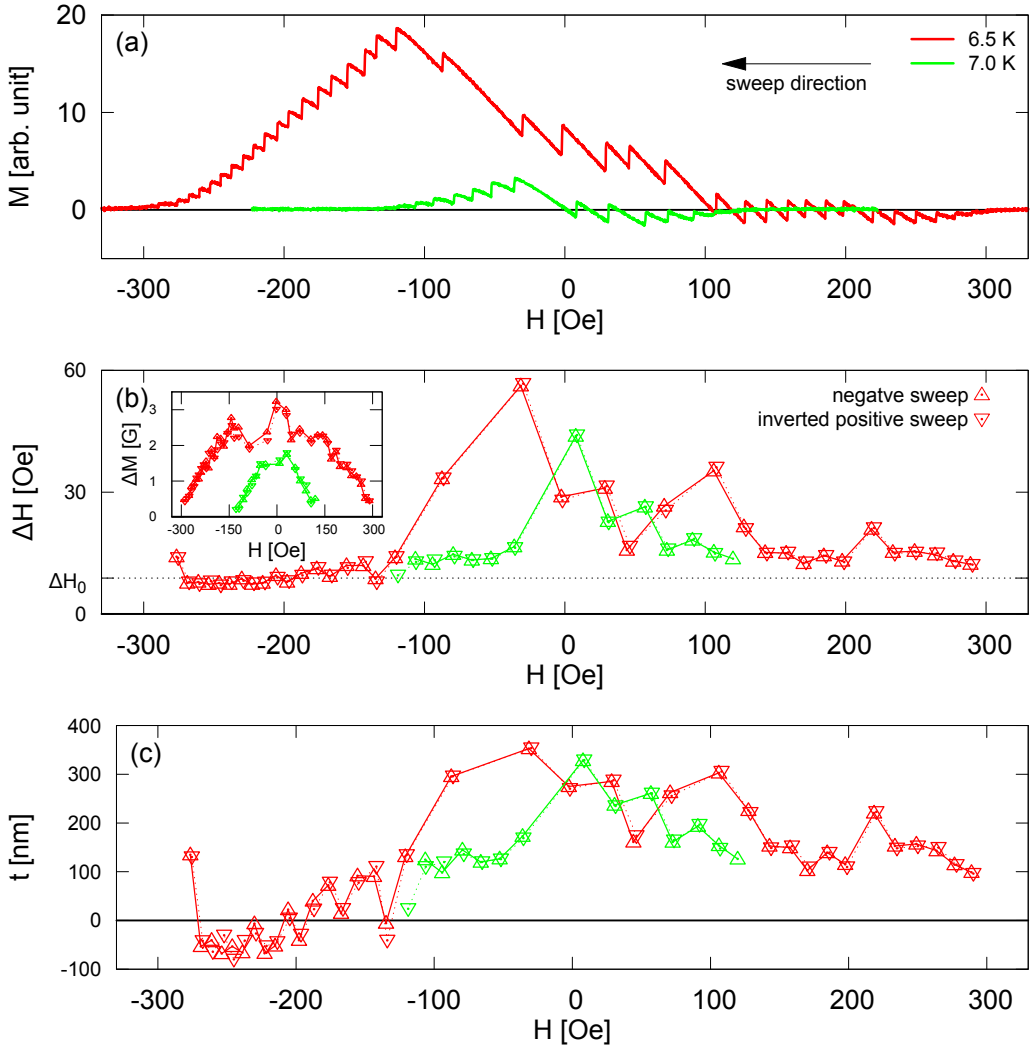

Figure 6-6: A close analysis of the magnetisation jumps, (a), reveals that the effective area surrounded by superconductivity changes with temperature and applied field. The data for ΔH, (b), and ΔM (inset) are plotted for both sweep directions, with the data of the positive sweep direction mirror inverted to fit the magnetisation data for the negative sweep shown on top (*cf.* Fig. 4-8). ΔH_0 is the step size corresponding to the perimeter of the core. The thickness of the superconducting sheath t as derived from ΔH is shown in (c).

increasingly restricted to the shell. The complex pattern at low applied fields, however, suggests a sheath of induced superconductivity in the core but is not fully understood.

The data could also be complicated by the formation of an intermediate state in

the tin core, which is able to form at fields and temperatures above the critical parameters of bulk tin. Further experiments will be required to fully understand this.

6.3 Conclusion

We show that it is possible to grow high quality 3D S-S' core-shell structures with tin cores and lead shells by electrodeposition. The lead shell can be grown on any tin shape, and appears to be a fairly rough polycrystalline film in SEM images. The lead shell coats all exposed faces of the crystal, only the face where the crystal is attached to the electrode is usually uncoated, yielding almost fully covered 3D core-shell structures. Alloying of the tin and lead is not observed within the resolution of the analysis methods used.

The lead shell is able to enhance the critical field and critical temperature of the core considerably. One experimental problem is that the signature of the core in the measured magnetisation is obscured if the shell magnetisation becomes too strong compared to the core magnetisation. Nevertheless, a qualitative analysis is possible and indicates an increase of the critical temperature of the tin core by at least 15 % in a large tin rod with a thin lead shell. At high temperatures, the onset of superconductivity in the core on decreasing the field occurs at higher fields than its destruction on increasing the field after reversing its sign. Upon increasing temperature, the critical field where superconductivity is destroyed approaches zero field while the onset field remains finite. This unexpected behaviour is not explained by existing theoretical models.

At high temperatures, when the core is not completely superconducting, oscillatory behaviour of the magnetisation as a function of applied field is observed. The jumps in magnetisation can be interpreted as the entry/exit of single flux quanta by analogy with Little-Parks oscillations. Changes in the field dependent periodicity of flux entry suggest that even at temperatures $T \gg T_c^{\mathrm{core}}$ superconductivity enters the core in a sheath around the perimeter, where the core is in close contact with the shell. The thickness of this sheath depends on the mag-

netisation history of the sample. As one would expect, superconductivity enters deeper into the sample at low fields than at high fields.

One major challenge for the analysis of these crystals is distinguishing between core and shell magnetisation as measured by the micro Hall probe technique. It is not possible to unambiguously distinguish the contributions of the core and the shell to the net measured magnetisation. Although the critical temperatures of tin and lead are very different, the superconducting properties of the lead shell change considerably at temperatures close to the critical temperature of tin, so that it is not possible to record a "shell background" by switching the core to the normal state by raising the temperature. Hence the interpretation of data from such core-shell structures is challenging. In the future, 3D G-L simulations are planned in collaboration with M. Milošević in Antwerp, who has indicated a strong interest in the experimental results. These should provide strong insights into the underlying physics of these fascinating systems.

Chapter 7

Sn/Pb-Ni core-shell structures

In the following section, the preparation of, and experiments on, core-shell structures with a superconducting core and a ferromagnetic shell are discussed. Most experiments on superconductor-ferromagnet hybrids (FSH) have been performed on lithographically prepared samples, which are generally constrained to be two dimensional. The electrochemical fabrication technique used for the preparation of our samples allows three dimensional structures to be made. While for lithographically fabricated samples or layered structures the ferromagnetic material is produced on just one side of the sample, electrodeposition of the ferromagnetic material results in coverage on all exposed faces of the crystal. Applications of such 3D samples range from magnetic guidance devices to novel superconducting/magnetic memory devices (*cf.* Sec. 2.5.3). In addition, lithographic fabrication of such devices is slow and expensive compared to electrodeposition, which allows a very large number of almost identical samples to be produced simultaneously.

The main focus of the following experiments is on exploring the interaction of the stray field of the ferromagnetic shell with the diamagnetic superconducting core. The competition of these two oppositely directed magnetisations in an externally applied field leads to repeated reversible switching of the net magnetisation behaviour.

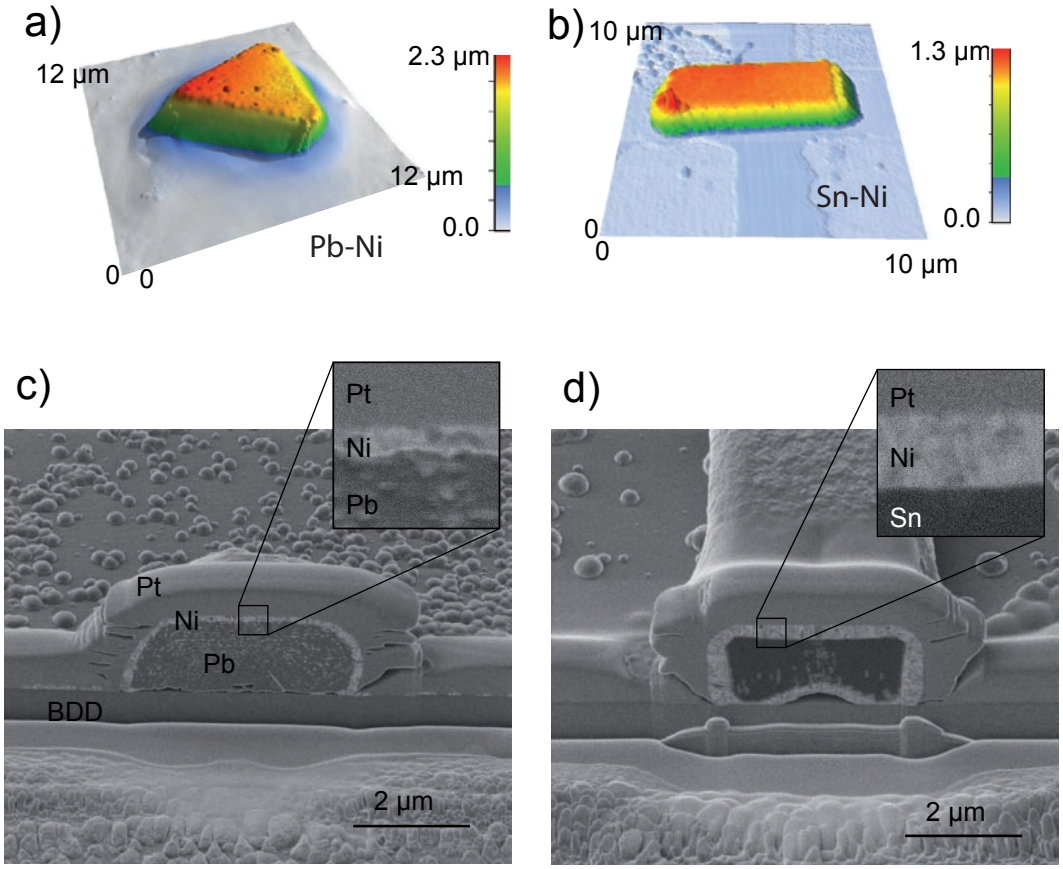

Figure 7-1: (a) and (b) show two AFM images of two core-shell structures, one Pb-Ni triangle (a) and one Sn-Ni rod (b). (c) and (d) show FIB milled cross sections of similar samples used to determine the shell thickness.[136] The material on the top of the crystals is Platinum, which was deposited to protect the actual crystal from damage during the milling process.

The experimental results are compared to micromagnetic simulations, which were performed by A. Knittel and H. Fangohr at the University of Southampton.[225,226]

7.1 Sample preparation

The main sample preparation process for these crystals was performed by S. Dale.[227] The cores of the crystals were grown by electrochemical deposition as discussed above and in M. Engbarth's doctoral thesis.[179,193]. The high T_c of

lead, above the boiling point of ^{4}He, made the measurements at temperatures $T \ll T_c$ more convenient. Also the core magnetisation of lead is much larger than for tin and hence the compensation of the core and shell magnetisation is more pronounced. After the core growth, the electrodes with the crystals were transferred to an electrolyte containing the ferromagnetic material. A Watt's bath, (100 mM $Ni(SO_3NH_2)_2$ + 15 mM $NiCl_2$ + 65 mM H_3BO_3), was used to plate the cores with nickel. The thickness of the nickel shell was estimated in the same way as for the S-S' core-shell structures and confirmed by FIB-milling the samples and imaging the shell directly. In Fig. 7-1 two AFM images of a Pb-Ni (a) and a Sn-Ni (b) crystal are shown which were used to determine the dimensions of the samples. Fig. 7-1c and d show two FIB milled cross-sections of a Pb-Ni triangle and a Sn-Ni rod respectively. To protect the crystal during the cutting and milling process, FIB deposition was used to cover the crystals with platinum (Pt) prior to milling. The insets in Fig. 7-1c and d present the clean interface between core and shell. There is no indication that alloying occurs at the interface. The thicknesses of the shells, estimated from the net charge flow to be $d \approx 100 - 300$ nm for both types of samples are confirmed by the images in Fig. 7-1c and d. Simulations of the stray field at the Hall probe at saturation magnetisation, M_{sat}, also yield a shell thickness of $\approx 200 - 300$ nm, which is slightly larger but still in very good agreement with the estimated values above.

7.2 Magnetisation data

For the magnetisation measurements of these samples, much higher fields were necessary than for the superconducting samples discussed earlier. Fields of $H >$ 2000 G were used to fully saturate the magnetisation of the ferromagnetic nickel shell. At these high fields the Hall probes showed weakly non-linear behaviour and the use of an empty reference Hall probe was essential to compensate for this. To account for the difference between individual Hall coefficients, a cubic function was fitted to the saturated section of the data as explained in Sec. 4.3.2. For each sample, the magnetisation was measured at several different temperatures above and below the T_c of the core. Fig. 7-2 displays the data for four different samples. For all samples, one curve of the shell magnetisation ($T = 8$ K $> T_c^{\text{core}}$) is drawn

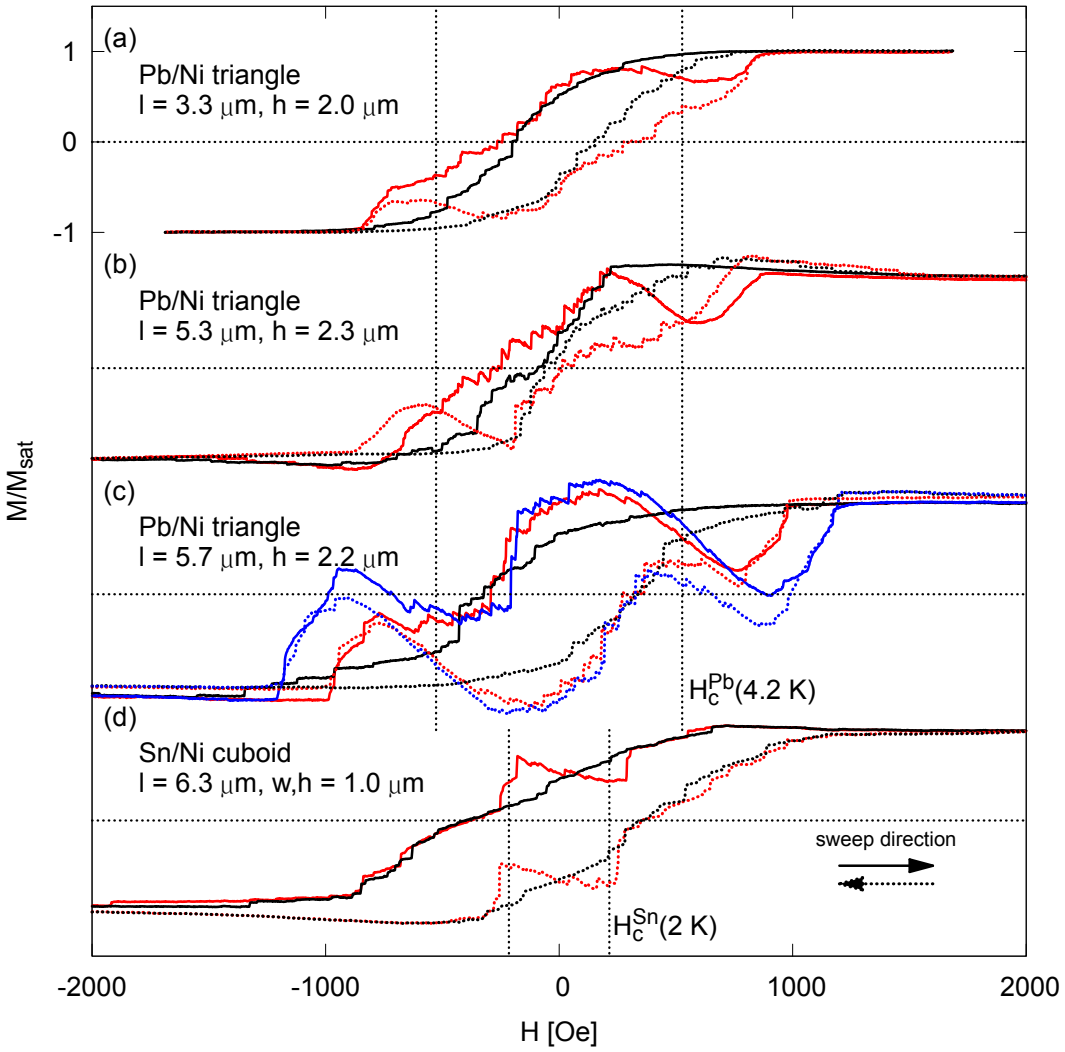

Figure 7-2: Graph showing magnetisation data normalised by the saturation magnetisation, M/M_{sat}, versus the applied field H. The black curve shows the magnetisation for $T > T_c$ ($T = 8$ K) and the red curve for $T < T_c$ ($T = 4.2$ K for (a)-(c) and $T = 2$ K for (d)). For (c) an additional curve with $T \ll T_c$ ($T = 2$ K) is shown. The solid lines show the positive sweep direction, and the dotted lines the negative sweep direction.

in black, while the red curve is for $T < T_c^{\text{core}}$. For the Pb-Ni samples in Fig. 7-2a-c this was recorded at the boiling point of helium $T = 4.2$ K, and for the Sn-Ni sample in Fig. 7-2d this was recorded at $T = 2$ K. Dotted lines indicate the value of the bulk critical field, H_c, of the core. For the large triangle in Fig. 7-2c, an additional curve is shown in blue which was recorded at $T = 2$ K $\ll T_c^{\text{Pb}}$. The magnetisation is expressed as a fraction of the saturation magnetisation M_{sat}.

In all samples, superconductivity exists at fields well in excess of the bulk critical field. A pronounced diamagnetic "dome" is visible as superconductivity nucleates in the sample at fields $|H| > \left|H_c^{\mathrm{bulk}}\right|$ and where superconductivity is destroyed at very much higher fields. This can directly be attributed to the magnetisation state of the ferromagnetic walls surrounding the core. In this regime, the magnetisation of the side walls is almost fully saturated at a value M_{FM} (*cf.* Fig. 2-25 in Sec. 2.5.3). The generated stray field, H_{FM}, opposes the externally applied field, H_{ext}, and hence the local field, represented by the vector sum of the fields, is lowered to below H_c^{core} and superconductivity survives. This compensation effect is visible in all Pb-Ni and Sn-Ni core-shell samples. The effect is strongest in the sample with the largest side length of $l = 5.7$ µm (Fig. 7-2c). For this sample, it was actually possible, at a very low temperature ($T = 2$ K $\ll T_c^{\mathrm{Pb}}$), to reverse the sign of the net magnetisation at the peak of the superconducting dome (blue curves in Fig. 7-2c) from para(ferro-)magnetic to diamagnetic and *vice versa*. Jumps in the shell magnetisation, such as domain reversal or domain wall jumps, are visible in the data for the pure core as well as in the data for the core-shell structure.

For the Sn-Ni sample in Fig. 7-2d the superconducting dome only appears in the regime where the magnetisation of the shell is reversing. H_c^{Sn} is considerably smaller than H_c^{Pb} at the temperatures used in our experiments. Hence for a fully magnetised shell, the local field never falls below the critical field of tin. Only during the magnetisation reversal process, when the magnetisation of the shell is significantly reduced, does the local effective field fall below H_c^{Sn} and superconductivity becomes restored in the core. However, by using a shell with lower saturation magnetisation, Sn-core samples should exhibit the same effects as the Pb-Ni core-shell samples shown here.

In order to highlight the changes in the magnetisation of the whole sample, Fig. 7-3 shows difference traces, $\Delta M(H)$, of the largest Pb-Ni triangle sample. For this plot, data recorded at $T = 8$ K $> T_c^{\mathrm{Pb}}$ was subtracted from the magnetisation traces recorded at various temperatures $T < T_c^{\mathrm{Pb}}$. Four distinct regimes are identified in these data. For positive field sweeps from large negative values, $|H_{ext}| > |H_{sat}|$, superconductivity first nucleates at the left hand side of the region labelled I. In this regime, the Ni shell is almost fully saturated with

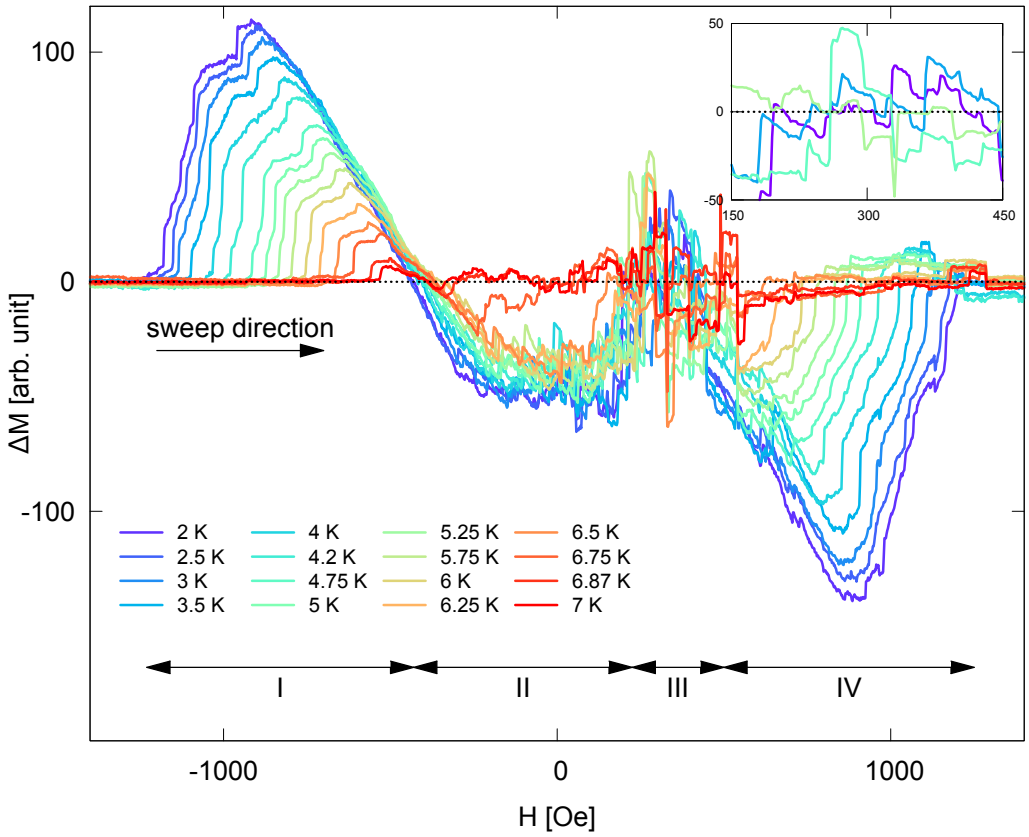

Figure 7-3: Magnetisation plots of a Pb-Ni cores-shell crystal at different temperatures $T < T_c^{\mathrm{Pb}}$. To illustrate the magnetisation contribution of the superconducting core, a measurement at $T > T_c$ was subtracted from the data. Four different characteristic regions, I - IV are observed, which are discussed in the text. The inset shows an expanded version of a subset of the curves in region III, where distinct diamagnetic "noise" is seen.

magnetisation pointing downwards, and the stray fields of the shell oppose the externally applied magnetic field. Superconductivity starts to nucleate as soon as the condition $|H_{ext} + H_{FM}| < H_c(T)$ is fulfilled anywhere in the core. The superconducting region grows with decreasing absolute value of the external field until a maximum of the superconducting dome is reached for $|H_{ext}| \approx |H_{FM}|$. Further decreasing $|H_{ext}|$ results in a decrease of the diamagnetic signal, as the external field is not able to compensate the stray field of the ferromagnetic shell anymore. When $|H_{ext} + H_{FM}| > H_c(T)$ is fulfilled everywhere in the Pb core, superconductivity collapses. The point were the superconducting fraction is largest is somewhere between region I and II. Due to the highly inhomogeneous field and

the measurement of the magnetisation with a Hall probe below the sample this point cannot be identified from the data presented here.

At the boundary between region I and region II, the magnetisation of the shell starts to reverse and the behaviour of the sample becomes much more complex as region II is entered. The reversal results in weaker stray fields, H_{FM}, in the superconducting core. The lower stray fields should facilitate the restoration of superconductivity in some areas of the sample. However, surprisingly ΔM crosses zero between region I and II which indicates a more paramagnetic net response. This can be explained by screening of the stray field by puddles of superconductivity in the core, which "throw out" more flux towards the Hall sensor. For low temperatures, the value of ΔM in this region is almost independent of temperature; only close to T_c does the value of ΔM vanish.

In the region, where the magnetisation reversal is steepest in the normal state curves (black curves in Fig. 7-2), an irregular series of steps arising from sudden changes in the wall magnetisations is seen.[115] These changes are due to the jumping domain walls and magnetic vortices between strong pinning sites as the magnetisation direction is switched. It is also possible that "Barkhausen steps" play a role in the reversal region, as these steps might be capable of changing the overall magnetic configuration of the sample enough so that a net response on the Hall probe is measured. This occurs in region III in Fig. 7-3. The inset shows an expanded version of four magnetisation traces, where these jumps are clearly displayed. Each jump in the shell magnetisation is accompanied by a correlated jump in the diamagnetic response of the superconducting core. Local changes in the magnetisation either increase or decrease the local stray fields and hence either enhance or suppress superconductivity in the core as is easily seen from the data in the inset.

Upon further increasing the field the sample enters region IV in Fig. 7-3. This region is dominated by another superconducting dome, similar to the dome in region I, but with an opposite sign. This indicates that the magnetisation of the nickel shell is now nearly fully reversed and has almost reached its saturation value parallel to the direction of the applied field. The compensation of the applied field is hence the same as for the compensation in region I. As expected,

reversing the sweep direction from $H_{ext} > H_{sat}$ results in the same evolution of diamagnetic signal with regions I-IV and the value of ΔM mirror inverted with respect to the origin.

Micromagnetic simulations, performed by A. Knittel and H. Fangohr at the University of Southampton using the finite-element solver NMAG, explain many of the effects seen in experimental data.[228,229] The simulation assumes an exchange coupling equal to $7.2 \cdot 10^{-7}$erg cm^{-1} and a saturation magnetisation of $M_{sat} = 6409$ Oe. The magnetocrystalline anisotropy, due to the polycrystalline character of the shell, is not accounted for. A tetrahedral mesh is used to model core and shell. For the shell a fine mesh is used with a tetrahedral edge length smaller than the exchange length l_{exch}. For the core, a coarse mesh is used to resolve the shell's stray field there. The screening currents and associated fields of the superconducting core are also ignored, as this would require coupled solutions of the micromagnetic equations with the G-L equations, which goes well beyond the scope of this work. A more complete discussion of the results can be found in Ref.[136] (*cf.* Appendix A).

Fig. 7-4 shows the results of these simulations. As it is not possible with state-of-the-art micromagnetic simulations to simulate a sample as large as those used in this experiment, the dimensions of the simulated sample were reduced by a factor of 10. Assuming an isotropic 250 nm thick nickel shell and ignoring any effects of the superconductor on the ferromagnetic shell, the effective field was calculated at the core. The resulting stray field seen at the Hall sensor was also calculated. In Fig. 7-4a the fraction of the superconducting core volume, where $|H_{ext} + H_{FM}| < H_c(T)$ is satisfied, is plotted. The graph shows the same "superconducting dome" as measured experimentally. For four different applied fields, the volume fraction is rendered as a 3D image in Fig. 7-4b(I-IV). In these 3D representations, the position of the Hall sensor is below the bottom of the triangular footprint. We see clearly that superconductivity first nucleates in a ring around the base edges (I), touching the top surface at three points. At the peak of the diamagnetic dome these regions are all joined up (II) and almost the whole core is superconducting. As the absolute value of the applied field is decreased the core turns normal at the perimeter, where the stray field of the shell is strongest (III). The superconducting volume continues to shrink until only a small fraction

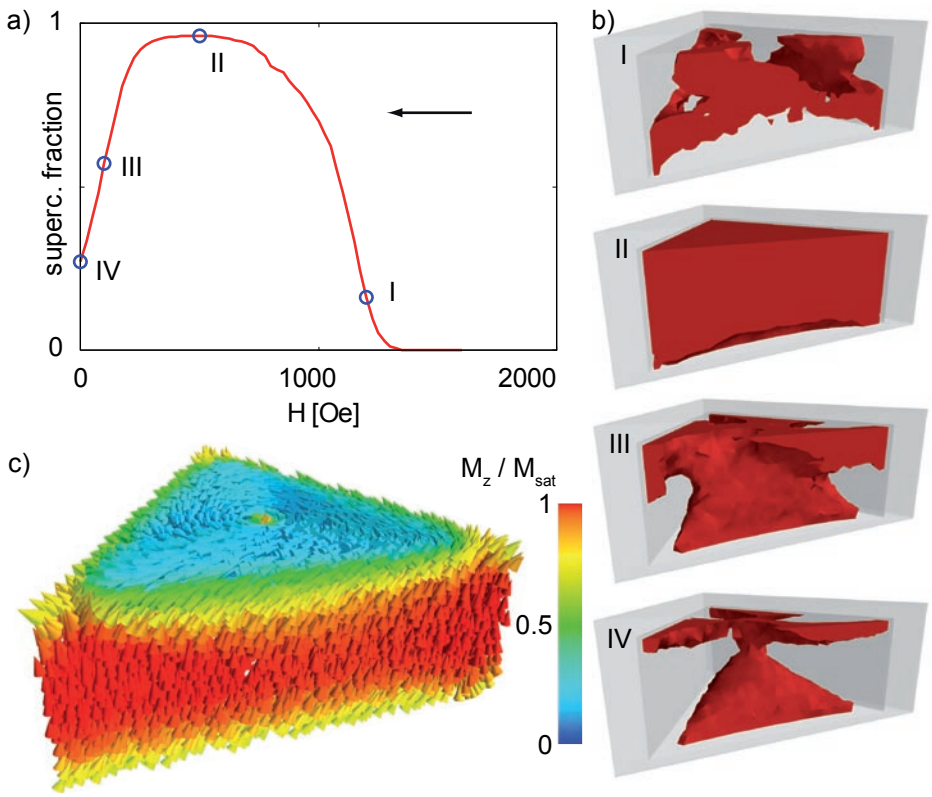

Figure 7-4: Micromagnetic simulations of the largest Pb-Ni triangle core-shell sample discussed above. The superconducting volume fraction as a function of applied field is shown in (a) and 3D renderings for four applied fields as indicated on the plot are shown in (b). A 3D vector plot of the magnetisation along the z-axis M_z/M_{sat} of the shell for a freezing field of $H_{ext} = 1000$ Oe is drawn in (c).

in the centre of the core, on the bottom and at the top is superconducting. In the last image Fig. 7-4b(IV), the formation of a large superconducting volume in the vicinity of the Hall probe is visible. This volume is likely to represent the "puddle of superconductivity" which leads to the magnetisation reversal in region II of Fig. 7-3. In the simulations, the magnetisation of the shell was "frozen" at a field of $H_{ext} = 1000$ Oe and assumed to be unchanged in a decreasing field in order to simulate the effect of magnetic pinning. Simulations at different freezing fields greater than 800 Oe revealed that the results were not very sensitive to this choice. A 3D vector plot of the shell magnetisation along the z-axis divided by the saturation magnetisation, M_z/M_{sat}, is presented in Fig. 7-4c. Note that there is a single vortex at the centre of the top surface, which is clearly correlated with the nucleation and destruction of superconductivity in Fig. 7-4b.

7.3 Conclusion

Electrochemical deposition is capable of fabricating superconducting-ferromagnetic core-shell structures with truly three dimensional geometries. Magnetisation measurements yield deep insights into the complex process of magnetisation reversal of the shell, which controls the nucleation of superconductivity in the core. In particular the possibility of controlling the magnetic response of the sample, even of switching the magnetic behaviour from para(ferro-)magnetic to diamagnetic by the application of an external magnetic field, could lead to a number of interesting applications. A relatively small change in the applied field is able to change the direction of the overall magnetisation of the sample. This could be exploited, for example, in magnetic guidance or novel memory devices. If FSHs are used as superconducting/magnetic memory devices as proposed by Nemes *et al.* one needs to be able to switch the samples between two different states.[143] By controlling the shell magnetisation with an external field, one is able to switch the core of the FSH between the normal and the superconducting state. This will define a "0" and a "1" to be read out. Moreover, electrodeposition is readily scalable and capable of producing a large number of identical samples; hence it is ideal for extension of these effects for industrial applications.

Chapter 8

Conclusions and future work

During the course of this work Hall array magnetometry measurements have been used to investigate the magnetic response of a variety of individual superconducting crystals grown by electrodeposition.

8.1 Conclusion

Electrodeposition was used to study the shape and size evolution of tin crystals from tetrafluoroboric acid solutions. In addition to complex snowflake shapes, which yield a good understanding of the crystallographic axes in tin crystals, tin crystals grow as cuboids with almost square cross-sections. The very flat, clean faces and the steep edges of the rods make them ideal samples to probe effects governed by the size and shape of the sample. In addition, tin also grows as thin triangular platelets, with steep edges. This is possible due to twinning and incomplete rod growth, although tin does not form perfect equilateral triangles which are however formed during the electrodeposition of lead. The steep edges of tin complement the slanted edges, found in lead triangles. Comparing these two, yields additional understanding of the importance of the edges for flux exit in a decreasing applied field. Electrodeposition can also be used to plate these crystals with another superconductor (lead) or with a ferromagnetic material

(nickel).

The cuboid tin crystals prepared in this way proof to be ideal model systems for studying mesoscopic, temperature dependent effects in small type I superconductors. Micromagnetic measurements on tin rods of varying sizes reveal that no intermediate state is present in our samples and that three distinct regimes are identified for the superconducting to normal phase transition for increasing temperature. At low temperature, clear supercooling and superheating is observed and generally the behaviour is close to the expected behaviour of bulk tin. As the critical temperature is approached the supercooling and superheating fields converge and the transition from the superconducting to the normal state and *vice versa* appears to become reversible, but remains clearly of first order. The crossover from a first order to a second order phase transition at temperatures very close to T_c cannot be unambiguously identified by our experiments. However, the predicted temperature dependence of H_{c3} for the second order phase transition in a thin slab ($w \ll \xi$), fits the data in the reversible regime, the observed transition is clearly of first order.

In contrast to the findings for rods, many triangular samples exhibit an intermediate state. However, the appearance of flux entry and exit in the magnetisation of individual samples varied even between similar samples. The pinning of flux on grain boundaries and twinning planes must govern the structure of the intermediate state. As these internal defects are difficult to assess, it is not possible to establish a model for the flux entry and exit or the structures formed. Nevertheless, flux exit is strongly delayed compared to the flux exit in lead triangles due to the much higher surface barrier arising from the steep edges of the tin triangles.

The S-S' tin-lead core-shell structures which were prepared and used in this work are, as far as we know, the first fully 3D S-S' core-shell structures to be investigated. The lead shell, the "strong" superconductor, in these is able to provide Cooper pairs for the "weaker" superconducting tin core, which diffuse across the interface and sustains the superconductivity in the core above both, the critical field and critical temperature of bare tin. The increase in critical temperature of the core with respect to the bulk value can be estimated to be greater than

$T_c^{\text{core}} > 1.16\ T_c^{\text{Sn}}$ for a large tin rod with a thin lead shell. For reasons we do not yet understand, the critical field of the onset of superconductivity in a configuration where the trapped flux is mostly parallel to the applied field is much higher than the field for the destruction in a field anti-parallel to the trapped flux. For smaller crystals, the shell can be regarded as a superconducting ring, in which Little-Parks like oscillations are observed as flux quanta enter and exit the sample. The periodicity can be used to estimate the width of the superconducting sheath at the perimeter of the core at $T \gg T_c^{\text{core}}$. The data suggest, that in a decreasing field, superconductivity penetrates up to ≈ 100 nm into the core while, after changing the direction of the applied field, superconductivity of the core is suppressed in an increasing field.

Enhancement of the core superconductivity is also observed in S-F core-shell structures which use a ferromagnetic nickel shell on either a superconducting lead or tin core. The main mechanism giving rise to the enhancement in these crystals is the compensation of an externally applied field by the stray field of the magnetised shell. A superconducting "dome" is observed, with a maximum at the value where the applied field is exactly compensated by the shell stray field over the largest fraction of the core volume. For one sample it was actually possible to switch the absolute measured net magnetic behaviour from diamagnetic to para(ferro)magnetic by tuning the applied field. The experimental data were compared to micromagnetic simulations, which are able to reproduce the observed behaviour.

8.2 Future work and outlook

In this final section of this thesis, some extensions of the work on hand as well as some future prospects are outlined.

There are a number of natural extensions to this work. Tin enters the mesoscopic regime very close to its critical temperature for samples with dimensions just less than one micrometre. Smaller samples should enter the mesoscopic regime at lower temperatures and hence the transition between first order and second or-

der phase transitions becomes more accessible. However, a way has to be found to manipulate these tiny crystals onto the Hall probe. The use of an optical microscope is limited by the need for space for the micromanipulator and the available lenses. Also, the signal of such small crystals, very close to the critical temperature, is extremely tiny and difficult to pick up with the currently used Hall probes. After overcoming these difficulties, measurement of other shapes are readily possible. However, it was shown that individual triangular crystals are very varied in their behaviour and it is questionable if other shapes can be produced which behave more reproducibly. In addition, simulation of more complex shapes gets increasingly difficult. Nevertheless, other shapes might yield additional understanding regarding the nucleation of superconductivity in corners of different angles or metastability for different vertical edges. All these experiments rely on the high resolution, both spatial and magnetic, of micro Hall probes. Other techniques, such as transport measurements or optical measurements would be pretty difficult to establish for the crystals produced in this work.

The S-S' core-shell system, established by electrodeposition and electroplating, is a much more fertile one for interesting new discoveries. The ability to drag superconductivity of a tin core above the boiling point of ^{4}He at ambient pressure by applying a thin lead shell is very exciting. With the crystals and techniques used for this work, only a rough estimation of the maximum enhancement of the critical temperature was possible. Here, other techniques such as Kerr microscopy or Bitter decoration could yield further insights into the extend to which the core superconductivity is influenced by another superconductor in intimate contact. Even the fabrication of core-shell structures with two different shells should be possible. By carefully choosing the electrolytes, one should be able to plate a thin normal conducting or ferromagnetic shell between the tin core and lead shell. This would yield further insight of how the proximity effect works and would complement work performed on stacked layered systems.

The behaviour of such a core-shell structure near zero applied field makes an application as superconducting memory thinkable. Utilising the fact that the core-state depends on the magnetic history, a write and read process is possible. If a small permanent magnetic field is applied, the core is either superconduct-

ing or normal, depending on the flux present at the interface. Applying a large magnetic field either parallel or antiparallel to the small "reading" field would write information onto that crystal. The fabrication by electrodeposition is easily scalable, though a way has to be found to address these bits in a real device. Additionally, the operating temperature of 4.2 K could discourage many applications. Nevertheless, it should be possible, and might be useful, for certain applications.

A memory device utilising the interaction between a soft ferromagnet and a superconductor was recently proposed.[143] The F-S core-shell structures measured during this work could yield ideal elements for such a memory device. It was shown that at the bench-scale full control of the magnetic behaviour of a single crystal is possible. By changing the applied field, the sample was switched from diamagnetic to para(ferro)magnetic over finite field ranges. Also, the positions of these switching phenomena depend on the magnetic history of the crystal. These are all the ideal pre-conditions for use in such a superconducting-magnetic memory device as proposed. The scalability of electrodeposition is just another advantage. However, the same disadvantages as above apply, namely that for the materials used in this work, the operating temperatures are too low for most serious applications.

Other applications for S-F core-shell structures might be *e.g.* for use as sensitive particle detectors. Superheated tin particles are currently used in particle detectors.[140,216] The shift to higher fields due to the compensation effects of the applied field and the magnetised shell could prove to be useful for their application in particle accelerators. The high sensitivity to changes in the net magnetic behaviour can possibly be utilised in magnetic guidance. Once tuned, by temperature or fabrication, to a certain target field, small variations around that value yield large changes in the net magnetisation.

To summarise, this work has introduced a new model system for the investigation of mesoscopic type I superconductivity in tin crystals and combined this with the established use of lead in the form of 3D core-shell structures. Micromagnetic measurements are an invaluable tool for investigating superconductivity in such crystals. The experimental findings are able to suggest a number of applications,

especially for the core-shell structures, which utilise their unique characteristics. Although these applications are currently only dreams for the future, new findings might yet demonstrate their benefits. In the last 100 years, the field of mesoscopic superconductors has received very little attention and there is plenty of room for new discoveries.

Bibliography

1. Onnes, H. K. *Communications from the Physical Laboratory of the University of Leiden* **108**, 3–24 (1908).

2. Ramsay, W. *Proceedings of the Royal Society of London* **58**, pp. 65–67 (1895).

3. Schubert, H. *Centaurus* **31**(3), 259–299 (1989).

4. June (2011). Nobelprize.org.

5. Kes, P. (2011). Talk at the NES 2011 superconductivity workshop.

6. Ouboter, R. D. *IEEE Transactions on magnetics* **23**(2), 355–370 MAR (1987).

7. Nobel, J. D. and Lindenfeld, P. *Physics Today* **49**(9), 40–42 (1996).

8. Onnes, H. K. *Communications from the Physical Laboratory of the University of Leiden* **122**, 11–15 (1911).

9. Onnes, H. K. *Communications from the Physical Laboratory of the University of Leiden* **133**, 61–68 (1913).

10. Onnes, H. K. *Communications from the Physical Laboratory of the University of Leiden* **Supplement 34 b**, 64–71 (1913).

11. Matricon, J. and Waysand, G. *The Cold Wars, A History of Superconductivity.* Rutgers University Press, New Brunswick, New Jersey, (2003).

12. Meissner, W. and Ochsenfeld, R. *Naturwissenschaften* **21**, 787 (1933).

13. Gorter, C. J. and Casimir, H. *Physica* **1**(1-6), 306 – 320 (1934).

14. London, F. and London, H. *Proceedings of the Royal Society* **A149**, 71 (1935).

15. Peierls, R. *Proceedings of the Royal Society of London. Series A, Mathematical and Physical Sciences* **155**(886), pp. 613–628 (1936).

16. Landau, L. D. *Physikalische Zeitschrift der Sowjetunion* **11**, 129 (1937).

17. Pippard, A. B. *Proceedings of the Royal Society of London. Series A. Mathematical and Physical Sciences* **216**(1127), 547–568 (1953).

18. Reynolds, C. A., Serin, B., Wright, W. H., and Nesbitt, L. B. *Physical Review* **78**(4), 487 May (1950).

19. Maxwell, E. *Physical Review* **78**(4), 477 May (1950).

20. Lock, J. M., Pippard, A. B., and Shoenberg, D. *Mathematical Proceedings of the Cambridge Philosophical Society* **47**(04), 811–819 (1951).

21. Ginzburg, V. L. and Landau, L. D. *Zh. Eksperim. i. Teor. Fiz.* **20**, 1064 (1950).

22. Abrikosov, A. A. *Journal of Experimental and Theoretical Physics* **5:6**, 1174–1182 (1957).

23. Cooper, L. N. *Physical Review* **104**, 1189–1190 Nov (1956).

24. Bardeen, J., Cooper, L. N., and Schrieffer, J. R. *Physical Review* **108**, 1175 (1957).

25. Giaever, I. *Physical Review Letters* **5**(4), 147–148 Aug (1960).

26. Josephson, B. D. *Physics Letters* **1**(7), 251 – 253 (1962).

27. Jaklevic, R. C., Lambe, J., Silver, A. H., and Mercereau, J. E. *Physical Review Letters* **12**(7), 159–160 Feb (1964).

28. Gao, L., Xue, Y. Y., Chen, F., Xiong, Q., Meng, R. L., Ramirez, D., Chu, C. W., Eggert, J. H., and Mao, H. K. *Physical Review B* **50**(6), 4260–4263 Aug (1994).

29. Kamihara, Y., Watanabe, T., Hirano, M., and Hosono, H. *Journal of the American Chemical Society* **130**, 3296 (2008).

30. Nagamatsu, J., Nakagawa, N., Muranaka, T., Zenitani, Y., and Akimitsu, J. *Nature* **410**(6824), 63–64 MAR 1 (2001).

31. Ibach, H. and Lüth, H. *Festkörperphysik*. Springer-Verlag, Berlin, Heidelberg, New York, (2002).

32. Fermi, E. *Zeitschrift für Physik A Hadrons and Nuclei* **48**, 73–79 (1928). 10.1007/BF01351576.

33. Landau, L. *Physikalische Zeitschrift der Sowjetunion* **11**, 26–35 (1937).

34. de Gennes, P. *Superconductivity of Metals and alloys*. Advanced Book Program, Perseus Books (Reading, Mass.), (1999).

35. Tinkham, M. *Introduction to Superconductivity*. Dover Publications, Mineola, New York, (2004).

36. Ginzburg, V. L. *Soviet Physics - JETP* **3**, 621 (1956).

37. Gor'kov, L. *Soviet Physics - JETP* **9**(6), 1364–1367 (1959).

38. Deaver, B. S. and Fairbank, W. M. *Physical Review Letters* **7**(2), 43–46 Jul (1961).

39. Doll, R. and Näbauer, M. *Physical Review Letters* **7**(2), 51–52 Jul (1961).

40. Little, W. A. and Parks, R. D. *Physical Review Letters* **9**(1), 9 Jul (1962).

41. Parks, R. D. and Little, W. A. *Physical Review* **133**(1A), A97 Jan (1964).

42. London, F. *Superfluids*, volume 1. John Wiley & Sons, Inc., New York, (1950).

43. Milošević, M. V. *Vortex Matter in Mesoscopic Superconductor / Ferromagnet Heterosystems*. PhD thesis, Universiteit Antwerpen Faculteit Wetenschappen Departement Fysica, (2004).

44. Fossheim, K. and Sudbø, A. *Superconductivity: physics and applications.* John Wiley & Sons Inc, (2004).

45. Brandt, E. H. *Brazilian Journal of Physics* **32**, 675 – 684 09 (2002).

46. Kleiner, W., Roth, L., and Autler, S. *Physical Review* **133**(5A), 1226–1227 (1964).

47. Saint-James, D. and Gennes, P. G. *Physics Letters* **7**(5), 306 – 308 (1963).

48. Smith, F. W., Baratoff, A., and Cardona, M. *Zeitschrift für Physik B Condensed Matter* **12**(2), 145–192 (1970).

49. Bean, C. P. and Livingston, J. D. *Physical Review Letters* **12**, 14–16 Jan (1964).

50. Jackson, J., Witte, C., and Müller, K. *Klassische Elektrodynamik.* de Gruyter, (2006).

51. De Gennes, P. *Solid State Communications* **3**, 127–130 (1965).

52. on Superconductivity, O. G. *Quantum Fluids, Proceedings of the Sussex University Symposium 16-20 August 1965.* North-Holland Publishing Company, (1966).

53. Matricon, J. and Saint-James, D. *Physics Letters A* **24**(5), 241 – 242 (1967).

54. Parr, H. *Physical Review B* **12**, 4886 (1975).

55. Parr, H. *Zeitschrift für Physik B Condensed Matter* **25**, 359–361 (1976).

56. Dolgert, A. J., Di Bartolo, S. J., and Dorsey, A. T. *Physical Review B* **53**(9), 5650–5660 Mar (1996).

57. Feder, J., Kiser, S. R., and Rothwarf, F. *Physical Review Letters* **17**(2), 87–89 Jul (1966).

58. Doll, R. and Graf, P. *Physical Review Letters* **19**(16), 897–899 Oct (1967).

59. Feder, J. and McLachlan, D. S. *Physical Review* **177**(2), 763–776 Jan (1969).

60. Hueber, D., Valette, C., and Waysand, G. *Physica B+ C* **108**, 1229–1230 (1981).

61. Chen, D.-X., Pards, E., and Sanches, A. *IEEE Trans. Magn.* **38**, 1742 (2002).

62. Chen, D.-X., Prados, C., Pardo, E., Sanchez, A., and Hernando, A. *Journal of Applied Physics* **91**(8), 5254–5259 (2002).

63. Osborn, J. *Physical Review* **67**(11-12), 351–357 (1945).

64. Cronemeyer, D. C. *Journal of Applied Physics* **70**(6), 2911–2914 (1991).

65. Torre, E. *Magnetic hysteresis*. IEEE Press, (2000).

66. Joseph, R. I. and Schlömann, E. *Journal of Applied Physics* **36**(5), 1579–1593 (1965).

67. Joseph, R. I. *Journal of applied physics* **37**(13), 4639 (1966).

68. Joseph, R. I. *Journal of applied physics* **38**(5), 2405 (1967).

69. Pardo, E., Chen, D., and Sanchez, A. *Journal of applied physics* **96**, 5365 (2004).

70. Landau, L. and Lifshitz, E. *Electrodynamics of Continuous Media*. Pergamon Press, (1960).

71. Tai, P. C. L., Beasley, M. R., and Tinkham, M. *Physical Review B* **11**, 411 (1975).

72. Desirant, M. and Shoenberg, D. *Proceedings of the Royal Society of London. Series A. Mathematical and Physical Sciences* **194**(1036), 63–79 (1948).

73. Andrew, E. R. *Proceedings of the Physical Society. Section A* **62**(2), 88 (1949).

74. Harper, F. E. and Tinkham, M. *Physical Review* **172**, 441–450 Aug (1968).

75. Egorov, V., Solt, G., Baines, C., Herlach, D., and Zimmermann, U. *Physica B: Physics of Condensed Matter* **289**, 393–395 (2000).

76. Provost, J., Paumier, E., and Fortini, A. *Journal of Physics F: Metal Physics* **4**, 439–448 (1974).

77. Fortini, A. and Paumier, E. *Physical Review B* **14**(1), 55–60 (1976).

78. Fortini, A., Hairie, A., and Girard, J. *Journal of Mathematical Physics* **20**, 2139 (1979).

79. Clem, J., Huebener, R., and Gallus, D. *Journal of Low Temperature Physics* **12**(5), 449–477 (1973).

80. Indenbom, M. and Brandt, E. *Physical Review Letters* **73**(12), 1731–1731 (1994).

81. Zeldov, E., Larkin, A. I., Geshkenbein, V. B., Konczykowski, M., Majer, D., Khaykovich, B., Vinokur, V. M., and Shtrikman, H. *Physical Review Letters* **73**, 1428–1431 Sep (1994).

82. Benkraouda, M. and Clem, J. *Physical Review B* **53**(9), 5716–5726 (1996).

83. Morozov, N., Zeldov, E., Konczykowski, M., and Doyle, R. *Physica C: Superconductivity and its applications* **291**(1-2), 113–131 (1997).

84. Douglass, D. H. *Physical Review Letters* **6**, 346–348 Apr (1961).

85. Tinkham, M. *Physical Review* **129**, 2413–2422 Mar (1963).

86. Tinkham, M. *Reviews of Modern Physics* **36**, 268–276 Jan (1964).

87. Tilley, D. R., Baldwin, J. P., and Robinson, G. *Proceedings of the Physical Society* **89**(3), 645 (1966).

88. White, R. H. *Physical Review* **142**, 241–247 Feb (1966).

89. Cody, G. D. and Miller, R. E. *Physical Review* **173**, 481–493 Sep (1968).

90. Miller, R. E. and Cody, G. D. *Physical Review* **173**, 494–503 Sep (1968).

91. Saint-James, D. *Physics Letters* **16**(3), 218 – 220 (1965).

92. Fink, H. J. *Physical Review* **177**, 732–737 Jan (1969).

93. Schultens, H. *Zeitschrift für Physik A Hadrons and Nuclei* **232**(5), 430–438 (1970).

94. van Gelder, A. P. *Physical Review Letters* **20**, 1435–1436 Jun (1968).

95. Fomin, V. M., Devreese, J. T., and Moshchalkov, V. V. *EPL (Europhysics Letters)* **42**(5), 553 (1998).

96. Schweigert, V. A. and Peeters, F. M. *Physical Review B* **60**(5), 3084–3087 Aug (1999).

97. Landau, I. L. and Rinderer, L. *Journal of Low Temperature Physics* **100**(3), 219–228 (1995).

98. Moshchalkov, V. V., Gielen, L., Strunk, C., Jonckheere, R., Qiu, X., Haesendonck, C. V., and Bruynseraede, Y. *Nature* **373**, 319–322 (1995).

99. Morelle, M., Teniers, G., Chibotaru, L., Ceulemans, A., and Moshchalkov, V. *Physica C: Superconductivity* **369**(1-4), 351–355 (2002).

100. Morelle, M., Bekaert, J., and Moshchalkov, V. *Physical Review B* **70**(9), 094503 (2004).

101. Indekeu, J. and van Leeuwen, J. *Physica C: Superconductivity* **251**(3-4), 290 – 306 (1995).

102. Indekeu, J. and Van Leeuwen, J. *Physica A: Statistical Mechanics and its Applications* **236**(1-2), 114–122 (1997).

103. Fink, H. J. and Joiner, W. C. H. *Physical Review Letters* **23**(3), 120–123 Jul (1969).

104. Khlyustikov, I. and Buzdin, A. *Advances in Physics* **36**(3), 271–330 (1987).

105. Khlyustikov, I. *Journal of Experimental and Theoretical Physics* **85**(3), 609–615 (1997).

106. Montevecchi, E. and Indekeu, J. *Physical Review B* **62**(21), 14359 (2000).

107. Yampolskii, S. and Peeters, F. *Physical Review B* **62**(14), 9663 (2000).

108. Baelus, B. J., Yampolskii, S. V., Peeters, F. M., Montevecchi, E., and Indekeu, J. O. *Physical Review B* **65**(2), 024510 Dec (2001).

109. Marchenko, V. and Podolyak, E. *Journal of Experimental and Theoretical Physics* **100**(2), 311–313 (2005).

110. Zha, G., Zhou, S., and Zhu, B. *Physical review B* **73**(9) MAR (2006).

111. Zha, G., Zhou, S., Zhu, B., Shi, Y., and Zhao, H. *Physical Review B* **74**(2), 024527 (2006).

112. Barba-Ortega, J., Sardella, E., and Aguiar, J. A. *Superconductor Science and Technology* **24**(1), 015001 (2011).

113. Heisenberg, W. *Zeitschrift für Physik A Hadrons and Nuclei* **49**, 619–636 (1928). 10.1007/BF01328601.

114. Pauli, W. *Zeitschrift für Physik A Hadrons and Nuclei* **31**(1), 765–783 (1925).

115. Barkhausen, H. *Zeitschrift für Physik* **20**, 401 (1919).

116. Kittel, C. *Reviews of Modern Physics* **21**, 541–583 Oct (1949).

117. Braun, A., Feldmann, B., and Wuttig, M. *Journal of Magnetism and Magnetic Materials* **171**(1-2), 16 – 28 (1997).

118. Yang, Z., Lange, M., Volodin, A., Szymczak, R., and Moshchalkov, V. V. *Nature Materials* **3**(11), 793–798 (2004).

119. Rusanov, A. Y., Hesselberth, M., Aarts, J., and Buzdin, A. I. *Physical Review Letters* **93**(5), 057002 Jul (2004).

120. Buzdin, A. I. *Reviews of Modern Physics* **77**(3), 935–976 Sep (2005).

121. Lyuksyutov, I. F. and Pokrovsky, V. L. *Advances in Physics* **54**(1), 67–136 (2005).

122. Aladyshkin, A. Y., Silhanek, A. V., Gillijns, W., and Moshchalkov, V. V. *Superconductor Science and Technology* **22**(5), 053001 (2009).

123. Doria, M. M., de C. Romaguera, A. R., Milošević, M. V., and Peeters, F. M. *EPL (Europhysics Letters)* **79**(4), 47006 (2007).

124. Doria, M. M., de C. Romaguera, A. R., and Peeters, F. M. *Physical Review B* **81**(10), 104529 Mar (2010).

125. Lin, L. K., Chi, Y. S., Chen, T. M., Shyu, S. G., Huang, J. H., and Lee, S. F. *Journal of Applied Physics* **105**(7), 07D519 (2009).

126. Vodolazov, D. Y., Gribkov, B. A., Gusev, S. A., Klimov, A. Y., Nozdrin, Y. N., Rogov, V. V., and Vdovichev, S. N. *Physical Review B* **72**(6), 064509 Aug (2005).

127. Garif'yanov, N., Goryunov, Y., Mühge, T., Lazar, L., Khaliullin, G., Westerholt, K., Garifullin, I., and Zabel, H. *The European Physical Journal B - Condensed Matter and Complex Systems* **1**, 405–407 (1998). 10.1007/s100510050203.

128. Bulaevskii, L. N. and Chudnovsky, E. M. *Physical Review B* **63**(1), 012502 Dec (2000).

129. Dubonos, S. V., Geim, A. K., Novoselov, K. S., and Grigorieva, I. V. *Physical Review B* **65**(22), 220513 Jun (2002).

130. Gillijns, W., Aladyshkin, A. Y., Silhanek, A. V., and Moshchalkov, V. V. *Physical Review B* **76**(6), 060503 Aug (2007).

131. Tamegai, T., Nakao, Y., Tsuchiya, Y., and Nakajima, Y. *Physica C: Superconductivity* **468**(15-20), 1308 – 1312 (2008). Proceedings of the 20th International Symposium on Superconductivity (ISS 2007), Proceedings of the 20th International Symposium on Superconductivity (ISS 2007).

132. Lange, M., Bael, M. J. V., Bruynseraede, Y., and Moshchalkov, V. V. *Physical Review Letters* **90**(19), 197006 May (2003).

133. Milošević, M. V., Berdiyorov, G. R., and Peeters, F. M. *Physical Review Letters* **95**(14), 147004 Sep (2005).

134. Golubović, D. S., Pogosov, W. V., Morelle, M., and Moshchalkov, V. V. *EPL (Europhysics Letters)* **65**(4), 546 (2004).

135. Lange, M., Van Bael, M. J., Silhanek, A. V., and Moshchalkov, V. V. *Physical Review B* **72**(5), 052507 Aug (2005).

136. Müller, A., Dale, S. E. C., Engbarth, M. A., Bending, S. J., Peter, L. M., Knittel, A., and Fangohr, H. *Advanced Functional Materials* **21**(10), 1874–1880 (2011).

137. Clogston, A. M. *Physical Review Letters* **9**, 266–267 Sep (1962).

138. Chandrasekhar, B. S. *Applied Physics Letters* **1**(1), 7–8 (1962).

139. Jaccarino, V. and Peter, M. *Physical Review Letters* **9**(7), 290–292 Oct (1962).

140. Larrea, A., Morales, A., Waysand, G., and Bartolomé, J. *Nuclear Instruments and Methods in Physics Research Section A: Accelerators, Spectrometers, Detectors and Associated Equipment* **317**(3), 541 – 544 (1992).

141. Tagirov, L. R. *Physical Review Letters* **83**(10), 2058–2061 Sep (1999).

142. Gu, J. Y., You, C.-Y., Jiang, J. S., Pearson, J., Bazaliy, Y. B., and Bader, S. D. *Physical Review Letters* **89**(26), 267001 Dec (2002).

143. Nemes, N. M., Visani, C., Leon, C., Garcia-Hernandez, M., Simon, F., Fehér, T., te Velthuis, S. G. E., Hoffmann, A., and Santamaria, J. *Applied Physics Letters* **97**(3), 032501 (2010).

144. Xia, Y., Rogers, J. A., Paul, K. E., and Whitesides, G. M. *Chemical Reviews* **99**(7), 1823–1848 (1999).

145. Shchukin, V. A. and Bimberg, D. *Reviews of Modern Physics* **71**, 1125–1171 Jul (1999).

146. Datta, M. and Landolt, D. *Electrochimica Acta* **45**, 2535 (2000).

147. Chernov, A. A. *Journal of Materials Science: Materials in Electronics* **12**, 437–449 (2001). 10.1023/A:1011839431276.

148. Barth, J. V., Costantini, G., and Kern, K. *Nature* **437**, 671–679 (2005).

149. Gates, B. D., Xu, Q., Stewart, M., Ryan, D., Willson, C. G., and Whitesides, G. M. *Chemical Reviews* **105**(4), 1171–1196 (2005). PMID: 15826012.

150. Martín, J., Jaccard, Y., Hoffmann, A., Nogués, J., George, J., Vicent, J., and Schuller, I. *Journal of applied physics* **84**, 411 (1998).

151. Kim, N., Hansen, K., Toppari, J., Suppula, T., and Pekola, J. *Journal of Vacuum Science & Technology B: Microelectronics and Nanometer Structures* **20**, 386 (2002).

152. Hao, L., Macfarlane, J., Gallop, J., Cox, D., Joseph-Franks, P., Hutson, D., Chen, J., and Lam, S. *Instrumentation and Measurement, IEEE Transactions on* **56**(2), 392–396 (2007).

153. Pangarov, N. A. *Electrochimica Acta* **9**, 721 (1964).

154. Grujicic, D. and Pesic, B. *Electrochimica acta* **49**(26), 4719–4732 (2004).

155. Nasirpouri, F., Bending, S., Peter, L., and Fangohr, H. *Thin Solid Films* **In Press, Corrected Proof**, – (2011).

156. Nasirpouri, F., Engbarth, M. A., Bending, S. J., Peter, L. M., Knittel, A., Fangohr, H., and Milošević, M. V. *Applied Physics Letters* **98**(22), 222506 (2011).

157. Huczko, A. *Applied Physics A: Materials Science & Processing* **70**(4), 365–376 (2000).

158. Lai, M., Martinez, J., Grätzel, M., and Riley, D. *Journal of Materials Chemistry* **16**(27), 2843–2845 (2006).

159. Djenizian, T., Hanzu, I., Premchand, Y. D., Vacandio, F., and Knauth, P. *Nanotechnology* **19**(20), 205601 (2008).

160. Kaltenpoth, G., Himmelhaus, M., Slansky, L., Caruso, F., and Grunze, M. *Advanced Materials* **15**(13), 1113–1118 (2003).

161. Chen, Z., Zhan, P., Wang, Z., Zhang, J., Zhang, W., Ming, N., Chan, C., and Sheng, P. *Advanced Materials* **16**(5), 417–422 (2004).

162. Liu, M., Li, X., Imrane, H., Chen, Y., Goodrich, T., Cai, Z., Ziemer, K., Huang, J., and Sun, N. *Applied physics letters* **90**, 152501 (2007).

163. Bresadola, M. *Brain Research Bulletin* **46**(5), 367 – 380 (1998).

164. Hunt, L. *Gold Bulletin* **6**(1), 16–27 (1973).

165. Fisher, A. C. *Electrode Dynamics*. Oxford Chemistry Primers, Oxford, (1996).

166. Gibbs, J. *The Collected works Volume I*. Yale university press, (1948).

167. Volmer, M. and Weber, A. *Zeitschrift für Physikalische Chemie* **119**, 277–301 (1926).

168. Frakas, L. *Zeitschrift für Physikalische Chemie* **125**, 236 (1927).

169. Becker, R. and Döring, W. *Annalen der Physik* **416**(8), 719–752 (1935).

170. Markov, I. *Crystal growth for beginners*. World Scientific Singapore, (1995).

171. Mullin, J. W. *Crystallization and Precipitation*. Wiley-VCH Verlag GmbH & Co. KGaA (2000).

172. Mullin, J. *Crystallization*. Butterworth-Heinemann, (2001).

173. Sieradzki, K., Brankovic, S. R., and Dimitrov, N. *Science* **284**(5411), 138–141 (1999).

174. Budevski, E., Staikov, G., and Lorenz, W. J. *Electrochimica Acta* **45**, 2559 (2000).

175. Cline, K. K., McDermott, M. T., and McCreery, R. L. *The Journal of Physical Chemistry* **98**(20), 5314–5319 (1994).

176. Hamann, C. H. and Vielstich, W. *Elektrochemie*. Wiley-VCH, Weinheim, (2004).

177. Scharifker, B. and Hills, G. *Electrochimica Acta* **28**, 879 (1983).

178. Hyde, M. E. and Compton, R. G. *Journal of Electroanalytical Chemistry* **549**, 1 – 12 (2003).

179. Müller, A., Dale, S. E. C., Engbarth, M. A., Bending, S. J., and Peter, L. M. *CrystEngComm* **12**(7), 2135–2138 (2010).

180. Santos, M. C. and Bulhões, L. O. S. *Electrochimica Acta* **48**, 2607 (2003).

181. Wranglén, G. *Electrichimica Acta* **2**, 130 (1960).

182. Fukami, K., Nakanishi, S., Yamasaki, H., Tada, T., Sonoda, K., Kamikawa, N., Tsuji, N., Sakaguchi, H., and Nakato, Y. *Journal of Physical Chemistry C* **111**, 1150 (2007).

183. Chou, N. H. and Schaak, R. E. *Chemistry of Materials* **20**, 2081 (2008).

184. Lizzul Rinne, C., Hren, J. J., and Fedkiw, P. S. *Journal of The Electrochemical Society* **149**, C150 (2002).

185. Tian, M., Wang, J., Snyder, J., Kurtz, J., Liu, Y., Schiffer, P., Mallouk, T. E., and Chan, M. H. W. *Applied Physics Letters* **83**, 1620 (2003).

186. Torrent-Burgués, J., Guaus, E., and Sanz, F. *Journal of Applied Electrochemistry* **32**, 225 (2002).

187. Gómez, E., Guaus, E., Sanz, F., and Vallés, E. *Journal of Electroanalytical Chemistry* **465**, 63 (1999).

188. Leubner, I. H. *The Journal of Physical Chemistry* **91**(23), 6069–6073 (1987).

189. Oskam, G., Vereecken, P. M., and Searson, P. C. *Journal of The Electrochemical Society* **146**(4), 1436–1441 (1999).

190. Davies, A., Gielen, M., and Pannell, K. *Tin chemistry: fundamentals, frontiers, and applications*. John Wiley & Sons Inc, (2008).

191. Hall, E. H. *American Journal of Mathematics* **2**(3), pp. 287–292 (1879).

192. Bending, S. *Advances in physics* **48**(4), 449–535 JUL-AUG (1999).

193. Engbarth, M. A. *Hall Magnetometry of Electrodeposited Superconducting Pb Mesostructures*. PhD thesis, University of Bath, Department of Physics, April (2010).

194. Geim, A. *JETP LETTERS* **50**(8), 389–393 OCT 25 (1989).

195. Bending, S. J., von Klitzing, K., and Ploog, K. *Physical Review B* **42**(16, Part A), 9859–9864 DEC 1 (1990).

196. Dingle, R., Störmer, H. L., Gossard, A. C., and Wiegmann, W. *Applied Physics Letters* **33**(7), 665–667 (1978).

197. Johnson, J. B. *Physical Review* **32**(1), 97 Jul (1928).

198. Nyquist, H. *Physical Review* **32**(1), 110–113 Jul (1928).

199. Oral, A., Bending, S. J., and Henini, M. volume 14, 1202–1205. AVS, (1996).

200. Geim, A. K., Dubonos, S. V., Lok, J. G. S., Grigorieva, I. V., Maan, J. C., Hansen, L. T., and Lindelof, P. E. *Applied Physics Letters* **71**(16), 2379–2381 (1997).

201. Bending, S. J. and Oral, A. *Journal of Applied Physics* **81**(8), 3721–3725 (1997).

202. Li, X.-Q. and Peeters, F. M. *Superlattices and Microstructures* **22**(2), 243 – 248 (1997).

203. Beenakker, C. W. J. and Houten, H. v. *Physical Review B* **39**(14), 10445–10448 May (1989).

204. Ford, C. J. B., Washburn, S., Büttiker, M., Knoedler, C. M., and Hong, J. M. *Physical Review Letters* **62**(23), 2724–2727 Jun (1989).

205. Beenakker, C. W. J. and van Houten, H. *Physical Review Letters* **63**(17), 1857–1860 Oct (1989).

206. Geim, A. K., Grigorieva, I. V., Lok, J. G. S., Maan, J. C., Dubonos, S. V., Li, X. Q., Peeters, F. M., and Nazarov, Y. V. *Superlattices and Microstructures* **23**(1), 151 – 160 (1998).

207. Rahm, M., Biberger, J., and Weiss, D. In *Nano-physics & Bio-electronics: A New Odyssey,* Chakraborty, T., Peeters, F., and Sivan, U., editors, 257–280 (ELSEVIER SCIENCE BV, Sara Burgerhartstraat 25, Po Box 211, 1000

Ae Amsterdam, Netherlands, 2002). International Meeting on Nano-Physics and Bio-Electronics, DRESDEN, GERMANY, AUG 06-30, 2001.

208. Roukes, M. L., Scherer, A., Allen, S. J., Craighead, H. G., Ruthen, R. M., Beebe, E. D., and Harbison, J. P. *Physical Review Letters* **59**(26), 3011–3014 Dec (1987).

209. Baranger, H. U. and Stone, A. D. *Physical Review Letters* **63**(4), 414–417 Jul (1989).

210. Kastalsky, A. and Hwang, J. C. M. *Solid State Communications* **51**(5), 317 – 322 (1984).

211. Shaw, R. W., Mapother, D. E., and Hopkins, D. C. *Physical Review* **120**, 88 (1960).

212. Casalbuoni, S., Czapek, G., Hasenbalg, F., Hauser, M., Janos, S., Pretzl, K., Calatroni, S., Sgobba, S., and Vollenberg, W. *Nuclear Instruments and Methods in Physics Research Section A: Accelerators, Spectrometers, Detectors and Associated Equipment* **459**(3), 469 – 474 (2001).

213. Zemmour, K. and Saidi, K. *Thin Solid Films* **424**, 253 (2003).

214. Stewart, G. R., Fisk, Z., Willis, J. O., and Smith, J. L. *Physical Review Letters* **52**, 679 (1984).

215. Mohanty, S. and Dheer, P. N. *Solid State Communications* **50**(8), 745 – 747 (1984).

216. Larrea, A., Bartolomé, J., Morales, A., Morales, J., and Waysand, G. *Journal of Magnetism and Magnetic Materials* **104-107**(Part 1), 229 – 230 (1992).

217. Girard, T. and Figueiredo, S. *PHYSICAL REVIEW-SERIES B-* **76**(10), 104513 (2007).

218. Müller, A., Milošević, M. V., Dale, S. E. C., Engbarth, M. A., and Bending, S. J. . In Preparation.

219. Chen, C.-X. *Journal of Materials Science Letters* **6**, 232–234 (1987). 10.1007/BF01728996.

220. Miller, P. B. *Physical Review* **113**, 1209–1212 Mar (1959).

221. Lambert, C. and Raimondi, R. *Journal of Physics: Condensed Matter* **10**, 901 (1998).

222. Kaneko, S., Hiller, U., Slaughter, J., Falco, C., Coccorese, C., and Maritato, L. *PHYSICAL REVIEW B* **58**(13), 8229–8231 OCT 1 (1998).

223. Brammertz, G., Golubov, A. A., Verhoeve, P., den Hartog, R., Peacock, A., and Rogalla, H. *Applied Physics Letters* **80**(16), 2955–2957 (2002).

224. Pearl, J. *Applied Physics Letters* **5**, 65–66 (1964).

225. Knittel, A., Franchin, M., Bordignon, G., Fischbacher, T., Bending, S., and Fangohr, H. *Journal of Applied Physics* **105**(7), 07D542 (2009).

226. Knittel, A., Franchin, M., Fischbacher, T., Nasirpouri, F., Bending, S., and Fangohr, H. *New Journal of Physics* **12**, 113048 (2010).

227. Dale, S. E. C., Müller, A., Engbarth, M. A., Bending, S. J., and Peter, L. M. in preparation.

228. Fischbacher, T., Franchin, M., Bordignon, G., and Fangohr, H. *IEEE Transactions on Magnetics* **43**(6), 2896–2898 (2007).

229. O'Handley, R. C. *Modern Magnetic Materials: Principles and Applications*. John Wiley & Sons, (2000).

Appendix A

Published papers